

**Department of Physics and Astronomy  
University of Heidelberg**

Bachelor Thesis in Physics  
submitted by

**Alica Marie Enderich**

born in Wiesbaden (Germany)

**February 2024**



**Performance study on photon measurements  
using the Photon Conversion Method  
with ALICE in Run 3**

This Bachelor Thesis has been carried out by Alica Marie Enderich at the  
Physikalisches Institut of the University of Heidelberg  
under the supervision of  
Prof. Dr. Silvia Masciocchi



## Abstract

This thesis will present analysis results on the PCM performance with ALICE in Run 3 for pp collisions at  $\sqrt{s_{NN}} = 13.6$  TeV. In the first part, the thesis will focus on studies of the material budget in the radial interval  $0 \text{ cm} \leq R_{xy} \leq 90 \text{ cm}$ .

With the beginning of Run 3 of the LHC at CERN and the related upgrades of the detectors used in the ALICE experiment, also the material budget associated with the experimental setup changed. Therefore, an update of the knowledge of the material budget is necessary as this is required for the reconstruction of charged particles produced in collisions.

The material budget can be studied using photons that can convert into  $e^+e^-$  pairs when traversing material. The photon conversions can then be reconstructed and subsequently be used to map the detector material. This allows the improvement of Monte Carlo simulations used for charged particle reconstruction. Reconstructing photons in this way is called photon conversion method (PCM). In this thesis, also a first calculation of calibration weights will be presented. The calibration weights will be estimated using two different methods: On the one hand using pion-isospin symmetry, and on the other hand calibration wires installed as a reference inside the Inner Tracking System of ALICE.

The main source of photons are neutral pions  $\pi^0$  and  $\eta$  mesons. Neutral pions can be reconstructed in the two photon decay channel. Therefore, the experimental  $\pi^0$  mass resolution can be used to examine the momentum resolution and thus the quality of the reconstructed photons. In the second part of the thesis, the quality of the reconstructed photons is being studied using the  $\pi^0$  invariant mass.



## Zusammenfassung

In dieser Arbeit werden Analyseergebnisse zur Leistung der Photon-Conversion-Methode (PCM) mit ALICE in Run 3 für pp-Kollisionen bei  $\sqrt{s_{NN}} = 13,6$  TeV präsentiert. Im ersten Teil wird die Arbeit sich auf Studien des Materialbudgets im radialen Intervall  $0 \text{ cm} \leq R_{xy} \leq 90 \text{ cm}$  konzentrieren.

Mit dem Beginn des Run 3 des LHC am CERN und dem damit verbundenen Upgrades der einzelnen im ALICE-Experiment verwendeten Detektoren hat sich auch das Materialbudget des experimentellen Aufbaus verändert. Für die Rekonstruktion geladener Teilchen, die bei ben Kollisionen entstehen, ist es daher wichtig, das Wissen über das Materialbudget zu aktualisieren.

Das Materialbudget kann mithilfe von Photonen untersucht werden, die in  $e^+e^-$ -Paare konvertieren können, wenn sie Material durchqueren. Die Photonkonversionen können dann rekonstruiert und anschließend zur Untersuchung des Detektormaterials verwendet werden. Dies ermöglicht die Verbesserung von Monte-Carlo-Simulationen, die für die Rekonstruktion geladener Teilchen benötigt werden. Das Rekonstruieren von Photonen auf diese Art wird als Photonkonversionsmethode (PCM) bezeichnet. In dieser Arbeit wird außerdem eine erste Berechnung von Kalibrierungsgewichten vorgestellt. Die Kalibrierungsgewichte werden dabei mithilfe von zwei Methoden geschätzt: Einerseits unter Verwendung der Isospinsymmetrie von Pionen und andererseits mithilfe Kalibrierungsdrähten, die als Referenz im Inneren Tracking System von ALICE installiert wurden.

Die größten Quellen für Photonen sind neutrale Pionen  $\pi^0$  und  $\eta$  Mesonen. Neutrale Pionen können im zwei Photonen Zerfallskanal rekonstruiert werden. Daher kann die experimentelle  $\pi^0$ -Massenaufösung verwendet werden, um die Impulsaufösung und somit die Qualität der rekonstruierten Photonen zu untersuchen. Im zweiten Teil der Arbeit wird die Qualität der rekonstruierten Photonen mithilfe der invarianten Masse von  $\pi^0$  untersucht.



# Contents

<b>1</b>	<b>Introduction</b>	<b>1</b>
1.1	Motivation . . . . .	1
1.2	Standard Model . . . . .	2
1.3	Quantum Chromodynamics (QCD) . . . . .	3
1.4	Quark-gluon plasma (QGP) . . . . .	5
<b>2</b>	<b>The ALICE experiment</b>	<b>7</b>
2.1	Large Hadron Collider (LHC) . . . . .	7
2.2	A Large Ion Collider Experiment (ALICE) . . . . .	7
2.2.1	Inner Tracking System (ITS) . . . . .	9
2.2.2	Time Projection Chamber (TPC) . . . . .	11
2.2.3	Transition Radiation Detector (TRD) . . . . .	12
2.2.4	Time-of-Flight detector (TOF) . . . . .	13
<b>3</b>	<b>Interaction processes of photons and electrons</b>	<b>16</b>
3.1	Interactions of photons with matter . . . . .	16
3.1.1	Photoelectric effect . . . . .	16
3.1.2	Compton scattering . . . . .	17
3.1.3	Pair production . . . . .	18
3.2	Interactions of electrons (positrons) with matter . . . . .	19
3.2.1	Ionisation . . . . .	19
3.2.2	Bremsstrahlung . . . . .	20
3.2.3	Transition and Cherenkov radiation . . . . .	20
<b>4</b>	<b>Photon Conversion Method (PCM)</b>	<b>22</b>
4.1	V0 Reconstruction and Photon Identification . . . . .	22
4.2	Data sets and Monte Carlo simulations . . . . .	26
4.3	Analysis procedure . . . . .	28
4.3.1	Analysis of the material budget . . . . .	28
4.3.2	Analysis of the photon momentum resolution . . . . .	30
<b>5</b>	<b>Material budget in the ITS2 and the TPC</b>	<b>33</b>
5.1	Detailed comparison of data and anchored Monte Carlo . . . . .	35
5.2	Comparison in $\varphi$ and $\eta$ in the radial interval of $42 \text{ cm} \leq R_{xy} \leq 58 \text{ cm}$ . . . . .	40
5.3	Reconstruction efficiency . . . . .	44
5.4	Purity of the photon sample . . . . .	45
5.5	Transverse momentum spectra . . . . .	46

5.6	Calibration of the material budget . . . . .	47
5.6.1	Pion-isospin-symmetry based calibration weights $\Omega_i$ . . . . .	47
5.6.2	Tungsten-wire based calibration weights $\omega_i$ . . . . .	49
5.6.3	Comparison of the calibration weights $\Omega_i$ and $\omega_i$ . . . . .	50
5.7	Conclusions on the material budget . . . . .	50
<b>6</b>	<b>Photon momentum resolution using neutral pions</b>	<b>52</b>
6.1	Neutral pion reconstruction . . . . .	53
6.1.1	Fit on $\pi^0$ invariant mass . . . . .	53
6.1.2	Yield extraction . . . . .	56
6.2	Comparison of $\pi^0$ invariant mass fit and raw yield . . . . .	57
6.2.1	Comparison of data LHC22f and anchored Monte Carlo LHC23d1k	57
6.2.2	Comparison of the data sets LHC22f, LHC23zc and LHC22o min. Bias . . . . .	60
<b>7</b>	<b>Summary and Outlook</b>	<b>62</b>
<b>A</b>	<b>Appendix</b>	<b>65</b>
A.1	Studies on material budget . . . . .	65
A.1.1	Analysis Tasks . . . . .	65
A.1.2	Integrated plots . . . . .	65
A.1.3	Two-dimensional plots . . . . .	67
A.1.4	Detailed analysis for different radii . . . . .	71
A.2	Neutral pion reconstruction . . . . .	76
A.2.1	Analysis Tasks . . . . .	76
A.2.2	Results for LHC22f . . . . .	78
A.2.3	Results for LHC23d1k (MC) . . . . .	83
A.2.4	Results for LHC23zc . . . . .	86
A.2.5	Results for LHC22o (min. Bias) . . . . .	91
<b>B</b>	<b>List of Acronyms</b>	<b>96</b>
<b>C</b>	<b>Bibliography</b>	<b>98</b>



# 1 Introduction

## 1.1 Motivation

High-energy physics aims to achieve a more profound comprehension of the composition of matter and the forces that regulate their interactions. This can be done by studying Quantum Chromodynamics (QCD) and exploring a state of matter called quark-gluon plasma (QGP). One experiment dedicated to this research is ALICE (A Large Ion Collider Experiment), which is part of the four major experiments at the CERN Large Hadron Collider (LHC).

During the Long Shutdown 2, the ALICE experiment at CERN-LHC underwent major upgrades. One of the major changes was the installation of the new Inner Tracking System (ITS2) by which a new beam-pipe was installed in order to place the silicon pixel detectors closer to the interaction point. For an overview of the upgrades of the different parts of the detector, see chapter 2. All those changes lead to the necessity to renew the implementation of the detector material in the Monte Carlo simulation and therefore a new cross-check of the knowledge of the material budget was necessary. This is needed for the reconstruction of charged particles that are produced in the collisions.

After an introduction to the ALICE experiment and the theory behind it in chapter 2 respectively this chapter, the interaction processes of photons and electrons will be explained in chapter 3. In a next step, the photon conversion method as well as the data used in the analysis are introduced in chapter 4.

The purpose of this thesis is to study the performance of the photon conversion method (PCM) in Run 3. In a nutshell, PCM uses the conversion of photons in electron positron pairs to measure photons that convert while traversing matter. Therefore, in the first step of the analysis, the material budget is investigated (see chapter 5). This allows to draw conclusions about the implementation of the detector material into the Monte Carlo simulation. Consequently, this allows to compare the photon momentum resolution for data and Monte Carlo.

In a next step of the analysis, a first estimate of calibration weights for the material budget is done. Calibration weights introduce the possibility to correct the material budget description in simulations. Even though the complete calibration of the material budget requires additional steps that were not done in this thesis, this already leads to first insights. The calibration weights are going to be estimated using two different methods that were introduced in Run 2. One method will use the approximate pion-isospin symmetry and the other method will be using two tungsten calibration wires that were inserted in the ITS2 of the ALICE detector. During Run 2, the latter

method was performed using the gas of the Time Projection Chamber of ALICE. For the purpose of calibration in Run 3, wires were installed that can now be used to extend the gas based calibration. For further information on the calibration weights in Run 2, see [1].

In the last step, the photon momentum resolution and momentum scale is studied (see chapter 6) by measuring the width of the peak at the  $\pi^0$  rest mass in the two photon invariant mass.

## 1.2 Standard Model

Until today, the Standard Model (SM) [2] is the most successful theory in Particle Physics. It was developed in the 1970s and describes our understanding of the fundamental structure of matter. The SM consists of several elementary particles and three of the four fundamental forces, namely the electromagnetic, the weak and the strong force. It leaves out the gravitational force which indicates that the SM is not yet a complete theory.

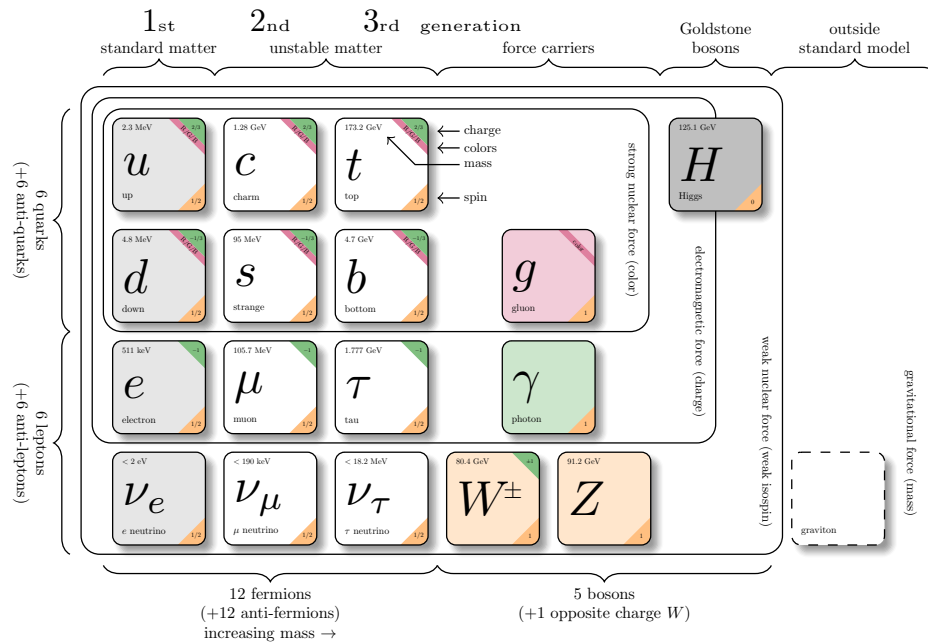


Figure 1.1: The elementary particles, bosons and interactions of the Standard Model of particle physics [2]

The Standard Model divides the elementary particles into fermions and bosons (see figure 1.1). They are classified by their spin: Elementary fermions have a half-integer

spin and obey the Fermi-Dirac statistics, whereas elementary bosons have an integer spin and obey the Bose-Einstein statistics.

The bosons can be further divided into scalar ( $H$ ) and gauge ( $\gamma$ ,  $W^\pm$  and  $Z$ ) bosons. The gauge bosons having spin 1 act as mediators of the interactions between fermions. The SM consists out of twelve gauge bosons in total, namely photons carrying the electromagnetic interaction,  $W^\pm$  and  $Z$  bosons for the weak interaction and eight gluons mediating the strong interaction. The Higgs boson  $H$  is a spin 0 scalar boson and it explains why the elementary particles apart from the photon and the gluons are massive.

In addition, there are twelve fermions, each of them having spin 1/2 and a corresponding anti-particle with the same mass and spin but opposite charge. The fermions can be divided into quarks and leptons and are further ranked in three generations going from the most stable ones on the left to the most unstable ones on the right in figure 1.1. In total, there are six types of quarks that are also known as flavours: up (u), down (d), strange (s), charm (c), bottom (b) and top (t). Quarks obey the strong, weak and electromagnetic interactions and under standard conditions can only be found in bound states known as hadrons. This can be explained by the so-called colour confinement. Leptons however, are free in existence as they do not carry any colour charge. The six different leptons can be divided into the charged leptons electron ( $e^-$ ), muon ( $\mu^-$ ) and tau ( $\tau^-$ ) and their respective neutral leptons also known as neutrinos ( $\nu_e$ ,  $\nu_\mu$  and  $\nu_\tau$ ). Each of the particles also has an anti-particle, for example  $e^+$  as anti-particle of  $e^-$  and  $\bar{\nu}_e$  for  $\nu_e$ . The charged leptons can interact weakly and electromagnetically whereas the neutrinos are only able to interact weakly. This is because they are not electromagnetically charged.

Ordinary matter consists of fermions of the first generation. These particles can form hadronic matter like neutrons and protons consisting of up and down quarks. Together they form atomic nuclei and along with electrons surrounding the atomic nuclei they form the ordinary matter we experience in everyday life. As an example for neutrinos in general, electron neutrinos are created in  $\beta^+$  decays.

### 1.3 Quantum Chromodynamics (QCD)

Quantum Chromodynamics (QCD) is a quantum field theory that describes the strong interaction. As seen before, the mediators of the strong interaction are the eight massless coloured gluons. In this context, colour describes an additional degree of freedom which occurs due to the underlying invariance under SU(3) local phase transformations associated with QCD. The colours are usually referred to as red, blue and green as well as the anti-colours anti-red, anti-green and anti-blue. The eight gluons, which correspond to the eight generators of the SU(3) local gauge symmetry, couple to coloured quarks and antiquarks as well as other gluons by exchanging colour. As stated by the

hypothesis of colour confinement, coloured objects are always confined to colour singlet states and thus only colour neutral objects can be observed [3].

In non-relativistic QCD, the potential between a quark and an antiquark can be described as

$$V_{q\bar{q}}(r) = -\frac{4}{3} \frac{\alpha_s}{r} + \kappa r \quad (1.1)$$

where  $r$  is the distance between the quark and the antiquark,  $\alpha_s$  is the coupling constant of the strong interaction and  $\kappa$  a string constant. The latter describes the long-range potential due to colour confinement.

Even though being described as the strong coupling *constant*,  $\alpha_s$  is dependent on the

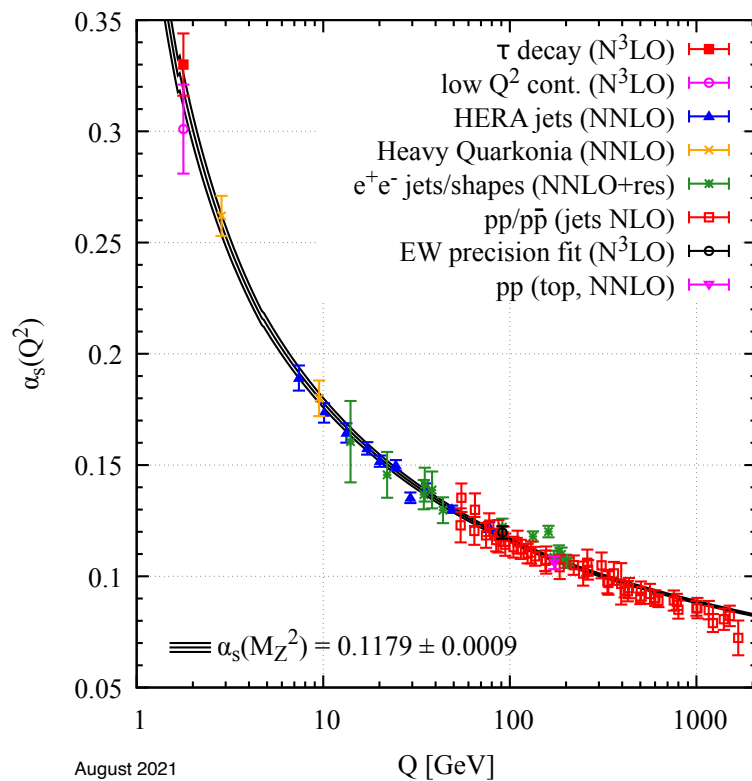


Figure 1.2: Summary of measurements of  $\alpha_s$  as a function of the energy scale  $Q$ . The black line shows the fit. [4]

energy scale as seen in figure 1.2 and was calculated (to leading order) as

$$\alpha_s(Q^2) = \frac{12\pi}{(33 - 2N_f) \ln(Q^2/\Lambda_{QCD}^2)} \quad (1.2)$$

with  $Q^2 \gg \Lambda_{QCD}^2$  [5]. Here,  $Q$  is the momentum transfer and  $N_f$  is the number of involved quark flavours.  $\Lambda_{QCD} \approx 200$  MeV is the fundamental QCD scale parameter.

For small momenta, the QCD coupling constant is large. Thus, perturbation theory is not applicable. But for high-momentum regimes, perturbative QCD can be used because the coupling constant gets small enough. This is called running of  $\alpha_s$ .

## 1.4 Quark-gluon plasma (QGP)

The asymptotic freedom as a property of QCD leads to a new, deconfined phase of matter called quark-gluon-plasma (QGP). It is created, when temperature or density become very high and strongly interacting quarks and gluons become free [6]. In order to produce QGP, heavy-ion collisions are used: The incident nuclei are accelerated to ultrarelativistic velocities and are Lorentz contracted discs rather than the ordinary model of sphere-like objects.

With increasing energy density, a phase transition to deconfined matter happens. The energy density increases as many new degrees of freedom get liberated around the deconfinement temperature [7]. This is the case, as in deconfined matter free quarks and gluons are available instead of hadrons that are bound states of quarks. As QGP can be formed at very high densities, QGP may be found at the centres of neutron stars [8]. In addition, QGP can also form at high temperatures, which is why QGP is believed to have formed very shortly after the Big Bang before cooling down and hadronising. However, studying the early universe or neutron stars is not directly possible but heavy-ion collisions establish an opportunity to do so.

As displayed in figure 1.3, the QCD phase diagram can be represented as a function of temperature and baryon chemical potential. One can see that QGP only exists at high temperatures and/or densities whereas the ordinary world consists of hadronic matter with quarks and gluons being confined to hadrons. Ordinary matter exists at finite temperatures  $T \approx 0$  MeV and a baryon chemical potential of  $\mu_B \approx 1$  GeV, which is a measure for the balance between matter and antimatter. The critical temperature for the phase transition between ordinary hadronic matter and QGP in the limit of zero baryon chemical potential is predicted to be at  $T_c = (156.5 \pm 1.5)$  MeV [9] using lattice QCD. This corresponds to around  $10^{12}$ K.

After the QGP has formed, it quickly expands and starts to cool. Eventually rehadronises as it passes the critical temperature again. Hadronisation describes the phase transition from the QGP phase to the Hadron Gas phase. In the latter also our normal matter known by everyday life is included. As shown in figure 1.3, the Hadron Gas phase also contains vacuum as a state with ideally no matter and Nuclear Matter consisting out of nuclei, thus quarks bound to protons and neutron which are then again bound with each other. The phase diagram could be completed with the Colour Superconductor phase in which the colour charge becomes superconducting. This is speculated to happen a high baryon chemical potential and low temperature [8].

In conclusion, the exploration of quark-gluon plasma is a central aspect in unravel-

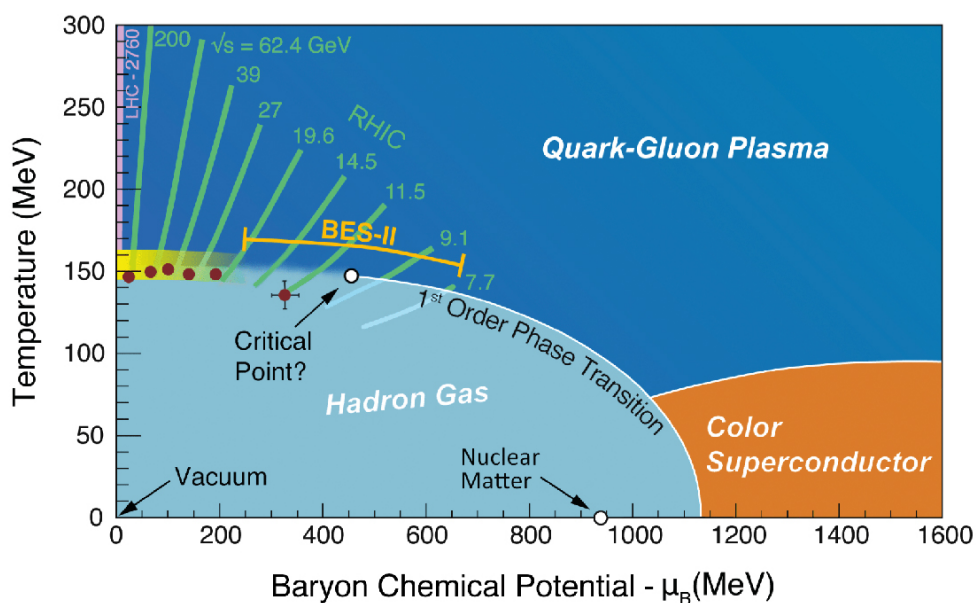


Figure 1.3: QCD phase diagram as a function of temperature  $T$  and baryon chemical potential  $\mu_B$ . The light blue area describes the hadron gas and the dark blue the QGP. The lines represent the results from present/future experiments [8].

ling the complex phases of nuclear matter evolution. As the QGP rehadronises it experiences the journey from extreme temperatures and energy densities to familiar everyday matter. This offers an opportunity to study the underlying principles of Quantum Chromodynamics. The study of QGP is not only a possibility to get to know the conditions of the early universe but also a way to understand the strong force and its role in shaping the structure of matter.

# 2 The ALICE experiment

## 2.1 Large Hadron Collider (LHC)

In this thesis, data from the ALICE experiment will be used for analysis. ALICE, which stands for "A Large Ion Collider Experiment", is situated at the European Organisation for Nuclear Research (CERN, an abbreviation for "Conseil Européen pour la Recherche Nucléaire") in Geneva, Switzerland. CERN is the largest research centre for particle physics and the Large Hadron Collider (LHC), one of the accelerators at CERN, is the world's largest particle accelerator. It is capable to achieve a centre of mass energy of  $\sqrt{s} = 13.6$  TeV in proton-proton (pp) collisions in Run 3 after upgrades in the last shutdown, the Long Shutdown 2 (LS2) which lasted from December 2018 until April 2022. As of the end of September 2023, for lead-lead (Pb-Pb) collisions a center of mass energy per nucleon pair of  $\sqrt{s_{NN}} = 5.36$  TeV has been reached [10].

The LHC, having a circumference of 26.7 km and being situated on Swiss and French terrain, was installed in the tunnel that previously housed the Large Electron-Positron Collider (LEP). The LHC accelerates bunches of protons as well as heavy ions and collides these at four different interaction points along the beam line. These offer the possibility for detectors specialised on different physics questions to be installed. There are four main experiments: ATLAS and CMS are dedicated to high luminosity and are known for the discovery of the Higgs Boson in 2012. LHCb studies beauty physics and ALICE is optimised for the investigation of quark-gluon plasma. In addition there are several smaller experiments along the LHC beam line. To be able to accelerate the protons or lead ions respectively, to the extreme energies reached, a succession of particle accelerators is used to produce beams of protons or heavy ions. Protons, that originally stem from hydrogen ions  $H^+$ , are accelerated to achieve an energy of  $\sqrt{s} = 6.8$  TeV [12].

Lead ions however, stem from pure lead ions that are gradually stripped from their electrons and get accelerated. This leads to  $Pb^{82+}$  ions that are injected in the LHC in up to 1248 bunches per beam [13].

## 2.2 A Large Ion Collider Experiment (ALICE)

At CERN, particles were first accelerated in 1959 and LHC's predecessor LEP operated from 1989 until 2000 [14]. In 1993, the ALICE experiment was officially proposed [15] and in 2009, the first data could be recorded. The main purpose of ALICE is the study of QGP.

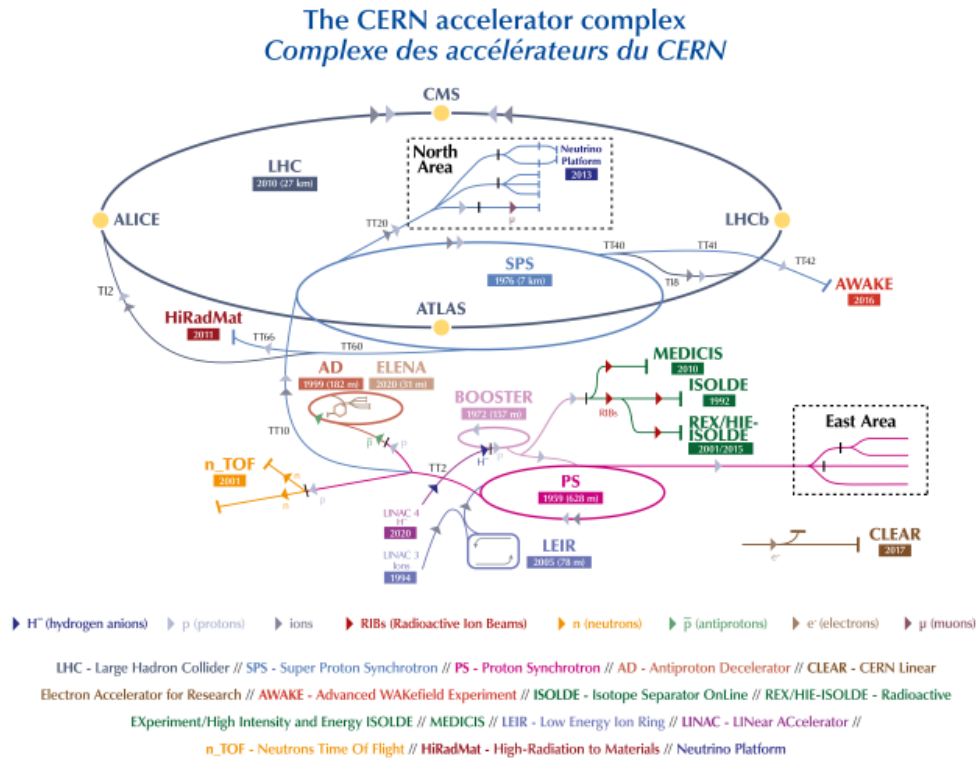


Figure 2.1: The CERN accelerator complex [11]

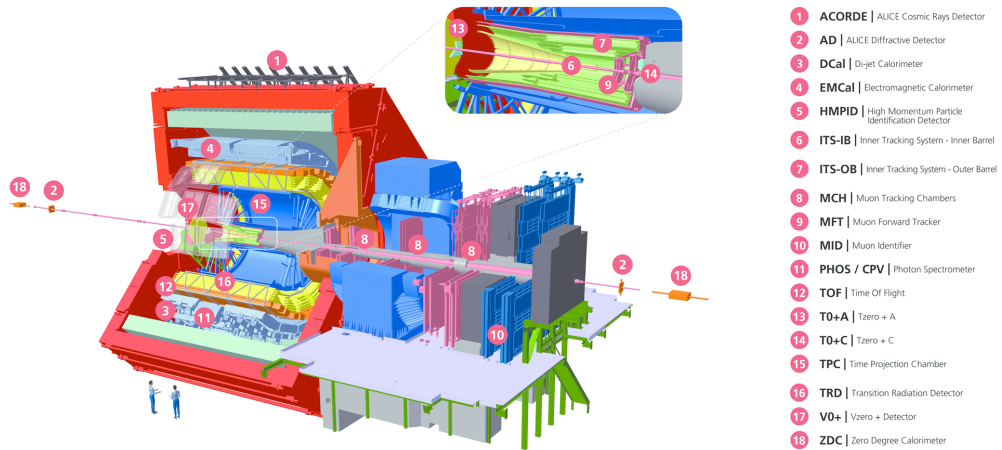


Figure 2.2: Overview of the ALICE detector in Run 3 [16]

As seen in figure 2.2, except for the muon-arm, the detector is mostly built inside the L3 magnet in mid-rapidity which was "inherited from the former LEP experiment L3" [17]. The tracking is mostly done by the detectors of the central barrel. These

are the Inner Tracking System (ITS), the Time Projection Chamber (TPC) and the Transition Radiation Detector (TRD). These will be described in detail in the following sections. Apart from them, the ALICE detector consists of further components: In radial direction, after the TRD the Time-of-Flight detector (TOF) is placed, which measures the time each particle takes from the vertex to the TOF itself. Following the TOF, calorimeters as the Di-jet Calorimeter (DCal) and the Electromagnetic Calorimeter (EMCal) are installed as well as the Photon Spectrometer (PHOS) and, at the outside of the L3 magnet, the ALICE Cosmic Rays Detector (ACORDE) is placed to measure cosmics. On the side of the L3 magnet in forward-rapidity, the muon-arm is situated which consists of different parts of different parts designated to measure muons.

### 2.2.1 Inner Tracking System (ITS)

As the ALICE detector was upgraded during LS2, so the Inner Tracking System 2 (ITS2) [18, 19] was installed replacing the ITS [20] as a key element thereof. The ITS is the innermost detector of the whole experimental apparatus and therefore the first particles are passing through after the collision. Its main purpose is the determination of the primary and secondary vertices and tracking of low-momentum particles [15]. Another aim is the improvement of the momentum resolution for high-momentum particles by matching their tracks captured in the TPC to those in the ITS. The performance of those tasks has been enhanced by the installation of ITS2. In comparison to the previous ITS, ITS2 has three main improvements:

First, the resolution of the impact parameter was ameliorated by a factor of 3 in the  $r\varphi$  coordinate and a factor of 5 along the beam axis (the  $z$ -coordinate), respectively. Second, the tracking efficiency and the  $p_T$  resolution at low-momentum are going to be improved by the increased detector's granularity. Third, the readout rate was increased to 200 kHz in pp and up to 100 kHz in Pb-Pb collisions.

Figure 2.3 shows a schematic overview of the ITS and its layers divided in Inner and Outer barrel. The radius of the beam pipe is reduced in the middle of the detector. This is depicted in the comparison of the blue and the red part of the beam pipe in the figure. This feature was used to move the detector closer to the interaction point to now 23 mm for the innermost layer. In addition, the material budget of the inner layers was reduced from  $1.14\%X_0$  to now  $0.35\%X_0$  along with reducing the pixel size from  $50\ \mu\text{m} \times 425\ \mu\text{m}$  to  $29.24\ \mu\text{m} \times 26.88\ \mu\text{m}$  in order to achieve the improved resolution and granularity. As seen in figure 2.3 the ITS is divided in the Inner Barrel (IB) and the Outer Barrel (OB) consisting of three and four layers respectively. The OB is further divided in the Middle Layers (MLs) and Outer Layers (OLs). The radial position of each layer is shown in table 2.1. Thus, the ITS covers a radial range from 23 mm to 400 mm.

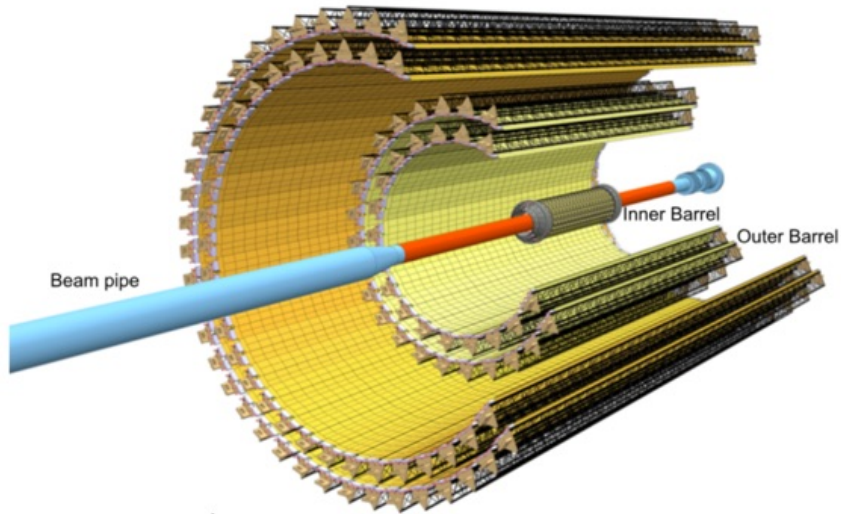


Figure 2.3: Layout of ITS2 [18]

The ITS is equipped with ALPIDE chips [19]. These are Monolithic Active Pixel Sensors (MAPS) based on CMOS technology. The advantage of using MAPS instead of hybrid pixel detectors is that MAPS consist only of one silicon layer, as the detection volume and the readout electronics are combined. This allows a significant reduction of material budget since in comparison to hybrid pixel detectors they can be thinned easily and they only consist of one layer instead of two separate layers. In addition, the significantly reduced pixel size leads to a better resolution of the detectors.

	Inner Barrel			Outer Barrel			
	Inner Layers			Middle Layers		Outer Layers	
	Layer 0	Layer 1	Layer 2	Layer 3	Layer 4	Layer 5	Layer 6
$R_{min}$ [mm]	22.40	30.10	37.80	194.40	243.90	342.30	391.80
$R_{max}$ [mm]	26.70	34.60	42.10	197.70	247.00	345.40	394.90

Table 2.1: Radii of the different layers of ITS2 [18]

Component	$R_{min}$ [mm]	$R_{max}$
Outer Barrel CYSS <sup>1</sup>	449	461
MFT Barrel	496	508
ITS Cage	540	550

Table 2.2: Structural components of the ITS2 [18, 21]

<sup>1</sup>CYSS - Cylindrical Structural Shell

### 2.2.2 Time Projection Chamber (TPC)

The ALICE Time Projection Chamber (TPC) shown in figure 2.4 is the main tracking and particle identification instrument. It has a cylindrical shape, is filled with gas and uses the fact that charged particles ionise the gas which they traverse. The TPC

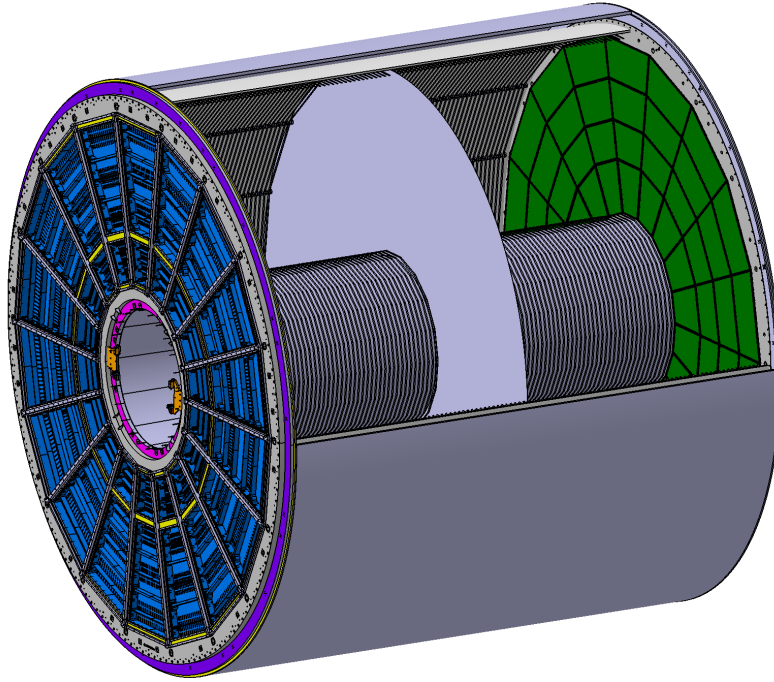


Figure 2.4: Schematic overview of the TPC [22]

has an active volume of  $88\text{ m}^3$  and encloses the ITS. Its radius ranges from 85 cm to 250 cm and its active volume has a length of about 500 cm [23]. In its centre, a high-voltage electrode is installed dividing the active volume in two halves and to provide an electrical field between the endplates and the said electrode. Furthermore, each endplate consist of 18 inner and outer readout chambers (IROCs and OROCs). These are arranged in pairs resulting in 18 equal azimuthal sectors [22]. For tracks with full radial track length, the TPC covers a pseudo-rapidity of  $|\eta| < 0.9$  and it covers the full azimuth except of the dead zones [23]. The spaces between two neighbouring readout chambers including the frames are referred to as dead zones. Here, no readout is possible. The detector is filled with a gas mixture consisting of  $Ne - CO_2 - N_2$  (90-10-5), so 90 parts of Ne, 10 parts of  $CO_2$  and 5 parts of  $N_2$ . In LS2, the TPC was upgraded to be able to handle a rate of up to 50 kHz Pb-Pb collisions. A collision rate this high leads to a pile up of multiple collision events within the former TPC drift time. Thus, a continuous readout is needed and the readout chambers used in the previous runs were replaced by Gas Electron Multiplier (GEM) detectors. GEMS

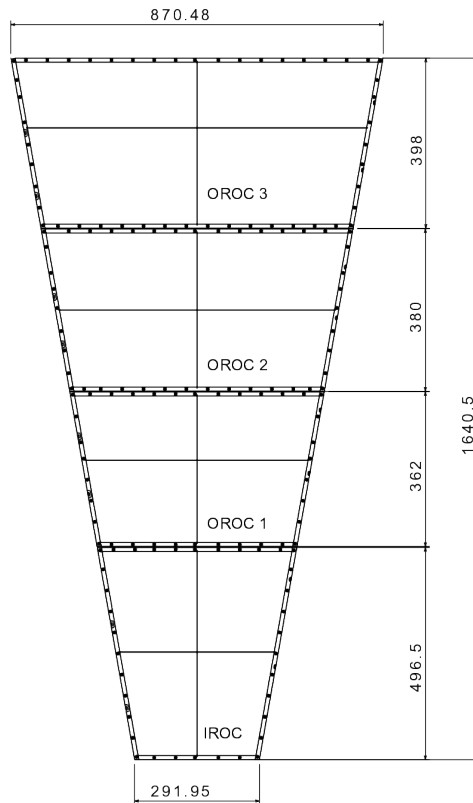


Figure 2.5: Overview of an ALICE TPC sector, consisting of an inner and an outer readout chamber [22]

are electron multipliers and therefore amplify the signal without leading to too many electrical charges flowing back in the gas filled detector. GEMs provide the needed amplification of the ionisation charges without any dead-time and therefore serve the continuous readout. The layering of four GEM foils only allows very little ion back flow while still being able to identify particles. As seen in figure 2.5, a ROC is based on a trapezoidal frame and consists of one IROC and three OROC stacks. For each GEM a different potential difference is applied.

### 2.2.3 Transition Radiation Detector (TRD)

As the name of the Transition Radiation Detector (TRD) indicates, this part of the ALICE detector uses Transition Radiation (TR). This phenomenon occurs, when a charged particle traverses a boundary between two different media with different refractive indices at relativistic velocity. It allows to distinguish electrons from hadrons as electrons produce TR and also have a higher  $dE/dx$  because of the relativistic rise of the ionisation energy loss. In addition it provides triggering and contributes to track reconstruction and calibration in the central barrel. The ALICE TRD covers the full azimuth and

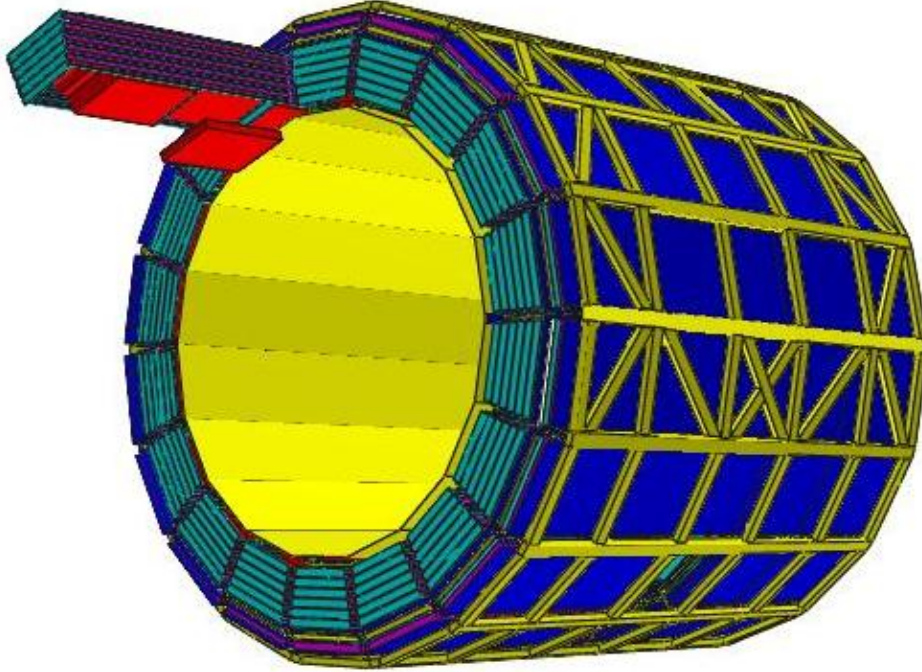


Figure 2.6: Overview of the ALICE TRD [24]

the pseudo-rapidity range of  $|\eta| < 0.84$ . As seen in figure 2.2, where the TRD is labelled with the number 16, the TRD encloses the previously discussed detector parts. The TRD has a modular structure and uses Multiwire Proportional chambers (MWPC) (see fig. 2.4). Those are filled with a Xe- $CO_2$ -mixture, dividing the azimuth in 18 sectors to match the TPC readout chambers. Along the beamline, each sector is split into five stacks. Furthermore, each stack is arranged in six layers at a radial distance from 2.90 m to 3.68 m from the beam axis. This results in a total of 540 readout chambers ( $18 \text{ sectors} \times 6 \text{ layers} \times 5 \text{ stacks}$ ), yet only 522 readout chambers were installed to minimise the material in front of the PHOS detector [25]. In addition, in each chamber, a radiator is installed mounted in front of a drift region and then followed by a MWPC. As seen in figure 2.7, photons are produced via TR by electrons in the radiator. Those are then absorbed in the MWPC. By contrast, the pion traversing the radiator does not lead to the emission of a photon. This allows the distinction between electrons and other charged particles.

#### 2.2.4 Time-of-Flight detector (TOF)

The aim of the Time-of-Flight detector (TOF) is to contribute to the particle identification. As the name suggests, this is done via measuring the time of flight of a

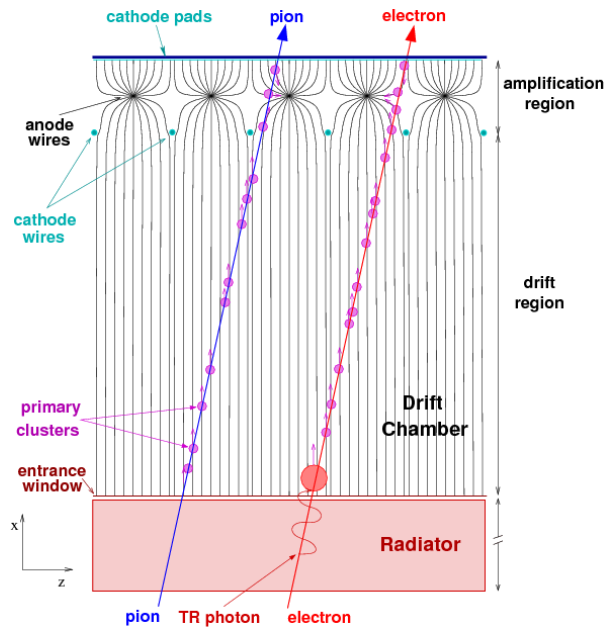


Figure 2.7: Schematic cross-sectional view of a ALICE TRD chamber [26]

particle. In order to be able to correctly identify particles, a good time resolution of a TOF detector is crucial. Therefore, the ALICE TOF has been designed to get a time resolution as small as possible [27]. Particle identification is possible via the mass squared, which can be obtained in the following way: The time of flight  $\Delta t$  is measured between two points with known distance  $L$ . This is used to calculate the velocity  $\beta = L/c\Delta t$  of a particle and thus, the squared mass can be extracted by combining  $\beta$  with the momentum  $p = \beta\gamma mc$  [28, 29] known from the measurement in the TPC via

$$m^2 = \frac{p^2}{c^2} \left( \frac{c^2(\Delta t)^2}{L^2} - 1 \right). \quad (2.1)$$

The TOF consists out of a large array of Multi-gap Resistive-Plate Chamber (MRPC) strip detectors. A resistive plate chamber (RPC) uses a homogeneous electric field between plates that are placed parallel next to each other. The plates have a small gap between each other which is filled with a gas. A sufficient high electric field is used so that an incoming particle creates an instant avalanche that can then be measured. The gas is used to put any point in the detector into use. The space between two plates is so small that only negligible drift to the plate occurs before an avalanche sets in [28]. In contrast to a single-gap RPC, a MRPC consists of multiple gas-filled gaps separated by more resistive plates. The use of MRPCs improves the time resolution with the number of gaps.

The TOF is located at a radial position of 3.7 m and covers a pseudo-rapidity of  $|\eta| <$

0.9. As the TPC and the TRD, the TOF is segmented in 18 supermodules which can be seen in figure 2.8. Each supermodule contains 91 MRPC strips and each of them is divided in 96 pads. As resistive plates soda-lime glass is used. The TOF covers the full azimuth except for holes left to disturb particles as little as possible while reaching the PHOS [30]. In LS2, the TOF's readout electronics were updated to implement a

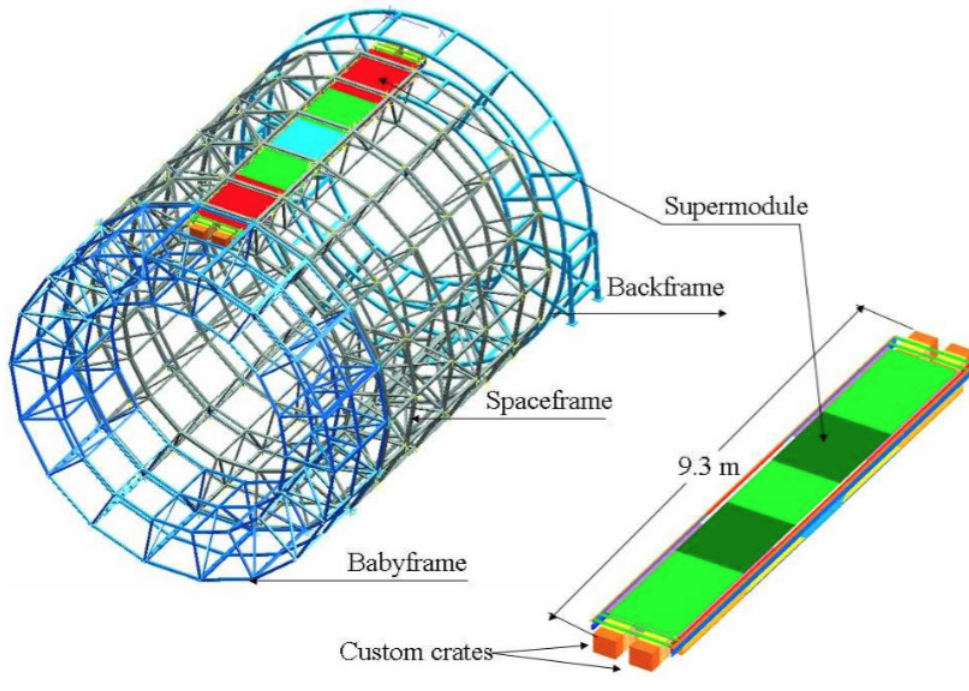


Figure 2.8: Schematic overview of the TOF detector [30]

continuous readout matching the ITS and the TPC. Another goal of the upgrade was to maximise the discrimination ability of the TOF concerning particle identification for intermediate momentum. Therefore, a periodic trigger with a frequency of 33 kHz was implemented to mimic a continuous readout[16].

# 3 Interaction processes of photons and electrons

## 3.1 Interactions of photons with matter

In the Standard Model, the photon  $\gamma$  is introduced as a gauge boson having spin 1. It is the mediator of the electromagnetic force. Photons can be described as electromagnetic radiation, they are mass- and charge-less and thus travel always with the speed of light. Because of it's properties, one can not detect a photon directly and rather must rely on the photon's interaction with matter. In the following section, the *photoelectric effect*, *Compton scattering* and *pair production* will be explained.

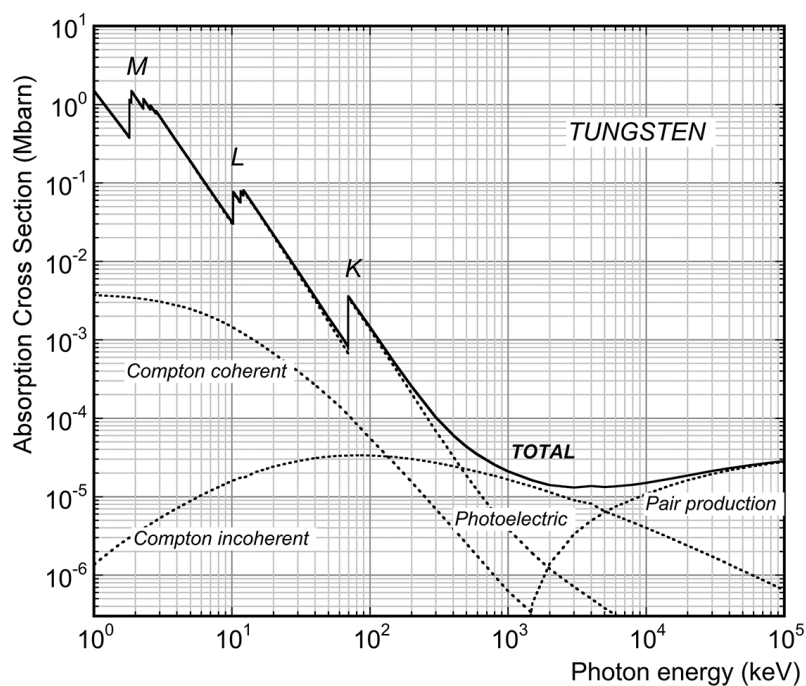


Figure 3.1: Absorption cross section of photons and its different components [31]

### 3.1.1 Photoelectric effect

The photoelectric effect describes an interaction of a photon together with an absorber atom. The photon is fully absorbed by an electron in one of the shells of the atom. This electron is the emitted (see figure3.2). The photoelectric effect can only take

place with an atom and not a free electron, as in this case, energy and momentum conservation would be violated. The energy of the electron is thus given by

$$E_{kin}^{e^-} = h \cdot \nu - E_b \quad (3.1)$$

with the binding energy  $E_b$  of the electron in its original shell and the frequency of the photon  $\nu$ . The cross-section of the photoelectric effect strongly depends on the atomic

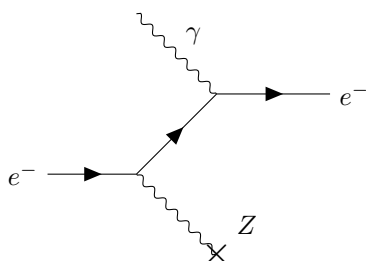


Figure 3.2: Feynman diagram of the photoelectric effect

number  $Z$  as well as the photon energy  $E_\gamma$ . A dependency can be expressed as

$$\sigma_{ph} \propto \frac{Z^n}{E_\gamma^m} \quad (3.2)$$

with  $n = 4 - 5$  and  $m \lesssim 3.5$  [28].

### 3.1.2 Compton scattering

As one can see in figure 3.1, Compton scattering is the dominant energy loss for photons with intermediate energy from around 50 keV to 500 keV. Unlike the photoelectric effect, Compton scattering does not require a nucleus to be present. The scattering of the photon is possible off a free or quasi-free electron. Here, a quasi-free electron is a shell electron whose binding energy is much smaller than the energy of the photon scattering.

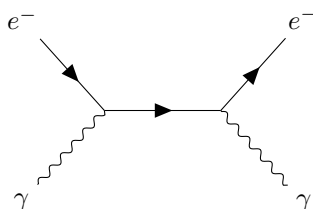


Figure 3.3: Feynman diagram of Compton scattering

The incoming photon in fig. 3.3 is scattered off an electron with an angle  $\theta$  with respect its original direction. Within this process, a portion of the photon energy  $E'_\gamma$  is

transferred to the Compton electron. Contrary to the photoelectric effect, here also a photons is going out. The energy of the outgoing photon as a function of the scattering angle is

$$E'_\gamma = \frac{E_\gamma}{1 - \frac{E_\gamma}{m_e c^2} (1 - \cos \theta)}. \quad (3.3)$$

Looking at an absorber, the probability that Compton scattering occurs depends on the number of electrons available in each atom. Thus, the cross section is linearly dependant of  $Z$ . Therefore, the cross section is approximately given by

$$\sigma_c \propto \frac{Z}{E_\gamma} \quad (3.4)$$

### 3.1.3 Pair production

For sufficiently high photon energies ( $\gtrsim 1$  MeV, pair production becomes the dominant effect. In this process, the photon converts into an electron-positron pair as seen in figure 3.4. In order to do so, the presence of an atomic nucleus is required to ensure the conservation of energy and momentum. The nucleus absorbs just a small fraction of the energy of the photon. In addition, the angle between the converted electron and positron is very small for high momentum photons because of momentum conservation.

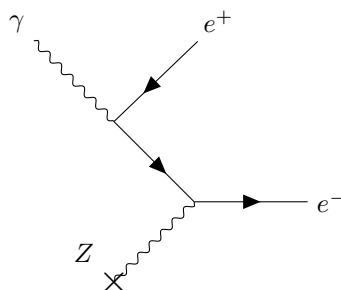


Figure 3.4: Feynman diagram of the pair production process

For high energies, the pair production process dominates. For this reason, the differential cross section for the full photon absorption cross section can be used as an approximation. It is given by

$$\frac{d\sigma}{dx} = \frac{A}{X_0 N_A} \left( 1 - \frac{4}{3} x(1-x) \right) \quad (3.5)$$

with  $A$  as the atomic number of the material and  $N_A$  the Avogadro constant.  $X_0$  is the radiation length and  $x = E_e/E_\gamma$  is the fractional energy the electron receives. Hence, the differential cross section can be integrated to get the high energy limit for the pair

production cross section:

$$\sigma_{pair} = \frac{7}{9} \frac{A}{X_0 N_A} \quad (3.6)$$

## 3.2 Interactions of electrons (positrons) with matter

The interactions described above all create electrons, which can then be detected to gather information about the photon.

Electrons and positrons as charged particles loose energy when traversing matter. The energy can be lost by *ionisation* or by radiation such as *Bremsstrahlung*, *transition radiation* or *Cherenkov radiation*.

### 3.2.1 Ionisation

When a charged particle passes through a medium, it loses energy via ionising or exciting the atoms of the medium. The energy loss can be described with the Bethe-Bloch-formula

$$-\left\langle \frac{dE}{dx} \right\rangle = K \rho z^2 \frac{Z}{A} \frac{1}{\beta^2} \left[ \frac{1}{2} \ln \left( \frac{2m_e c^2 \beta^2 \gamma^2 T_{max}}{I^2} \right) - \beta^2 - \frac{\delta}{2} - \frac{C}{Z} \right] \quad (3.7)$$

with the following quantities [28]:

- $K = 4\pi N_A r_e^2 m_e c^2$
- $z, \beta$ : charge and velocity of the particle
- $I$ : mean excitation energy
- $T_{max} = \frac{2m_e c^2 \beta^2 \gamma^2}{1 + 2\gamma m_e/M + (m_e/M)^2}$ : maximum possible energy transfer to a shell electron with  $M$  being the mass of the particle
- $\delta$ : density correction
- $C/Z$ : shell correction

In this formula, the energy loss is given per path length which corresponds to the amount of matter having been traversed. As described in equation 3.7, the  $1/\beta^2$  term is dominant at low energies and the  $\ln\gamma$  term at high energies. This leads to a minimum of the energy loss between the two regions which is around  $\beta\gamma \approx 3$ .

The energy loss at low energies is marked by the  $1/\beta^2$  dependency. This can be explained by the momentum transfer. At low energies, the momentum transfer increases as the effective interaction time is longer for slower particles.

The rise for high energies can be explained by two phenomena. First, the maximum energy transfer  $T_{max}$  increases asymptotically with the limit  $T_{max} \rightarrow \gamma M c^2 = E$  for

$\gamma \rightarrow \infty$ . Second, with increasing  $\gamma$  the relativistic effects become more prominent: The electric field extends to atoms of the medium further away from the particle to interact with it. This effect gets however limited by the polarisation of the medium as the nearby atoms shield the charge of the particle. Therefore, the energy loss saturates in the so-called Fermi plateau at high energies.

### 3.2.2 Bremsstrahlung

While traversing matter, charged particles not only loose energy by ionisation but also by Bremsstrahlung. This occurs when the particles crosses the electric field of nuclei and therefore gets decelerated. To conserve energy, this results in the emission of a photon. The energy loss can be described by [32]:

$$-\frac{dE}{dx} = 4\alpha N_A \left( \frac{e^2}{mc^2} \right)^2 \ln \frac{183}{Z^{1/3}} \frac{Z(Z+1)}{A} Q^2 \cdot E \quad (3.8)$$

with the fine-structure constant given by  $\alpha = e^2/(4\pi\epsilon_0\hbar c)$ , the charge and mass of the incoming particle  $Q, m$ , the atomic number  $Z$  and the atomic mass number  $A$ . As the equation is highly dependant in the particle mass,

$$-\frac{dE}{dx} \sim \frac{1}{m^2} \quad (3.9)$$

Bremsstrahlung is only dominant for electrons and positron whereas it can be mostly neglected for heavier particles in the relevant energy regime. For electrons and positrons, Bremsstrahlung dominates at higher energies above an energy of a few tens of MeV in most materials. For the electron as the incoming particle, the radiation length can be introduced via

$$-\frac{dE}{dx} = \frac{1}{X_0} E \quad (3.10)$$

with the material dependent constant  $X_0$  given by

$$\frac{1}{X_0} = 4\alpha N_A \left( \frac{e^2}{m_e c^2} \right)^2 \ln \frac{183}{Z^{1/3}} \frac{Z(Z+1)}{A}. \quad (3.11)$$

### 3.2.3 Transition and Cherenkov radiation

When a charged particle travels through a medium with a velocity  $\beta = v/c$  that is higher than the speed of light in the medium given by  $\beta_m = \beta/n$  with the refraction index  $n$ , photons get emitted. They are emitted under the Cherenkov angle given by

$$\cos(\theta_c) = \frac{1}{n\beta} \quad (3.12)$$

Charged particles polarise atoms in the medium when traversing the material. If the velocity of the particle becomes larger than the speed of light in the material, the polarised particles are no longer distributed symmetrically with respect to the flight direction but they distributed asymmetrically. Therefore, a dipole is created which emits an electromagnetic pulse. The waves propagate with the speed of light of the medium and superimpose constructively resulting in a wavefront with the Cherenkov angle given in equation 3.12.

Similarly, when a particle crosses the boundary between two different dielectrics with different refraction indices, photons can be emitted as transition radiation. As a charged particle in a dielectric medium approaches the boundary to a medium with different dielectric properties, the electric field configuration changes. As a continuous transition is required, electromagnetic radiation is then emitted. The angular distribution of the energy is peaked at

$$\theta_t \simeq \frac{1}{\gamma}. \quad (3.13)$$

with  $\gamma$  being the Lorentz factor.

# 4 Photon Conversion Method (PCM)

In this chapter, an overview on the photon reconstruction using PCM is given. For that, the V0 reconstruction is explained as well as the cuts in order to select photons from the complete V0 sample. In a next step, the data sets analysed in this thesis are introduced. Lastly, the analysis chain for the investigation of the material budget in chapter 5 as well as the study on the photon momentum resolution using the pion invariant mass in chapter 6 are described.

## 4.1 V0 Reconstruction and Photon Identification

In ALICE, the photons measured have transverse momenta of  $p_T \gtrsim 100$  MeV/c which is why photon conversion is the main process. Particles with lower momentum will bend too much and won't reach the detectors to measure them. A possible way to reconstruct the photon conversions is by tracking the conversion products.

Photon conversions are not decays but they can be treated like that as two oppositely charged particles (electron and positron) are emitted from the same point (conversion vertex),

$$\gamma \rightarrow e^+ + e^-. \quad (4.1)$$

Because of that, one can search for vertices of V0s to reconstruct photons. V0s are particles that cannot be detected directly due to their neutral charge in most detectors. However, photons for example can be detected in electromagnetic calorimeters and neutral hadrons in hadronic calorimeters. Examples for V0s are the photon  $\gamma$  discussed here but also  $K_S^0$ ,  $\Lambda$  and  $\bar{\Lambda}$ .

In general, a V0 can be reconstructed by matching displaced tracks with opposite charge. Later in the analysis, these will correspond to the electron and positron. In figure 4.1, the geometry of the reconstruction of a secondary vertex is shown. First, one chooses a track with an impact parameter  $b$  that is large enough. Then all tracks with opposite charge are matched with this track. On those tracks, several selection criteria are applied. These are for example:

- a large enough impact parameter  $b$
- a small enough distance of closest approach (DCA)
- their point of closest approach (PCA) has to be closer to the primary vertex than any of the measured points of the tracks

- the cosine of the pointing angle has to be greater than a certain boundary. The pointing angle is the angle between the total momentum of the two particles and the line that connects the primary and the secondary vertex.

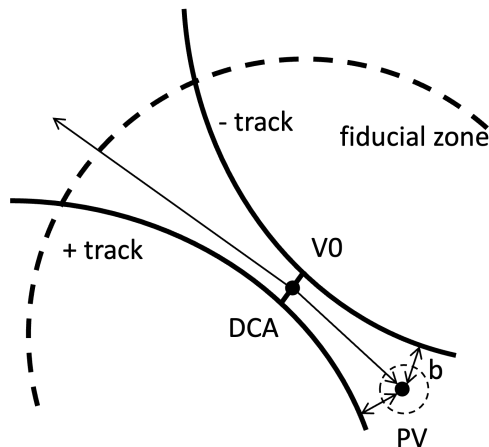


Figure 4.1: Geometry of the reconstruction of a secondary vertex. (figure inspired by [33])

The next step is then to select photons among all V0 candidates. To be able to reconstruct photons from electron positron pairs, different cut sets are going to be applied in order to differentiate the electron positron pairs from other charged particles in the V0 sample and the photons from other V0s. This ensures to extract physically possible conversions and reduces contamination from other decays.

To differentiate the reconstructed photons, different cuts are defined. The complete list of cuts and applied values is given in table 4.1. As one feature, they distinguish which track segments are required: The cut ITSTPC requires tracks in the ITS as well as the TPC whereas the cut TPCOnly requires tracks only in the TPC. The cuts analysis and qc (quality control) have similar properties but the cut analysis requires slightly stricter limits for the cosine of the pointing angle as well as the point of closest approach.

During the analysis of the material budget, only the cut qc is going to be used. For the estimation of the calibration weights, also the wire cut is needed. As mentioned in the introduction, calibration wires were installed in the ITS2. This cut allows the reconstruction of the photons that have converted in the material of the calibration wires. For the wire-based estimation of the calibration weights, it is necessary to have one cut that assigns reconstructed photons to the wires.

For the investigation of the photon momentum resolution, the analysis will be performed for four different cuts (analysis, qc, ITSTPC and TPCOnly) in order to compare them and the properties of the different data sets.

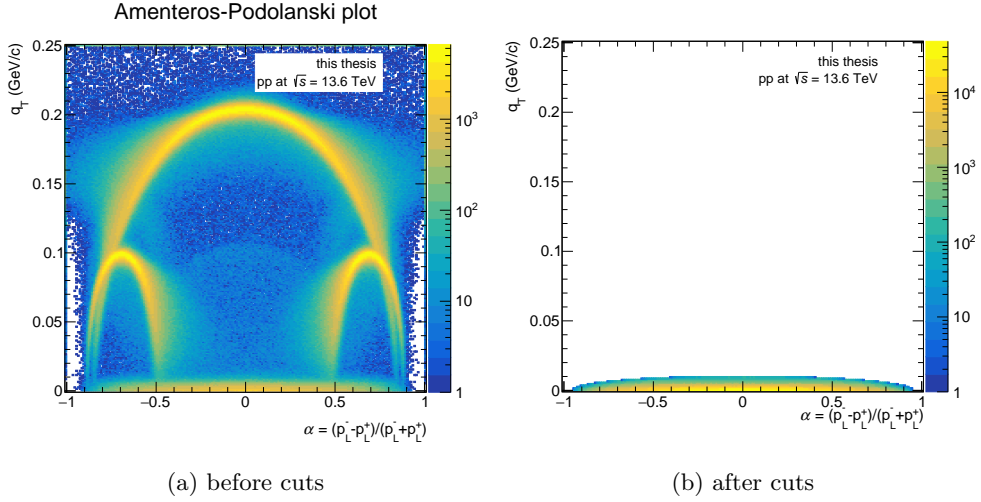


Figure 4.2: Armenteros-Podolanski distribution for V0 candidates. On the left no cuts are applied. On the right the selection cuts for data LHC22f for the cut  $q_c$  are applied.

As a first selection, a minimum track momentum of 0.02 GeV/c is required to ensure a good track quality as well as the minimum number of crossed rows in the TPC of 20 rows and a minimum of crossed rows over findable clusters in the TPC of 80%. In addition it is required that the tracks are propagated to within the beam pipe, i.e. the inner region of the beam pipe. The track selection criteria are the same for all the cuts except the cut *wuire*. However, this cut is only used for the wire-based calibration method and not for the analysis. The track selection cuts applied on the cuts used for the analysis can be seen in table 4.1.

Those selection criteria were all applied to the tracks. In addition, criteria are going to be applied on TPC particle identification (PID) to identify the tracks as electrons as well as on the reconstructed V0 to identify it as a photon.

The goal of the particle identification cuts applied on the secondary tracks is to identify electrons and positrons and to reject pions and protons. For that, the TPC energy loss distribution can be used and tracks are accepted if they have an energy loss within  $\pm 3\sigma$  from the expected electron  $dE/dx$ .

As the selected tracks and their reconstructed V0s still contain combinatorial background, cuts are applied on the reconstructed V0. To do so, an Armenteros-Podolanski plot is used (see figure 4.2). It shows the longitudinal momentum asymmetry  $\alpha$  between the secondary tracks with respect to the transverse momentum  $q_T$ . The longitudinal momentum asymmetry is defined by

$$\alpha = \frac{p_L^{e^+} - p_L^{e^-}}{p_L^{e^+} + p_L^{e^-}} \quad (4.2)$$

Cuts used in the analysis					
	analysis	qc	qc_ITSPC	qc_TPConly	wwire
<b>Track cuts</b>					
Track $p_T$ (GeV/c)			$0.02 < p_T < 10^{10}$		$0.02 < p_T < 10^{10}$
Min $N_{\text{crossed rows TPC}}$			20		20
Min $N_{\text{crossed rows}}/N_{\text{findable clusters TPC}}$			$> 80\%$		$> 80\%$
$\chi^2/\text{Cluster TPC}$			$0.0 \leq \chi^2 \leq 4.0$		$0.0 \leq \chi^2 \leq 4.0$
TPC $N\sigma$ Electron			$-3 \leq \sigma \leq +3$		$-4 \leq \sigma \leq +4$
Within beam pipe			true		-
<b>Cuts on the V0</b>					
$p_T$ (GeV/c)			$0.1 < p_T < 10^{10}$		$0.1 < p_T < 10^{10}$
$\eta$			$-0.9 < \eta < 0.9$		$-0.9 < \eta < 0.9$
$R_{xy}$ (cm)			$1 < R_{xy} < 90$		-
<b>Distinguishing cuts</b>					
Min cos PA	0.995	0.95	0.99	0.95	0.99
Max PCA	0.5	3.0	0.5	3.0	0.5
AP $\alpha, q_T$	-	0.95, 0.01	0.95, 0.01	0.95, 0.01	0.95, 0.01
WwireIB	-	-	-	-	true
WwireOB	-	-	-	-	true
$N_{\text{clusters ITS}}$	-	-	-	-	2 - 4
ITSTPC	-	-	true	-	-
TPConly	-	-	-	true	-

Table 4.1: Overview of the different cuts used in the analysis to select photons among all V0 candidates

with  $p_L^{e^+}$  the longitudinal momentum of the positron and  $p_L^{e^-}$  the one of the electron. The Armenteros-Podolanski plot [34] allows to separate photons from other V0 candidates. The electron-positron pairs from the photon conversion have a very small opening angle when they fly away from the conversion point. Therefore, the momentum of the daughter particles ( $e^+, e^-$ ) in transverse direction with respect to the mother particle  $q_T$  is close to zero. It is defined by

$$q_T = p_e \cdot \sin \theta_{V0,e}. \quad (4.3)$$

The cut that is done on the Armenteros-Podolanski plot is given by the two-dimensional cut

$$\left( \frac{\alpha_{V0}}{\alpha_{V0}^{max}} \right)^2 + \left( \frac{q_T}{q_T^{max}} \right)^2 < 1 \quad (4.4)$$

For the cuts that are applied,  $\alpha_{V0}^{max} = 0.95$  and  $q_T^{max} = 0.01$  are chosen. Furthermore, the V0 transverse momentum  $p_T$ , the pseudo-rapidity  $\eta$  and the radial position are limited to the values given also in table 4.1 A further constraint used is the pointing angle. It is a measure of how good the mother momentum points to the primary vertex and should be small i.e. the cosine of the pointing angle should be close to 1. Thus, a cut is used on  $\cos(\theta_{PA})$ . The value chosen depends on the different cuts and can be found in table 4.1. In addition, a line cut is applied on the V0s with respect to the geometry of the detector. This cuts out tracks that are outside of the fiducial zone. For the cut the following condition has to be fulfilled:

$$R_{conv} > |Z_{conv}| \cdot \tan(2 \cdot \arctan(\exp(-\eta_{max}))) - Z_0 \quad (4.5)$$

For this analysis,  $Z_0$  was set to 7 cm and  $R_{conv}$  and  $Z_{conv}$  are limited by previous cuts.

## 4.2 Data sets and Monte Carlo simulations

In the analyses performed for this thesis, several data sets of LHC Run 3 taken by ALICE in 2022 and 2023 are used. An overview of the different datasets used in the analysis is given in table 4.2. For the investigation of the material budget and the estimation of the calibration weights in chapter 5, the dataset LHC22f will be studied and is going to be compared with its anchored Monte Carlo LHC23d1k. An anchored Monte Carlo simulation anchored to a data set is produced with the same settings and detector conditions as the data. As LHC22f has a low interaction rate, this leads to less effects to calibrate. Therefore, it is well suited to study the material budget as the goal is to get a  $\gamma$ -ray tomography of the detector as detailed and precise as possible. For studying the photon momentum resolution in chapter 6, the datasets LHC22f, LHC22o minimum bias and LHC23zc as well as the Monte Carlo LHC23d1k anchored

Data sets used in the analysis						
Period	Run number	Pass	Date	Collision energy	Number of analysed events	Average IR/kHz
<b>Data</b>						
LHC22f	520259, 520294, 520471, 520472, 520473	pass 4	July 2022	13.6 TeV	75 263 460	42
LHC22o Min Bias <sup>1</sup>	526641, 526964, 527041, 527240	pass 4	July 2022	13.6 TeV	18 645 350 000	501.6
LHC23zc <sup>2</sup>	537901	apass 1	June 2023	13.6 TeV	1 160 703 000	673.6
LHC22 Low IR	LHC22f, m, q, r	pass 4	2022	13.6 TeV	4 127 947 000	42
<b>Monte Carlo</b>						
LHC23d1k	520259, 520294, 520471, 520472, 520473	pass 4		13.6 TeV	56 093 590	42

Table 4.2: Compilation of the different data sets and Monte Carlo simulation and their properties used in this thesis.

<sup>1</sup> Complete name: LHC22o\_pass4\_minBias\_medium<sup>2</sup> Complete name: LHC23zc\_pass1\_relval\_itstpcmap\_1 (Release Validation production in view of pp ref and PbPb 2023 data processing, ITSTPC map, updated tag)

to LHC22f are used. Doing so, the pion invariant mass fit can be compared first for data LHC22f and its anchored Monte Carlo LHC23d1k and then for the different datasets LHC22f, LHC22o min. bias and LHC23zc. The comparison of data and Monte Carlo allows to check whether the implementation in the simulation is right. The comparison of the different data sets allows to investigate the difference in the pion reconstruction that stems from having different properties of the data. In this analysis, the data sets will be compared having the following properties:

- LHC22f has a low interaction rate and therefore has fewer effects to be calibrated, fewer overlapping events
- LHC22o min. bias has an intermediate interaction rate. The term minimum bias describes events that have been selected with a minimum bias interaction trigger which is associated with inelastic collisions.
- LHC23zc has the best calibration currently available and a similar interaction rate to LHC22o min. bias

The comparison of the data sets allows to check the behaviour of the photon momentum resolution at different interaction rates, as well as calibration versions.

### 4.3 Analysis procedure

In this section, the details of the different steps of the analysis for the material budget as well as the photon momentum resolution will be explained. First, the tasks in the O2 analysis framework will be explained and then the contributions that were added during this thesis. The task in O2Physics/PWGEM can be found in the O2 repository <sup>3</sup>. A set of Python scripts was developed during this thesis to prepare the different plots, to calculate the calibration weights and to carry out the mass resolution studies. The scripts are uploaded on github <sup>4</sup>.

#### 4.3.1 Analysis of the material budget

For the study of the material budget, the result outputs created with the tasks listed in table 4.3 were the starting point.

---

<sup>3</sup>O2Physics PWGEM repository

<sup>4</sup>AlicePCMRun3 repository

Analysis Tasks Material Budget	
Monte Carlo LHC23d1k (HL155278)	Data LHC22f (HL125184)
o2-analysis-em-associate-mc-info	–
o2-analysis-em-material-budget-mc	o2-analysis-em-material-budget
o2-analysis-em-pcm-qc-mc	o2-analysis-em-pcm-qc
o2-analysis-em-create-pcm	
o2-analysis-em-skimmer-gamma-conversion	
o2-analysis-pid-tpc-base	
o2-analysis-pid-tpc-full	
o2-analysis-em-create-emreduced-event	

Table 4.3: Overview of the most important tasks used for the data used for the material budget in chapter 5. A complete overview can be found in the appendix A.1.1.

The first part of analysing the material budget was carried out using the ALICE O2Physics analysis framework. The data and Monte Carlo were processed using the tasks that are already implemented in O2Physics/PWGEM, see table 4.3.

While some of the tasks are helper tasks or required for the data analysis, the following tasks from the PWGEM carry out the analysis

- material-budget(-mc)
- pcm-qc(-mc)
- create-pcm

Note that (-mc) denotes the according tasks that are used for Monte Carlo. The task *create-pcm* functions as a new V0 finder <sup>5</sup> to reconstruct the V0 and the photon, respectively. Together with the task *pcm-qc* the output of the V0 finder along with the cuts that are applied on the reconstructed V0s (see overview in table 4.1), is stored in ROOT files.

The task *material-budget* loops over the identified V0 photons to study the material budget. The task includes more outputs, but in this analysis only the event and V0 outputs are used. The event output stores information that is used for the normalisation as the number of events and the number of charged particles. For the V0, a four-dimensional THnSparse histogram for each cut is stored with the dimensions  $p_T$ ,  $R_{xy}$ ,  $\eta$  and  $\varphi$ .

Starting with analysis of the raw data, one could investigate the material budget of the ITS2 and parts of the TPC in the dimensions of the radius  $R_{xy}$ , the azimuthal angle  $\varphi$  and the pseudo-rapidity  $\eta$ . To be able to get a detailed view on the different parts of the detector, radial cuts and cuts in the pseudo-rapidity were defined. The analysis

<sup>5</sup>It was developed to be able to use TPConly tracks, after first results from pilot beam data [35] showed that photons were only reconstructed until  $R_{xy} \leq 30$  cm

was performed for data and Monte Carlo. This led to the possibility to check the correct implementation of the detector material into the Monte Carlo simulation and to determine the position of material installed in the detector but not yet implemented into the simulation. The differences could be determined on the one hand by finding differences in the received output distributions and on the other hand by using the ratio of normalised reconstructed photons in data divided by those in Monte Carlo leading to a new distribution. As both distributions ideally should be identical, the deviation from 1 of the ratio could be used to quantify the differences. For the investigation of the material budget, Python scripts were developed to plot the following histograms:

- Integrated distributions in the four dimensions  $p_T$ ,  $R_{xy}$ ,  $\eta$  and  $\varphi$
- Two-dimensional distributions in  $R_{xy}$  vs  $Z$ ,  $R_{xy}$  vs.  $\varphi$  and  $V_x$  vs.  $V_y$

Furthermore, the material budget was investigated in different intervals in  $R_{xy}$  and  $\eta$ . To do so, the four-dimensional output of the *material-budget* task was cut along the intervals to then study the following distributions:

- The normalised number of photon conversions as a function of conversion point  $\eta$  for different radial intervals
- The normalised number of photon conversions as a function of  $\varphi$  for different intervals in conversion point  $R_{xy}$  and  $\eta$
- Two-dimensional distributions of  $\eta$  vs.  $\varphi$  of the conversion point for different radial intervals
- The normalised number of photon conversions as a function of  $p_T$  for different radial intervals

In addition, the code included the calculation of the Monte Carlo reconstruction efficiency. Python scripts were also developed for the estimation of the calibration weights following the two calibration methods established during Run 2. This allows the determination of the two calibration weights in the radial intervals chosen also for the investigation of the material budget while introducing a threshold in the photon transverse momentum  $p_T$ .

### 4.3.2 Analysis of the photon momentum resolution

The investigation of the photon momentum resolution was performed using the data sets LHC22f, LHC22o min. bias and LHC23zc as well as the Monte Carlo simulation LHC23d1k anchored to the data LHC22f. An overview of the tasks to analysis the raw data for the different data sets is given in table 4.4. Most of the tasks correspond to those of the analysis of the raw data for the study of the material budget. For the

Analysis Tasks photon momentum resolution			
Monte Carlo LHC23d1k (124837)	Data LHC22f (124838)	Data LHC22o min. bias (135860)	Data LHC23zc (134765)
o2-analysis-centrality-table	o2-analysis-centrality-table	o2-analysis-centrality-table	—
o2-analysis-multiplicity-table	o2-analysis-multiplicity-table	o2-analysis-multiplicity-table	o2-analysis-multiplicity-table
—	o2-analysis-cal-clusters	o2-analysis-cal-clusters	—
—	o2-analysis-je-enca-corr-task	o2-analysis-je-enca-corr-task	—
<b>o2-analysis-em-pcm-qc-mc</b>	<b>o2-analysis-em-pcm-qc</b>	<b>o2-analysis-em-pcm-qc</b>	<b>o2-analysis-em-pcm-qc</b>
o2-analysis-em-create-emreduced-mc-event	o2-analysis-em-create-emreduced-event	o2-analysis-em-create-emreduced-event	o2-analysis-em-create-emreduced-event
<b>o2-analysis-em-pi0eta-to-gammagamma</b>	<b>o2-analysis-em-pi0eta-to-gammagamma</b>	<b>o2-analysis-em-pi0eta-to-gammagamma</b>	<b>o2-analysis-em-pi0eta-to-gammagamma</b>
o2-analysis-em-skimmer-gamma-conversion	o2-analysis-em-skimmer-gamma-conversion	o2-analysis-em-skimmer-gamma-conversion	o2-analysis-em-skimmer-gamma-conversion
—	o2-analysis-em-skimmer-gamma-cal	o2-analysis-em-skimmer-gamma-cal	—
—	o2-analysis-em-skimmer-phos	o2-analysis-em-skimmer-phos	—
o2-analysis-em-skimmer-dalitz-ee	o2-analysis-em-skimmer-dalitz-ee	—	—
o2-analysis-track-propagation	o2-analysis-track-propagation	o2-analysis-track-propagation	o2-analysis-track-propagation
—	o2-analysis-trackselection	o2-analysis-trackselection	—
<b>o2-analysis-em-create-pcm</b>	<b>o2-analysis-em-create-pcm</b>	<b>o2-analysis-em-create-pcm</b>	<b>o2-analysis-em-create-pcm</b>

Table 4.4: Overview of the most important tasks used for the data and MC hyperloop train runs for the photon momentum resolution studies presented in chapter 6. Note that the the calibration and the software development are still ongoing, which is why different (helper) tasks are used for different data sets. A complete overview can be found in the appendix A.2.1.

analysis of the photon momentum resolution, the pion decay,

$$\pi^0 \rightarrow \gamma\gamma \tag{4.6}$$

is going to be used. Therefore, the most important step of the analysis of the raw data is the reconstruction of the pion using two photons. This is done in the *pi0eta-to-gammagamma*. This task allows the reconstruction of the neutral  $\pi^0$  and  $\eta$  meson. In this analysis, only the  $\pi^0$  will be investigated. The task combines photon pairs (every photon is paired with every other) and returns a histogram of  $M_{\gamma\gamma}$  vs.  $p_{T,\gamma\gamma}$ . This is done once for same-event photons and once for mixed-event photons. The latter allows to subtract the combinatorial background later in the analysis. The same- and mixed-event histograms are created for the cuts described in table 4.1.

With that output, the pion invariant mass is extracted from the  $\gamma\gamma$  invariant mass distribution to analyse the peak position and peak width for different data sets using Python scripts. First, the mixed-event histogram was scaled to the same-event one by using an integral over an interval outside of the region of the pion invariant mass and multiplying the mixed-event histogram by the value of the same-event integral divided by the mixed-event integral. Then, the pion invariant mass was fitted in different intervals in  $p_T$  using an asymmetric Gaussian and a polynomial for the remaining combinatorial background. From that the peak position was determined and the FWHM of the peak was calculated. In addition, a Python script to calculate the raw yield was written. All this was repeated for each interval in  $p_T$  and for each cut for the different data sets used in the analysis.

# 5 Material budget in the ITS2 and the TPC

For the reconstruction of charged particles especially during the tracking algorithm and for the determination of systematic uncertainties of many different measurements, a precise knowledge of the material budget of a given detector is crucial. It is needed for tracking, as the knowledge of the geometry and the material allows conclusions on where particles are most likely to be produced and how the material influences the trajectory of the particles. After the updates of the ALICE detector during LS2, the different parts of the detector changed and with that the material budget, too. Therefore, a renewal of the knowledge of the material budget is necessary. In addition, the new detector leads to mandatory updates in the implementation of its geometry in the Monte Carlo simulation. As the start of Run 3 is still recent, deviations in the implementation of the detector material occur. Therefore, it is important to get to know these and to communicate them.

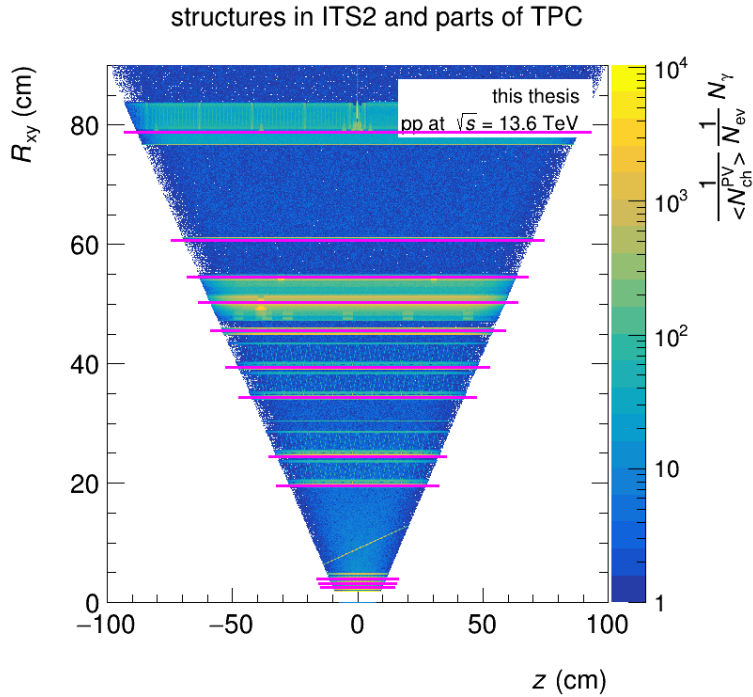


Figure 5.1:  $R_{xy}$  vs.  $V_z$  distribution of the photon conversion vertices calculated using the true MC coordinates. A  $\gamma$ -ray tomography of the detector material is obtained.

Probing the detector material is possible by using PCM, i.e. reconstructing electron positron pairs that originate from a photon conversion. By reconstructing converted photons, one can obtain a detailed  $\gamma$ -ray tomography of the detector. The analysis of Monte Carlo simulations allows to investigate the detector geometry implemented in the software. First, one uses the information provided by Geant to identify all  $\gamma$  conversions and their true spatial coordinates  $(V_x, V_y, V_z)$ .

In figure 5.1, the conversion radius  $R_{xy} = \sqrt{V_x^2 + V_y^2}$  is given as a function of  $V_z$ . One can see the different structures that form the inner part of the ALICE detector, namely the different layers of the ITS and its components and the inner part of the TPC.

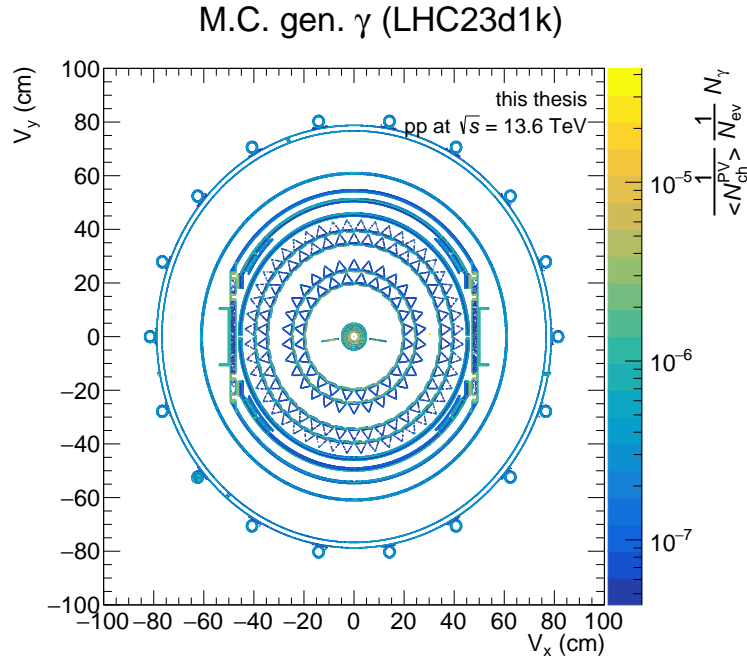


Figure 5.2:  $V_y$  vs  $V_x$  distribution of converted photons in the detector material using the true MC coordinates. The different detector components are clearly visible.

These structures are also visible in figure 5.2. Here, the photon conversion points are plotted in a  $V_y$  vs  $V_x$  distribution. In the centre of the plot, the IB of the ITS is visible as well as the two installed calibration wires. In addition, one can see the middle and outer layers of the OB. The triangular shape of the OB staves is also visible [18]. The corresponding  $V_y$  vs  $V_x$  distributions as obtained in reconstruction of real data for the LHC22f period and its anchored Monte Carlo LHC23d1k can be seen in figure 5.3. The different detector structures are also visible but convoluted with the experimental resolution.

As a first step of the analysis, a detailed study on the material budget of the inner

part of the ALICE detector was performed. This was done in radial direction up to a radius of 90 cm. This includes the complete ITS2 as well as a fraction of the TPC. As data sets, LHC22f and its anchored Monte Carlo LHC23d1k are used. Their properties are given in table 4.2. To be able to compare the number of reconstructed photons for data and Monte Carlo, the numbers are normalised by the respective number of events  $N_{ev}$  and the average number of reconstructed charged particles  $\langle N_{ch} \rangle$ . The factor  $\langle N_{ch} \rangle$  takes into account that the number of produced photons can be different in MC simulations and in data.

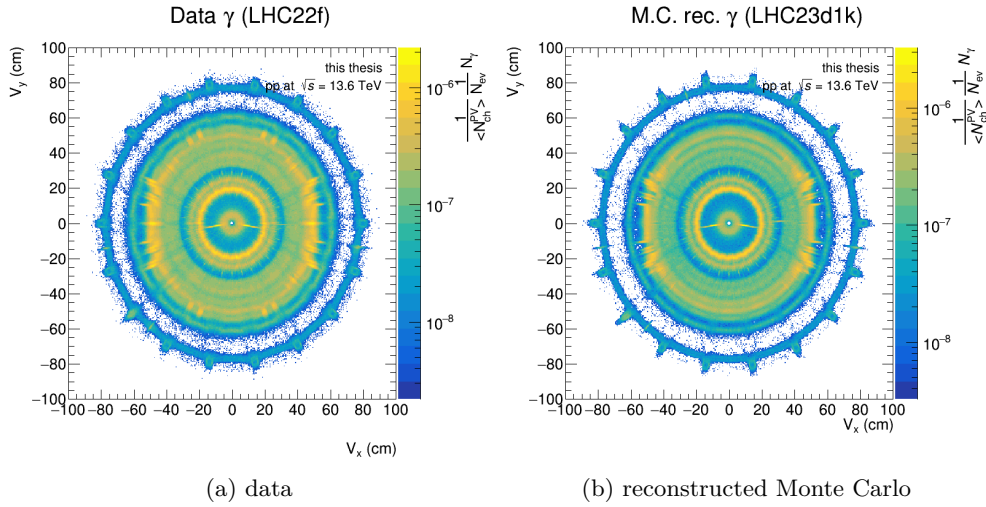


Figure 5.3:  $V_x$  vs  $V_y$  distribution of reconstructed photons in the detector material for data and Monte Carlo

After the study of the material budget in different radial intervals, an overview of the calculation of calibration weights for the material budget will be given. Two methods will be applied on data of Run 3 that have been developed in Run 2. However this will only be a first estimate as the effort of a complete calculation is beyond the scope of a Bachelor's thesis.

## 5.1 Detailed comparison of data and anchored Monte Carlo

At this stage, the one dimensional distributions of the normalised number of converted photons for data and Monte Carlo can be looked at <sup>1</sup>. This is first done in the azimuthal angle  $\varphi$  resulting in a distribution from 0 to  $2\pi$  covering all  $R$  and  $\eta$ . This distribution

<sup>1</sup>For all Monte Carlo distributions, validated primary photons are selected. The impact of the purity of the photon sample will be discussed in section 5.4

is seen in figure 5.4. In this figure, like in this complete chapter, data is represented by blue and Monte Carlo by red markers. In the upper part of each plot, the distribution of reconstructed photons as a function of the respective coordinates for data and Monte Carlo is given. In the lower part, the ratio of data divided by Monte Carlo is plotted. To have matching data sets, one would aim for deviations of maximum five percent (marked by the dashed lines). As one can see, the overall shape of data and Monte Carlo seems comparable. However, one can also see that there are different peaks visible in data but not in Monte Carlo and vice-versa. To investigate these deviations further, one can look at the other dimensions  $R_{xy}$  and  $\eta$ . The results can be seen in figure 5.5. Looking at the distribution of converted photons as a function of  $R_{xy}$ , one can see distinguishable minima at different radii. The different regions correspond to different detector structures named in figure 5.1. The ratio as a measure for the deviation between data and Monte Carlo shows deviations of up to 90 % for  $69 \text{ cm} \leq R_{xy} \leq 90 \text{ cm}$  and of up to 10% for positive  $\eta$ . For a better understand of these differences, the purity of the photon sample was investigated in Monte Carlo. See section 5.4 for more details.

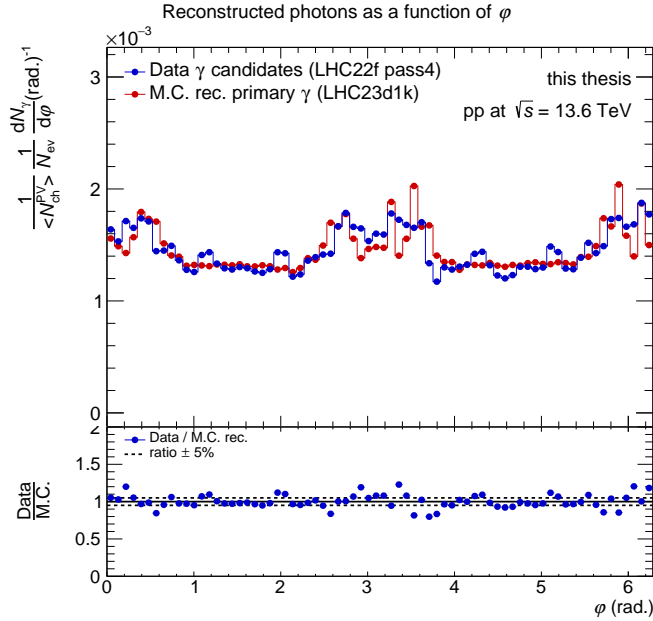


Figure 5.4: Top: Integrated plot of the normalised number of reconstructed photons as a function of  $\phi$  for the data set LHC22f in blue and its corresponding Monte Carlo LHC23d1k in red

Bottom: Ratio of the data and Monte Carlo distributions from the top. The five percent deviation is marked by two dashed black lines.

In order to take a detailed look on the deviations between data and MC, various cuts in the dimensions  $R_{xy}$  and  $\eta$  are defined. Those are shown in figure 5.5 with the pink lines and hatched areas respectively. The cuts in  $\eta$  are chosen to match the typical

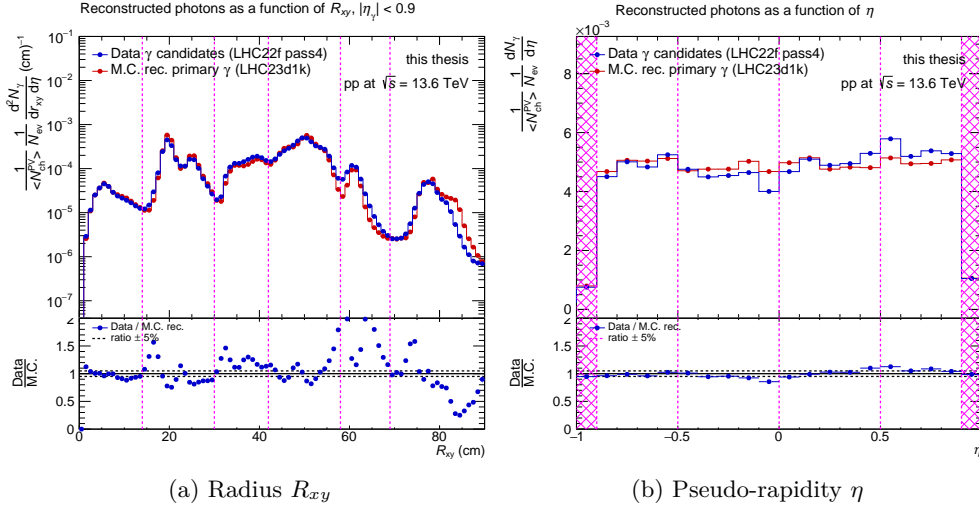


Figure 5.5: Top: Integrated plots of the number of reconstructed photons in the dimensions  $R_{xy}$  (a) and  $\eta$  (b) for the data set LHC22f in blue and its corresponding Monte Carlo LHC23d1k in red. The selected cuts are illustrated with pink lines. Bottom: Ratio of the data and Monte Carlo distributions from the top. The five percent deviation is marked by two dashed black lines.

pseudo-rapidity range of  $|\eta| \leq 0.9$ . This corresponds to the pseudo-rapidity coverage for full radial track length of the TPC as well as the ITS [20, 36].

This is further divided in positive and negative pseudo-rapidity as well as smaller and larger absolute values corresponding to a cut at  $|\eta| = 0.5$ . That makes a total of six cuts in  $\eta$  resulting in four intervals plus two additional intervals including the division in positive and negative  $\eta$  for an absolute value of  $|\eta| \leq 0.9$ . The defined cuts in  $\eta$  are listed in table 5.1. In radial direction the cuts were chosen to match the minima visible

detector side	pseudo-rapidity interval	subdivided pseudo-rapidity interval
C side	$-0.9 \leq \eta \leq 0.0$	$-0.9 \leq \eta \leq -0.5$
		$-0.5 \leq \eta \leq 0.0$
A side	$0.0 \leq \eta \leq 0.9$	$0.0 \leq \eta \leq 0.5$
		$0.5 \leq \eta \leq 0.9$

Table 5.1: Overview of the cuts in  $\eta$ . Note that all six intervals listed in this table are investigated.

in figure 5.5 (left). Those correspond to the different parts of the ITS and TPC as seen in table 5.2. Note that they first were chosen according to the data sets but they also match the Technical Design Report of the ITS, see table 2.1. The complete division is given in table 5.3: Here, for each combination of radial and pseudo-rapidity cut, the

Radial interval	Contained structures/detector parts
$0 \text{ cm} \leq R_{xy} \leq 14 \text{ cm}$	The three layers of the Inner Barrel of the ITS and two of the in total three tungsten wires installed for calibration purposes
$14 \text{ cm} \leq R_{xy} \leq 30 \text{ cm}$	The two Middles Layers of the Outer Barrel of the ITS
$30 \text{ cm} \leq R_{xy} \leq 42 \text{ cm}$	The two Outer Layers of the Outer Barrel of the ITS
$42 \text{ cm} \leq R_{xy} \leq 58 \text{ cm}$	Support structure for the ITS2
$58 \text{ cm} \leq R_{xy} \leq 69 \text{ cm}$	Inner containment vessel of the TPC consisting of the central drum surrounding the ITS with a radius of 610mm and two support cones
$69 \text{ cm} \leq R_{xy} \leq 90 \text{ cm}$	Inner field cage vessel of the TPC with a radius of 788 mm

Table 5.2: Overview of the cuts in  $R_{xy}$  and the structures or detector parts they contain.

normalised number of reconstructed photons is plotted as a function of the angle  $\varphi$  for data and Monte Carlo. In addition, the ratio of normalised number of reconstructed photons for data divided by the same quantity for Monte Carlo is given.

It can be noticed, that for small radius and all pseudo-rapidity ranges, data and Monte Carlo show comparably little deviation (with exception of the  $\varphi$  regions corresponding to the calibration wires). Looking at a radius of  $14 \text{ cm} \leq R_{xy} \leq 30 \text{ cm}$ , the ratio between data and Monte Carlo comes close to five percent. For the experiment, even smaller deviations are required, but this is already a promising result.

However, the ratio plotted in the different histograms in table 5.3, spreads over a broad range: Especially for larger radii such as  $69 \text{ cm} \leq R_{xy} \leq 90 \text{ cm}$ , the deviation between data and Monte Carlo increases up to a level of 60 %. This indicates that the reconstruction still needs to be improved as this was not observed in Run 2 and the material in this radial interval is the same as before LS2 [22]. Looking at radii between 69 and 90cm, the difference between data and MC can only be explained by differences in the efficiency as the material did not change between Run 2 and Run 3.

Like it was already visible in figure 5.5 (right), the number of reconstructed photons as a function of the pseudo-rapidity shows differences between positive and negative  $\eta$ . This is also visible in table 5.3 for example at a radius of  $58 \text{ cm} \leq R_{xy} \leq 69 \text{ cm}$ : Here, the deviation for positive  $\eta$  is smaller than for negative pseudo-rapidity. Looking at a pseudo-rapidity range of  $0.5 \leq |\eta| \leq 0.9$ , the deviation between data and Monte Carlo is at a level of 20 % for positive compared to around 50% for negative  $\eta$ .

As a general trend, it is observed, that with increasing radius  $R_{xy}$  and increasing absolute pseudo-rapidity  $\eta$ , the deviation between data and Monte Carlo becomes larger.

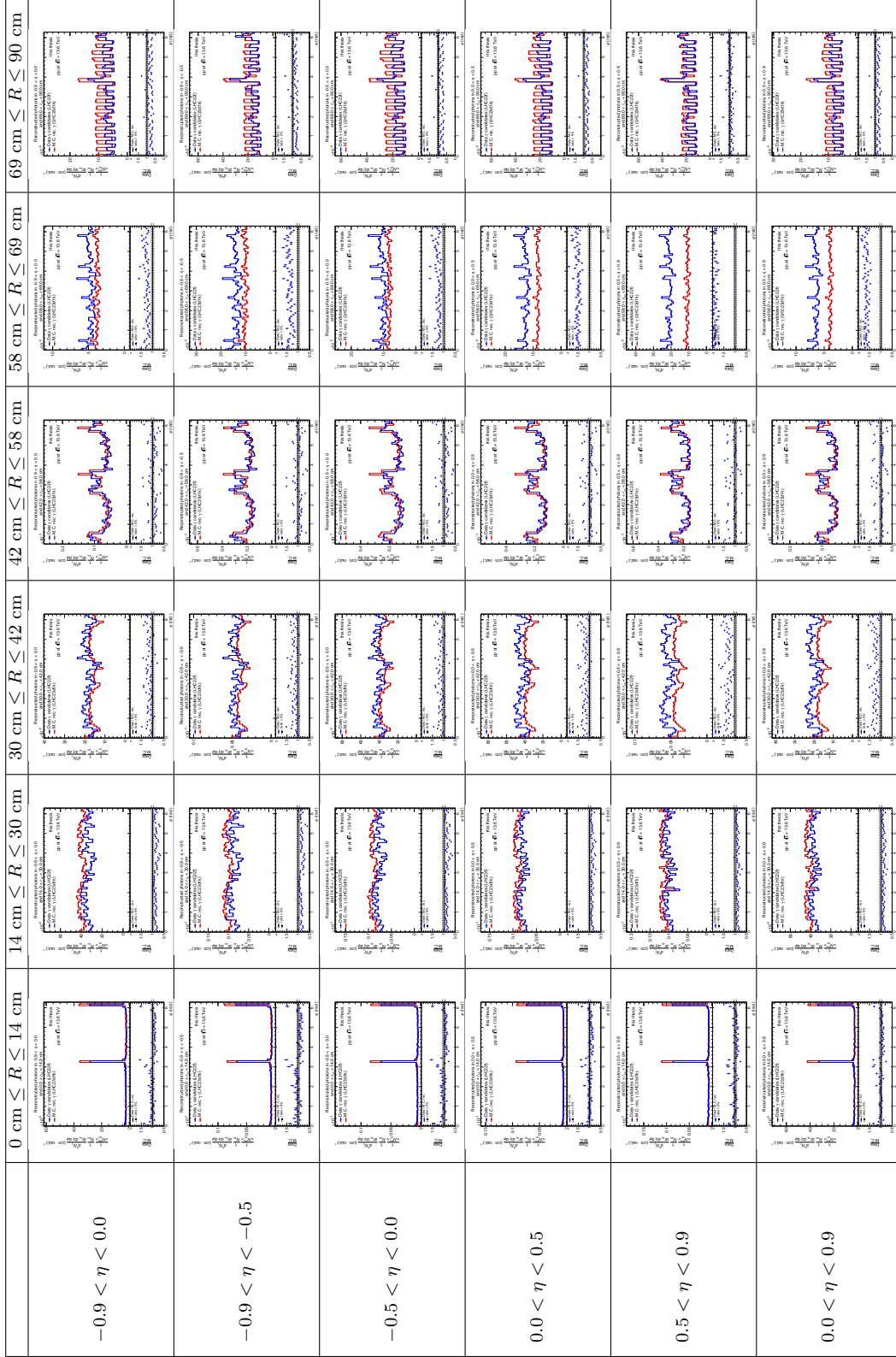


Table 5.3: Overview of the different plots that result from the cuts defined in tables 5.1 and 5.2

## 5.2 Comparison in $\varphi$ and $\eta$ in the radial interval of $42 \text{ cm} \leq R_{xy} \leq 58 \text{ cm}$

In this section, a detailed comparison between data and Monte Carlo will be given. The focus will be set on the radial interval of  $42\text{cm} \leq R_{xy} \leq 58 \text{ cm}$ . In the appendix A.2, conclusions for the other radial intervals that have been defined in table 5.2 will be given. In a first step, the one dimensional distribution of the normalised number

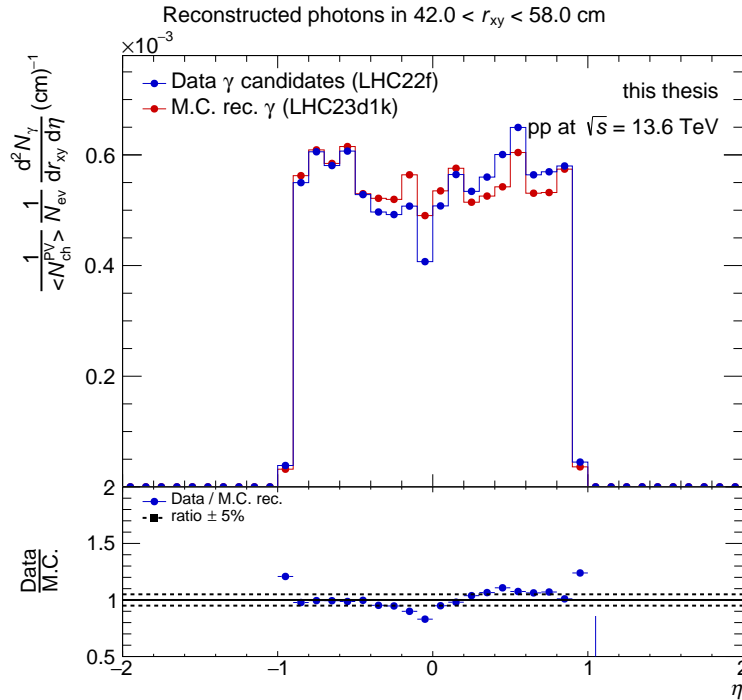


Figure 5.6: Distribution of the normalised number of reconstructed photons as a function of  $\eta$  in a radial interval of  $42 \text{ cm} \leq R_{xy} \leq 58 \text{ cm}$

of reconstructed photons as a function of  $\eta$  for the chosen radial interval can be investigated in figure 5.6. As one can see in the direct data and Monte Carlo comparison in the upper part of the plot as well as in the lower part showing the ratio between data and Monte Carlo, the Monte Carlo is below data in positive  $\eta$ . This results in local deviations of up to 20%. This effect is also visible for negative  $\eta$ , however the deviation is almost completely in the five percent range. In addition it is visible, that both distributions are not symmetric in  $\eta$  but the Monte Carlo distribution is even more asymmetric which can explain the increasing deviation. Looking at table 2.2, one can see that in the investigated radial interval, multiple structural components of the ITS2 are located. This could give a reason for the deviation. However, the reason is

not yet clarified. In the future, once the calibration has converged and the calibration procedure is fully established, one may need to check this deviation again.

Similar  $\eta$ -distributions for the other radial intervals are given in the appendix in table A.1. There, one can see that the deviation between data and Monte Carlo increases with increasing radius and the distributions deviate more between positive and negative  $\eta$  resulting in more and more asymmetry. In a next step, this found deviation can

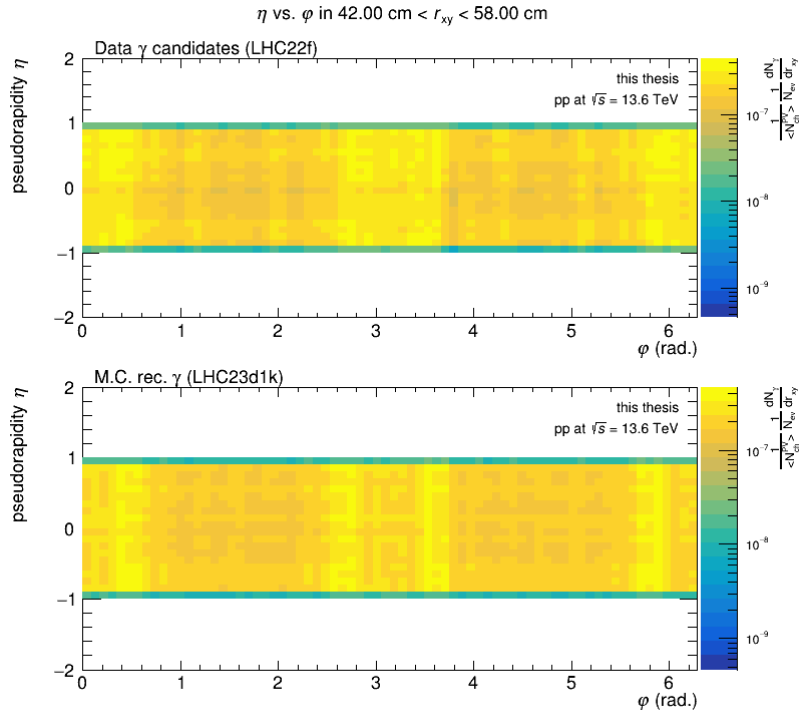


Figure 5.7: Two-dimensional plot in  $\eta$  vs.  $\varphi$  of the normalised number of reconstructed photons in a radial interval of  $42\text{cm} \leq R_{xy} \leq 58\text{cm}$

be studied in more detail by looking at the two dimensional distribution of  $\eta$  vs. angle  $\varphi$ . This is shown in figure 5.7 for data on top and for Monte Carlo on the bottom. The overall shape of the two plots seems comparable. However on one hand, an additional structure in data and  $\eta \approx 0$  is visible, that is not represented in Monte Carlo. On the other hand, there seems to be an additional structure at  $\varphi \approx \pi$  and  $\varphi \approx 2\pi$  in Monte Carlo that is not visible in data.

To get an even more detailed view on the deviations between data and Monte Carlo, both cuts in  $R_{xy}$  and  $\eta$  can be performed at the same time, this results in the overview given in table 5.4. Here, the result of the six cuts in  $\eta$  defined in table 5.1 is shown: The

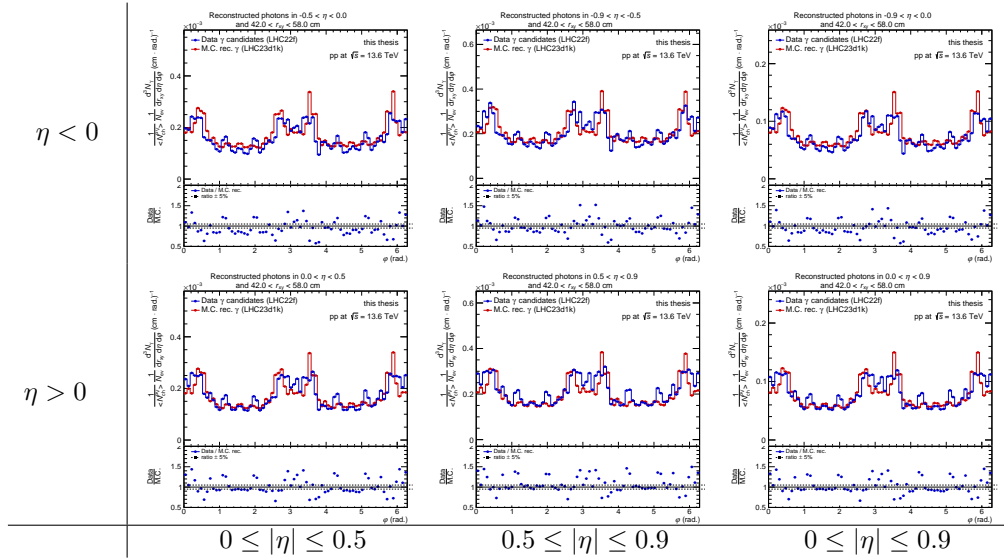


Table 5.4: Distribution of reconstructed photons as a function of  $\varphi$  in different intervals of  $\eta$  for  $42\text{cm} \leq R_{xy} \leq 58\text{ cm}$

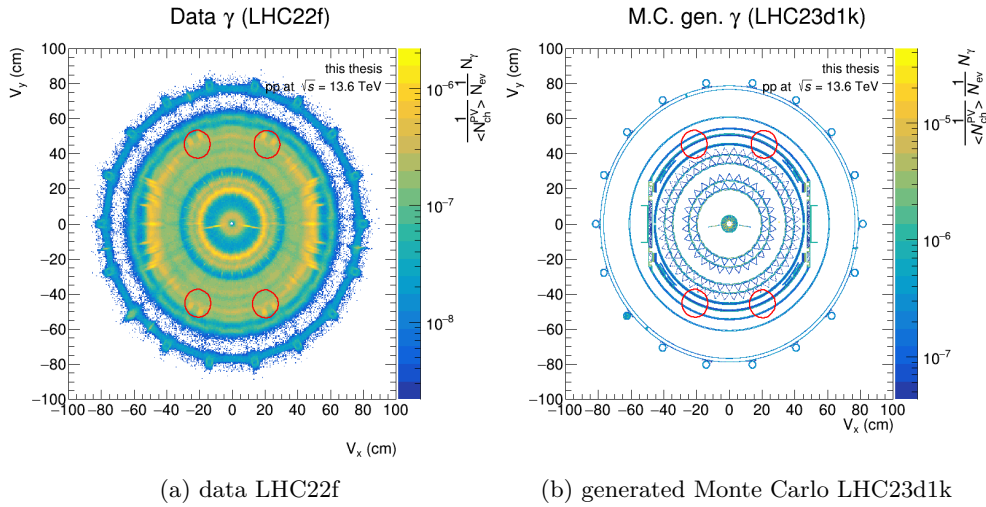
plots for negative pseudo-rapidity are given on the top and for positive pseudo-rapidity on the bottom, respectively. From left to right, the plots are divided in different absolute values of  $\eta$ . This results in  $2 \times 3$  plots.

Note that in the appendix A.1, overviews with the same structure are given for each radial interval. For the radial interval considered in this section, one can see that in each plot, three respectively two, considering the cylindrical shape of the detector, global maxima are prominent at an angle of around  $\varphi \approx \pi$  and  $\varphi \approx 2\pi$ . For data, they have a broader shape than in Monte Carlo where those maxima are more divided into two separate maxima each.

In addition to this overall shape of the distribution in  $\varphi$ , a substructure in data is visible that is not represented in Monte Carlo: between the global maxima, there are two regions of a lower level. Additionally, in data there each are two well distinguishable and two less visible peaks. It seems there is additional detector structure that is not yet or not yet correctly implemented in Monte Carlo. To find out which structure this could be, the position of these peaks is determined. The values are given in table 5.5.

The calculated angular positions of the peaks for positive and negative pseudo-rapidity are matching. An overview of the calculated angular positions for all cuts in  $\eta$  is given in the appendix A.9. To find out which structure the peaks represent, the positions can be located in two-dimensional plots of the  $R_{xy}$ -plane for generated Monte Carlo and data. Looking at figure 5.8, one can see a structure in data, that is not implemented in Monte Carlo. Discussion with experts lead to the conclusion, that the missing structure are the Muon Forward Tracker (MFT) rails on the cage [21]. The cage is a support

detector part	$-0.9 \leq \eta \leq 0.0$	$0.0 \leq \eta \leq 0.9$
upper half	1.13	1.13
	2.01	2.01
lower half	4.28	4.28
	5.15	5.15

 Table 5.5: Angular position  $\varphi$ [rad] of the well visible peaks for positive and negative  $\eta$ 

 Figure 5.8: Two-dimensional plots in the  $R_{xy}$ -plane of the normalised number of reconstructed photons. The red circles represent the angular position of the peaks found in a radial interval of  $42\text{cm} \leq R_{xy} \leq 58\text{cm}$ 

structure, that holds the beam pipe, the ITS2 and the MFT [12]. The implementation of the MFT rails is currently (January 2024) still ongoing. With all these statements, it is important to mention that discrepancies between data and Monte Carlo can also occur due to bin migration. This can happen as the bins/cuts in  $R_{xy}$  defined here could lead to some smearing in  $R_{xy}$  which would then lead to shifting of structures originating from one defined interval to another. This effect cannot be excluded in this analysis.

In conclusion, studying the deviation between data and Monte Carlo in detail is of interest as this can give information on the current implementation of the detector material into the Monte Carlo simulation. As ALICE has undergone a major upgrade during LS2, this is particularly important because the composition and position of the different detector parts has changed and also the analysis framework which contains the model of the detector used for Monte Carlo production was updated.

### 5.3 Reconstruction efficiency

A further step in the analysis is to calculate the reconstruction efficiency which gives a measure on how good the reconstruction is working. As one knows the actual conversion points from generated Monte Carlo, this is used as the true information. To be able to calculate the efficiency as a function of  $R_{xy}$  without the effect of the resolution, histograms of reconstructed conversion points using the true conversion point (green distribution) were implemented. The efficiency can then be calculated by dividing the reconstructed Monte Carlo distribution with Monte Carlo truth conversion points by the generated Monte Carlo distribution. This is displayed in figure 5.9.

One can see, that the efficiency is mostly at a level of 10% and has a tendency to decrease with increasing radius. In addition, for very small radii smaller than 5 cm the reconstruction efficiency drops significantly.

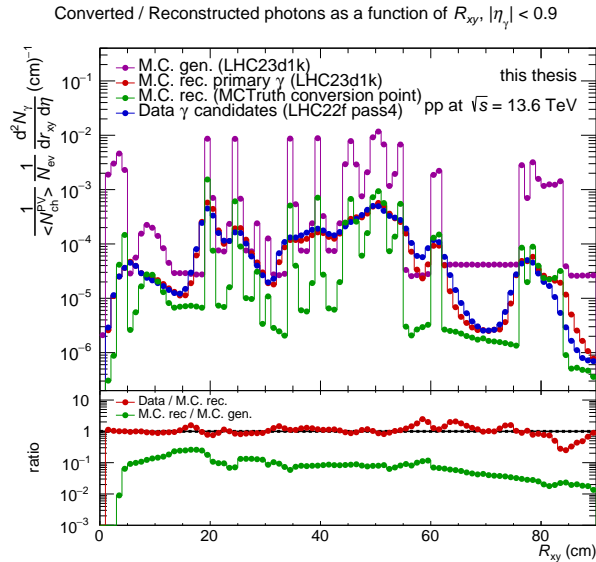


Figure 5.9: Top: Integrated plots of the normalised number of reconstructed photons as a function of  $R_{xy}$  for data LHC22f in blue, as well as for generated MC in violet, reconstructed MC primary photons in red, and reconstructed MC using the MCTruth conversion point in green. All Monte Carlo distributions stem from the period LHC23d1k.

Bottom: Ratio of data and reconstructed Monte Carlo primary in red and ratio of reconstructed Monte Carlo using the true conversion point in green.

## 5.4 Purity of the photon sample

To examine the purity of the photon sample, one can compare the reconstruction of Monte Carlo and data by reconstructing the Monte Carlo once actually like Monte Carlo and once like data. The radial distributions of the normalised number of reconstructed photons is displayed in figure 5.10. One can see that the reconstruction as data overall leads to more reconstructed photons as the reconstruction of primary photons. General differences occur, as the reconstructed Monte Carlo in the analysis only uses primary photons. For data, contamination can occur for example because of  $K$ ,  $\Lambda$  etc. as well as combinatorics. This effect can also be seen in Monte Carlo when it is reconstructed like data, i.e. not only primary photons are reconstructed but rather photon candidates.

The ratio varies from 1.05 to 1.2 up to  $R_{xy} \approx 55$  cm and for  $55 \text{ cm} \lesssim R_{xy} \lesssim 75$  cm a large deviation is observed. This could be one explanation for the increasing differences of data and Monte Carlo with increasing radius in the analysis before (see table 5.3).

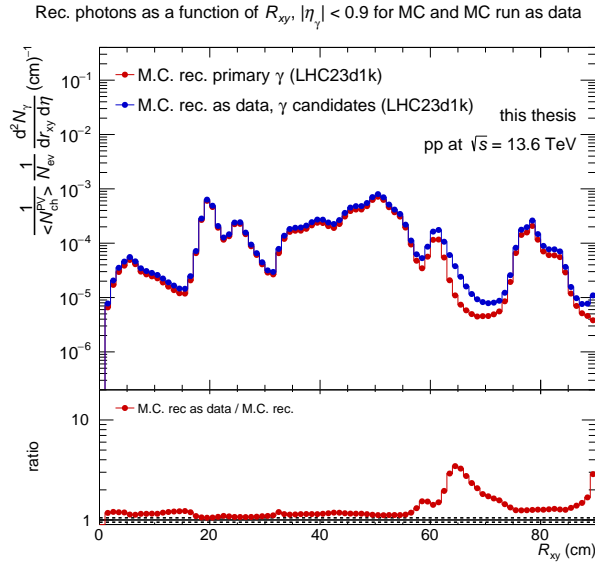


Figure 5.10: Purity of the photon sample.

Top: Integrated plots of the normalised number of reconstructed photons as a function of  $R_{xy}$  for reconstructed MC primary photons in red and reconstructed MC ran as data in blue. Both Monte Carlo distributions stem from the period LHC23d1k.

Bottom: Ratio of the distribution of Monte Carlo reconstructed as data divided by reconstructed Monte Carlo primary photons.

## 5.5 Transverse momentum spectra

The comparison of the normalised transverse momentum distributions in data and Monte Carlo brings additional information to understand possible differences between data and Monte Carlo. In figure 5.11, the comparison is displayed in each radial interval and in addition for the calibration wires installed in the ITS2.

The calibration wires, that are installed in the inner part of the ITS2 and the first radial interval of  $0 \text{ cm} \leq R_{xy} \leq 14 \text{ cm}$  have a similar  $p_T$  distribution. Their spectra decrease more rapidly with  $p_T$  than the spectra for larger intervals. Their similar shape can be explained by their common radial position. The other radial intervals have an overall homogeneous shape and the highest number of reconstructed photons is reached for a radial interval of  $42 \text{ cm} \leq R_{xy} \leq 58 \text{ cm}$ .

Especially for the ratios, the deviations increase with increasing  $p_T$  and for two intervals ( $30 \text{ cm} \leq R_{xy} \leq 42 \text{ cm}$ ) and ( $58 \text{ cm} \leq R_{xy} \leq 69 \text{ cm}$ ) the deviations at low  $p_T$  are also sizable.

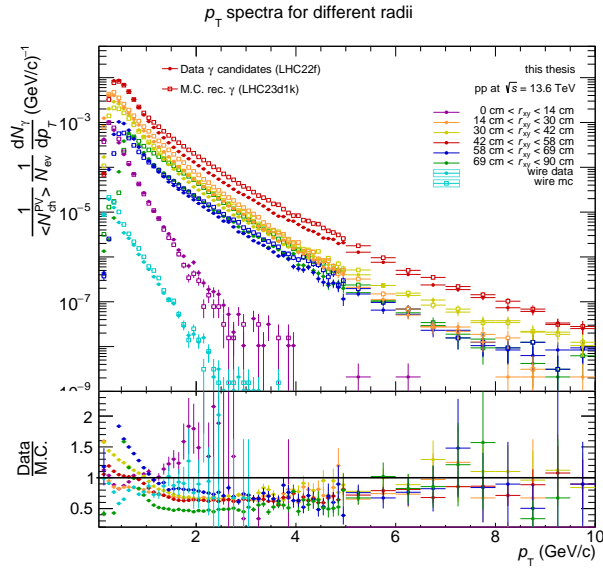


Figure 5.11: Top: Transverse momentum spectra for data (bold markers) and reconstructed MC (empty markers) in the different radial intervals that have been defined in table 5.2 as well as for the calibration wires installed in the ITS2. Bottom: Ratio of Data and MC for the different radial intervals and the calibration wires

## 5.6 Calibration of the material budget

As seen in chapter 5, differences between data and Monte Carlo in the normalised number of reconstructed photon conversions occur. Ideally, this should only be the case if the number of reconstructed photons is not normalised. But if the number of reconstructed is normalised by  $\langle N_{ch} \rangle$ , there should be no more differences. However, a high precision of the knowledge of the material budget is crucial for example for the reconstruction of charged particles as well as for the reconstruction of photons using PCM. Therefore, a data-driven correction to the material budget description can be applied. The methods used in this section were developed in Run 2 [1, 37]. The goal of these methods is to reduce the systematic uncertainty for photon measurements and for analyses based on tracking of charged particles as well as to reduce local differences in the detector material description in Monte Carlo.

In Run 2, pion-isospin-symmetry based calibration weights  $\Omega_i$  and TPC-gas based calibration weights  $\omega_i$  have been developed. In this thesis using data from Run 3, pion-isospin-symmetry based calibration weights will be calculated as well. Replacing the use of TPC-gas for calibration purposes, calibrated tungsten wires were inserted in the IB and OB of the ITS2. As their composition and position is well known, these can be used to assist the material budget calibration and to estimate the  $\omega_i$  weights.

In this thesis, only a first calculation of the calibration weights will be given. Like in Run 2 [1], this would be followed by an iterative process of applying weights to the Monte Carlo data and from that calculating new calibration weights with the aim to get the evaluation procedure of the calibration weights to converge. This process is done as the difference in the number of reconstructed photons could also stem from a different shape of the  $p_T$  spectrum in Monte Carlo compared to data. In addition, secondary charged particles would need to be subtracted and systematic uncertainties to be calculated. As this is a quite complex and time consuming process, this is not done here but could be a topic of future analyses.

### 5.6.1 Pion-isospin-symmetry based calibration weights $\Omega_i$

To correct the material budget, one can use the robustness of the ratio of number of reconstructed photons to the number of reconstructed charged particles ( $N_\gamma^{\text{rec}}/N_{\text{ch}}^{\text{rec}}$ ) [1]. First, this is the case because of the approximate isospin symmetry in the number of produced charged and neutral pions. The pions have an Isospin of  $I = 1$  and the third component of the isospin is  $-1, 0, 1$  for  $\pi^-, \pi^0$  and  $\pi^+$ , respectively. Thus, they form an isospin triplet. Because of isospin symmetry, the number of the different kinds of pions produced in collisions is the same as the particle production in the collisions does not favour any isospin state.

Second, charged pions are the main contribution to the number of charged particles

(90% of charged particles are charged pions) [38, 1] and the photons from  $\pi^0$  decays are the dominant contribution to the total number of photons. This has been verified with Monte Carlo using different event generators.

The ratio  $N_{\gamma,i}^{\text{rec}}/N_{\text{ch}}^{\text{rec}}$  can be calculated in different radial intervals  $i$ . For completeness,

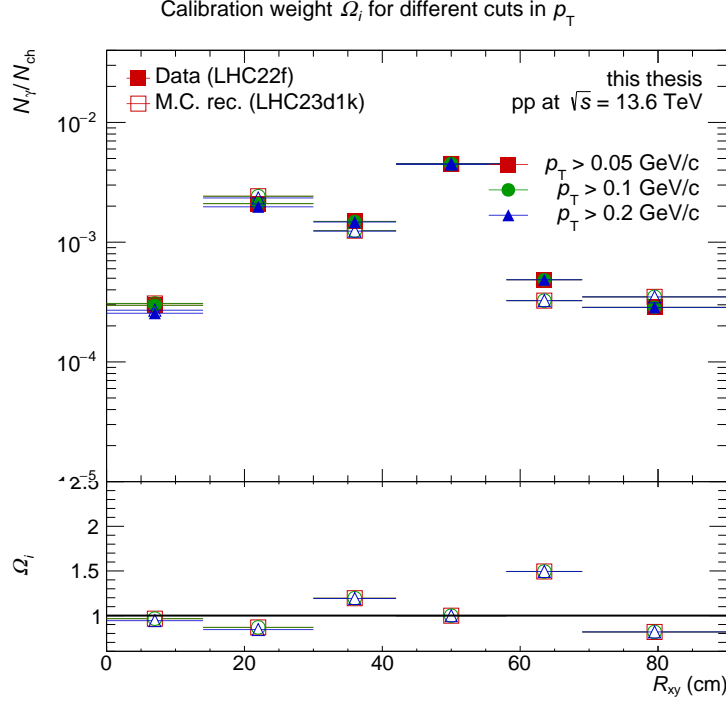


Figure 5.12: Calculated ratios  $N_{\gamma,i}^{\text{rec}}/N_{\text{ch}}^{\text{rec}}$  (top) and derived calibration weights  $\Omega_i$  for data LHC22f and Monte Carlo LHC23d1k

the same intervals as for the material budget investigation in chapter 5 are used. In addition this can be done for data and Monte Carlo. Next, the ratio of those two calculated ratios can be determined which is then defined as the pion-isospin-symmetry based calibration weight given by

$$\Omega_i = \frac{N_{\gamma,i}^{\text{rec, RD}}/N_{\text{ch}}^{\text{rec, RD}}}{N_{\gamma,i}^{\text{rec, MC}}/N_{\text{ch}}^{\text{rec, MC}}} \quad (5.1)$$

with  $N_{\text{ch}}^{\text{rec, RD}}$ ,  $N_{\text{ch}}^{\text{rec, MC}}$  the number of reconstructed primary tracks with a transverse momentum above a chosen threshold. RD and MC stand for real data and Monte Carlo, respectively. This quantity is then sensitive to the correctness of the detector material implementation: Assuming the photon reconstruction efficiency obtained in MC simulations is the same as in real data and the detector material implementation to be completely correct, one would get a ratio of 1 as the detector material would

lead to the same number of photon conversions. The estimated values of  $\Omega_i$  are shown in figure 5.12. The different thresholds applied in  $p_T$  only show a small influence on the ratio  $N_\gamma/N_{\text{ch}}$  and thus on  $\Omega_i$ . The difference also decreases even further with increasing radial interval. The calibration weights have values of around 0.8 to around 1.5. In general, the deviation of the expectation value increases with increasing radius. This is in accordance with the increasing deviation between data and Monte Carlo for increasing radii which was also observed in the studies of the material budget. Especially the calibration weight determined for the radial interval of 58 to 69 cm deviates from the expectation value. Looking at the purity of the photon sample depicted in figure 5.10, one can see also a large deviation between reconstructed Monte Carlo and reconstructed Monte Carlo run as data. This can also explain the large deviation for the calibration weight determined in this region.

### 5.6.2 Tungsten-wire based calibration weights $\omega_i$

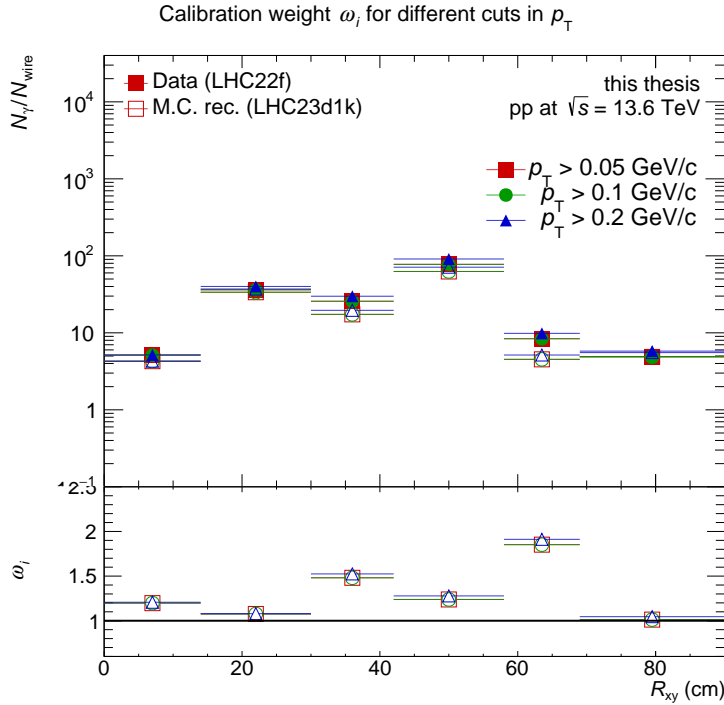


Figure 5.13: Calculated ratios  $N_{\gamma,i}^{\text{rec}}/N_{\gamma,\text{wire}}^{\text{rec}}$  (top) and derived calibration weights  $\omega_i$  for data LHC22f and Monte Carlo LHC23d1k

The calibrated tungsten wires installed in the IB and OB of the ITS2 can be used as a reference as their position and composition is very well known <sup>2</sup>. With that, the rest

<sup>2</sup>In this analysis, only the tungsten wires installed in the IB of the ITS2 are used.

of the detector can be calibrated. The tungsten-wire calibration weight is given by

$$\omega_i = \frac{N_{\gamma,i}^{\text{rec, RD}} / N_{\gamma,\text{wire}}^{\text{rec, RD}}}{N_{\gamma,i}^{\text{rec, MC}} / N_{\gamma,\text{wire}}^{\text{rec, MC}}} \quad (5.2)$$

with  $N_{\gamma,\text{wire}}^{\text{rec, RD}}$ ,  $N_{\gamma,\text{wire}}^{\text{rec, MC}}$  the number of reconstructed photons whose conversion point corresponds to the wire and  $N_{\gamma,i}^{\text{rec, RD}}$ ,  $N_{\gamma,i}^{\text{rec, MC}}$  the number of reconstructed photons for real data (RD) or Monte Carlo (MC) in the respective radial interval  $i$ . For all the calculated numbers of reconstructed photons, a threshold in  $p_T$  is applied. The estimated  $\omega_i$  values as a function of the radial position are displayed in figure 5.13. Compared to figure 5.12, the ratios  $N_{\gamma}/N_{\text{wire}}$  show more deviation for the different thresholds in  $p_T$  which thus also follows for the calibration weights  $\omega_i$ . The weights calculated for the different radial intervals follow a similar shape as the pion-isospin based weights but are overall higher ranging from around 1.0 to around 1.8.

### 5.6.3 Comparison of the calibration weights $\Omega_i$ and $\omega_i$

One can compare the calibration weights using equations (4.11) and (4.12) in the paper [1] given by

$$\frac{\Omega_i}{\omega_i} = \frac{P_{\text{wire}}^{\text{RD}} \times \varepsilon_{\gamma,\text{wire}}^{\text{RD}} \times \varepsilon_{\text{track}}^{\text{MC}}}{P_{\text{wire}}^{\text{MC}} \times \varepsilon_{\gamma,\text{wire}}^{\text{MC}} \times \varepsilon_{\text{track}}^{\text{RD}}} \quad (5.3)$$

and

$$\frac{\Omega_i}{\omega_i} = \frac{\varepsilon_{\gamma,\text{wire}}^{\text{RD}} \times \varepsilon_{\text{track}}^{\text{MC}}}{\varepsilon_{\gamma,\text{wire}}^{\text{MC}} \times \varepsilon_{\text{track}}^{\text{RD}}} \quad (5.4)$$

with the conversion probabilities  $P_{\text{wire}}^{\text{RD}}$ ,  $P_{\text{wire}}^{\text{MC}}$  that can be assumed equal and the photon reconstruction efficiencies  $\varepsilon_{\gamma,\text{wire}}^{\text{RD}}$ ,  $\varepsilon_{\gamma,\text{wire}}^{\text{MC}}$  and the detection efficiencies  $\varepsilon_{\text{track}}^{\text{RD}}$ ,  $\varepsilon_{\text{track}}^{\text{MC}}$ . Note that in [1], the TPC-gas has been used and now the calibration wires. Therefore, the subscript "gas" has been replaced by "wire" here. According to these equations, one would assume a ratio  $\Omega_i/\omega_i$  of 1 if the ratio  $\varepsilon_{\gamma,\text{wire}}/\varepsilon_{\text{track}}$  is reproduced in Monte Carlo. The results are depicted in figure 5.14. The ratios determined for the different radial intervals match very well. As the ratio is at a level of around  $\Omega_i/\omega_i \approx 0.80$ , this is not yet the case. This leads to the assumption that the reconstruction efficiency of photons in the wire as reference and/or the charged particle reconstruction efficiency are not yet reproduced in Monte Carlo. An additional difference can come from the fact that secondaries are not yet subtracted in the data.

## 5.7 Conclusions on the material budget

In this part of the thesis, different steps of the analysis were described and selected results were presented. As it was seen in the analysis, some pieces of material are not

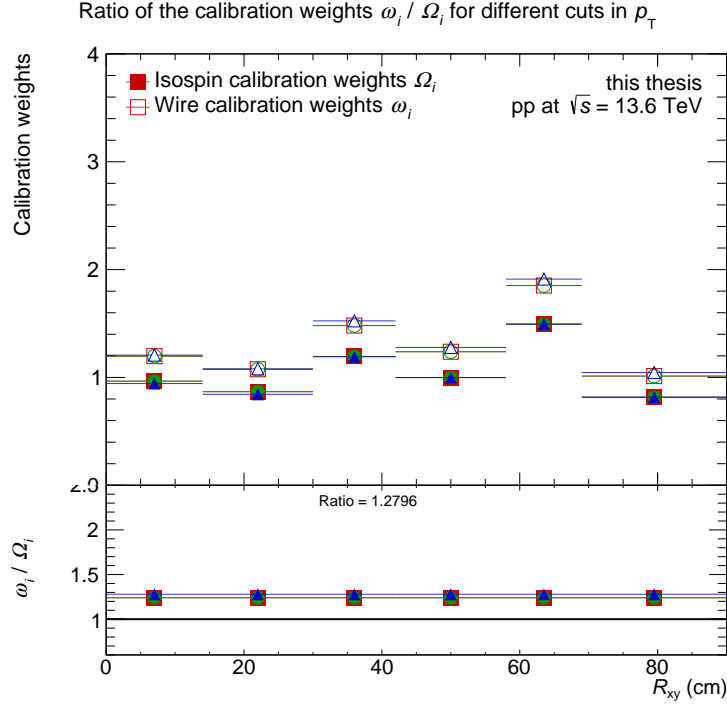


Figure 5.14: Distribution of the two estimated calibration weights  $\Omega_i$  and  $\omega_i$  as a function of the radial position using data LHC22f and Monte Carlo LHC23d1k and their ratio on the bottom.

yet implemented in the Monte Carlo. These were identified and communicated to the experts.

Looking at the determined reconstruction efficiency, one can see that it can still be improved. Here, it is important to acknowledge, that the calibration is still ongoing and also secondaries and other combinatorics can influence the efficiency. This can also be seen when looking at the Monte Carlo simulation that has been reconstructed as data depicting the purity of the photon sample.

In addition, a first estimate of the calibration weights  $\Omega_i$  and  $\omega_i$  was provided. As the ratio of the two calibration weights suggests, there are still effects, that need to be considered.

# 6 Photon momentum resolution using neutral pions

Pions are mesons consisting of the lightest quarks  $u$  and  $d$ . In total there are three different pion states with different quark contents [4]:

$$|\pi^+\rangle = |u\bar{d}\rangle, \quad m(\pi^+) = 139.57 \text{ MeV}/c^2 \quad (6.1)$$

$$|\pi^-\rangle = |\bar{u}d\rangle, \quad m(\pi^-) = 139.57 \text{ MeV}/c^2 \quad (6.2)$$

$$|\pi^0\rangle = \frac{1}{\sqrt{2}} [ |u\bar{u}\rangle - |d\bar{d}\rangle ], \quad m(\pi^0) = 134.97 \text{ MeV}/c^2 \quad (6.3)$$

As they are the lightest particles and make up the biggest part of particles produced in collisions, they are rather well known. For this analysis, the two photon decay channel of the neutral pion is used. Its branching ratio is [4]

$$Br(\pi^0 \rightarrow 2\gamma) = (98.823 \pm 0.034) \% \quad (6.4)$$

The photons can then each convert into an electron positron pair when traversing the detector material

$$\pi^0 \rightarrow 2\gamma \rightarrow 2(e^+ + e^-). \quad (6.5)$$

Despite their neutral electric charge, they can be used to study the charged particle momentum resolution and assesses the goodness of the calibration as well as to know how good is the agreement between data and Monte Carlo reconstruction. In addition, the photon momentum resolution itself is of interest when measuring  $\pi^0$  and  $\eta$  mesons and direct photons. As the photons are reconstructed via  $e^+e^-$  pairs, the measurement is affected by electron Bremsstrahlung.

In the first section, the details of the neutral pion analysis will be explained. The goal is to obtain the  $p_T$ -differential raw pion yield for the different cuts / types of V0 defined in table 4.1. For that, first the  $\pi^0$  signal is identified in a two photon invariant mass distribution. For Monte Carlo, this can be done directly by using the MC information whereas for data the signal appears on top of a combinatorial background. One can identify the peak already before subtracting. But in order to quantify the yield, the subtraction of the combinatorial background is needed. In a next step, the  $\pi^0$  invariant mass is fitted to acquire the peak position and width. Those are used to set the integration ranges to then calculate the pion raw yield.

This is done for the different cuts illustrated in chapter 4 in order to compare them. The process is repeated for the different data sets listed in table 4.2. In the end of this

section, the results for the different data sets will be compared.

## 6.1 Neutral pion reconstruction

### 6.1.1 Fit on $\pi^0$ invariant mass

To determine the mass of reconstructed pions, one can calculate the invariant mass  $M_{\gamma\gamma}$  of all photon pairs in each event. Neutral pions appear as a peak around the rest-mass in a  $\gamma\gamma$  invariant mass distribution on top of a combinatorial background. This can be done by using the four momenta of the two photons given by

$$p_{\gamma i}^{\mu} = \left( \frac{E_{\gamma i}}{c}, \mathbf{p}_{\gamma i} \right), \quad i = 1, 2 \quad (6.6)$$

The invariant mass is then calculated by

$$M_{\gamma\gamma}^2 = (E_{\gamma 1} + E_{\gamma 2})^2 - \|\mathbf{p}_{\gamma 1} + \mathbf{p}_{\gamma 2}\|^2 \quad (6.7)$$

$$= 2E_{\gamma 1}E_{\gamma 2}(1 - \cos \theta_{12}) \quad (6.8)$$

with  $E_{\gamma 1,2}$  the energy and  $\theta_{12}$  the opening angle between the photons.

The analysis is done differentially in the pair transverse momentum. The width of the intervals is chosen to acquire enough statistics for a reliable analysis.

The goal is to extract the  $\pi^0$  peak mean and width. Therefore, the spectrum of  $p_T$  vs.  $M_{\gamma\gamma}$  is first split in different  $p_T$  intervals. They are given in table 6.1.

$0.40 \text{ GeV}/c \leq p_T \leq 0.80 \text{ GeV}/c$
$0.80 \text{ GeV}/c \leq p_T \leq 1.20 \text{ GeV}/c$
$1.20 \text{ GeV}/c \leq p_T \leq 1.60 \text{ GeV}/c$
$1.60 \text{ GeV}/c \leq p_T \leq 2.00 \text{ GeV}/c$
$2.00 \text{ GeV}/c \leq p_T \leq 3.00 \text{ GeV}/c$
$3.00 \text{ GeV}/c \leq p_T \leq 4.00 \text{ GeV}/c$
$4.00 \text{ GeV}/c \leq p_T \leq 6.00 \text{ GeV}/c$
$6.00 \text{ GeV}/c \leq p_T \leq 12.00 \text{ GeV}/c$

Table 6.1: Overview of the intervals in  $p_T$  for the pion invariant mass analysis

As the  $\pi^0$  peak appears above a combinatorial background, the background has to be subtracted to analyse the neutral pion invariant mass in the  $\gamma\gamma$  invariant mass distribution.

This can be done by using the mixed events, i.e. by combining measured photons from different events. This implies that the two photons can never stem from the

same pion and therefore the mass spectrum does not have an invariant mass peak. The mixed events can then be scaled to the same events by choosing an integral with boundaries outside the visible peak in the same events. The received histogram still has a remaining background that can however be modelled by including a polynomial function in the fit function for the invariant mass peak.

Contrary to data, this subtraction is not necessary in the Monte Carlo simulation as it is known that the photons stem from the same pion as the *MC truth* can be used.

As a fit function a Gaussian is used that has been modified with an exponential tail on the left in order to model the Bremsstrahlung tail on the left of the peak. As the photons are reconstructed via  $e^+e^-$  pairs, they are affected by electron Bremsstrahlung and this has to be taken into account in the fit function. The fit function is given by

$$f_{\text{data}}(M_{\gamma\gamma}) = \begin{cases} A \cdot \left[ G(M_{\gamma\gamma}) + \exp\left(\frac{M_{\gamma\gamma} - M_{\pi^0}}{\lambda}\right) [1 - G(M_{\gamma\gamma})] \right] + B + C \cdot M_{\gamma\gamma}, & x < M_{\pi^0} \\ A \cdot [G(M_{\gamma\gamma})] + B + C \cdot M_{\gamma\gamma}, & x \geq M_{\pi^0} \end{cases} \quad (6.9)$$

with the Gaussian

$$G(M_{\gamma\gamma}) = \exp\left(-\frac{1}{2} \left(\frac{M_{\gamma\gamma} - M_{\pi^0}}{\sigma}\right)^2\right). \quad (6.10)$$

For the Monte Carlo the same equation is used except there is no need for the remaining background polynomial:

$$f_{\text{MC}}(M_{\gamma\gamma}) = \begin{cases} A \cdot \left[ G(M_{\gamma\gamma}) + \exp\left(\frac{M_{\gamma\gamma} - M_{\pi^0}}{\lambda}\right) [1 - G(M_{\gamma\gamma})] \right], & x < M_{\pi^0} \\ A \cdot [G(M_{\gamma\gamma})], & x \geq M_{\pi^0} \end{cases} \quad (6.11)$$

The parameters of the functions are given in table 6.2.

variable	parameter
A	amplitude
$\sigma$	standard deviation of the Gaussian
$\lambda$	inverse slope of the Bremsstrahlung tail
$M_{\pi^0}$	reconstructed peak position of the $\pi^0$
B	offset of the remaining background
C	linear slope of the remaining background

Table 6.2: Fit parameters used for asymmetric Gaussian

The peak position and peak width can be obtained with the fit function. However, the fit function is not being used to get the yield but rather to determine the integration range for the pion yield. An example of the fits in a  $p_T$  range of  $0.4 \text{ GeV}/c \leq p_T \leq 0.9 \text{ GeV}/c$  for the different track selections is shown in figure 6.1. The blue points in figure 6.1 represent the real event subtracted by the scaled background. The red solid

line is the obtained fit.

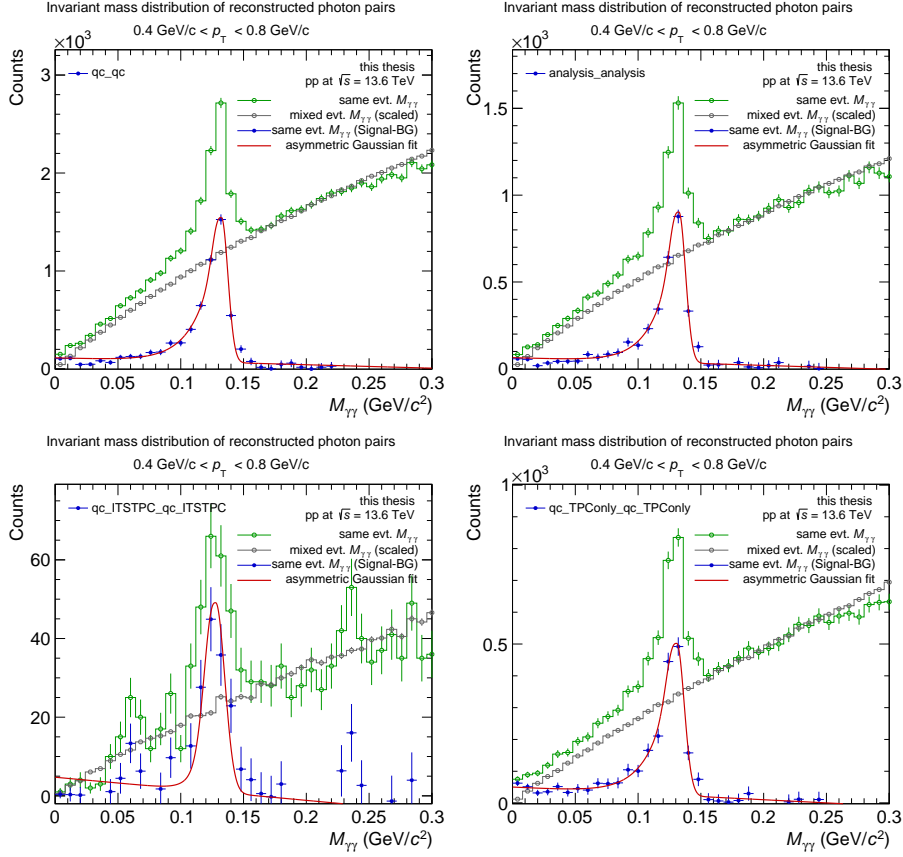


Figure 6.1: Overview on invariant mass distribution of reconstructed photon pairs  $M_{\gamma\gamma}$  around the rest mass of  $\pi^0$  ( $135 \text{ MeV}/c^2$ ) for the different cuts qc, analysis, ITSTPC and TPCOnly from upper left to lower right, respectively. The green and gray histograms represent the same- and mixed-events (scaled to the same-events histogram) respectively. In blue, the data after subtraction of the combinatorial background is shown and in red the fitted asymmetric Gaussian with the remaining background. All plots are for a pair- $p_T$  interval of  $0.4 \text{ GeV}/c \leq p_T \leq 0.8 \text{ GeV}/c$ .

The fitting process is repeated in all  $p_T$ -ranges defined in table 6.1. In addition, this process is then repeated for the different cuts that have been explained in chapter 4. Namely, those are the cuts: qc, analysis, ITSTPC and TPCOnly. The resulting peak position and peak width as a function of  $p_T$  for the different cuts is shown in 6.2. The fitted invariant mass distributions can be found in appendix A.2.2. In figure 6.2, the different cuts are indicated by the different colours. One can see that the cut ITSTPC has an overall lower mean and FWHM than the other cuts and that the cuts qc and analysis obtain very similar values.

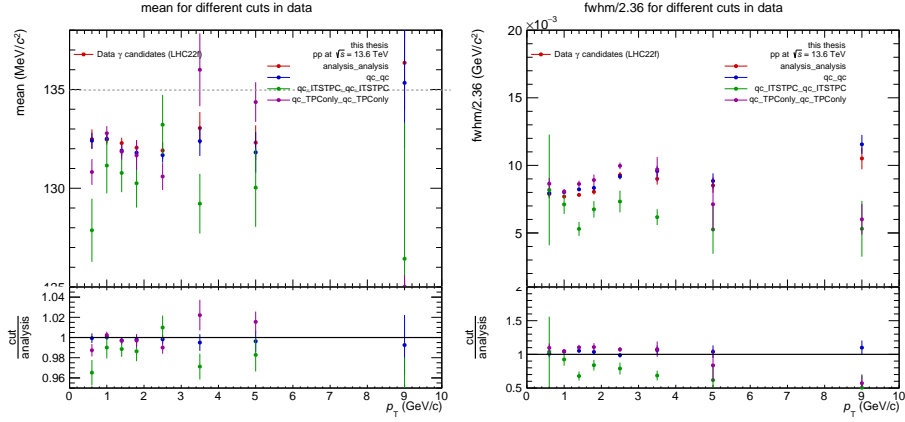


Figure 6.2: Overview on the determined mean and FWHM/2.36 of the  $\pi^0$  invariant mass fit as a function of the transverse momentum  $p_T$  for LHC22f for the different cuts qc (red), analysis (blue), ITSTPC (green) and TPCOnly (violet)

### 6.1.2 Yield extraction

To get the  $\pi^0$  yield, the invariant mass peak obtained after subtraction of the mixed event background is integrated. This needs to be done in an asymmetric window in order to include the Bremsstrahlung tail. The chosen integration ranges can be found in table 6.3. As the invariant mass peak obtained after subtraction still contains a

Lower integration limit $M_{\text{low}}^{\pi^0}$	Upper integration limit $M_{\text{high}}^{\pi^0}$
$M_{\pi^0} - 0.035 \text{ GeV}/c^2$	$M_{\pi^0} + 0.02 \text{ GeV}/c^2$

Table 6.3: Integration ranges for the yield extraction

residual background, the fit function was extended by a linear polynomial. To get the raw yield, this remaining linear background is integrated and subtracted from the  $\pi^0$  signal integral. Therefore, the complete raw yield is calculated as follows:

$$N_{\text{raw}}^{\pi^0} = \int_{M_{\text{low}}^{\pi^0}}^{M_{\text{high}}^{\pi^0}} (N_{\gamma\gamma} - N_{\text{comb. BG}}) dM_{\gamma\gamma} - \int_{M_{\text{low}}^{\pi^0}}^{M_{\text{high}}^{\pi^0}} (B + C \cdot M_{\gamma\gamma}) dM_{\gamma\gamma} \quad (6.12)$$

From that, the raw yield distribution in  $p_T$  can be acquired which is shown in figure 6.3 again for the data set LHC22f. Again, the same cuts were used as in the fitting process to determine the mean and FWHM.

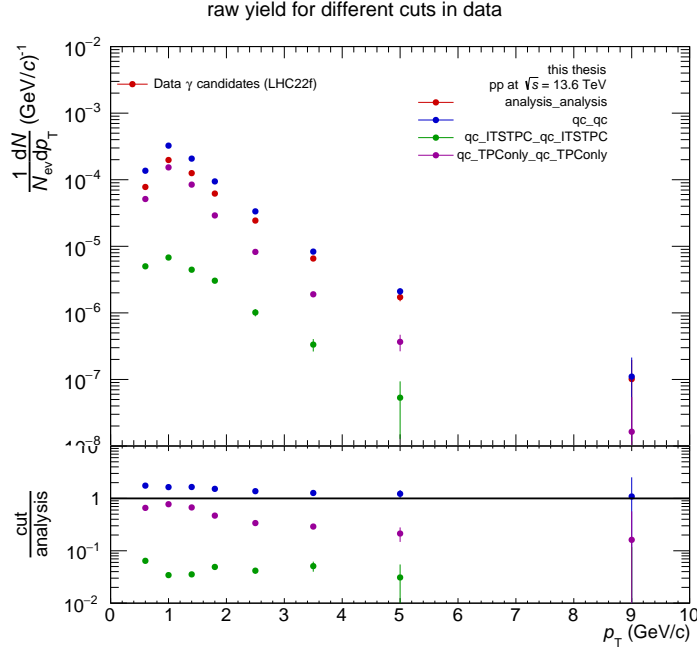


Figure 6.3: Calculated raw yield per event as a function of the transverse momentum  $p_T$  for LHC22f for the different cuts qc (red), analysis (blue), ITSTPC (green) and TPConly (violet)

As visible in figure 6.3, TPConly tracks have a higher yield than ITSTPC tracks. As the cuts analysis and qc include ITSTPC and TPConly tracks, TPConly tracks are very important to enhance the efficiency.

## 6.2 Comparison of $\pi^0$ invariant mass fit and raw yield

This process of obtaining the raw pion yield can now be repeated for the different data sets listed in table 4.2. The detailed results are given in the appendix in section A.2.

### 6.2.1 Comparison of data LHC22f and anchored Monte Carlo LHC23d1k

In a first step, the data LHC22f and its anchored Monte Carlo LHC23d1k can be compared. Note that the results for LHC22f were also used to describe the fitting and yield extraction process earlier in this section. Therefore, some of the values in the following histograms repeated. In figure 6.4, the mean and the FWHM determined in the fitting process as well as the raw yield calculated according to equation 6.12 are shown for the cuts qc (red), analysis (blue), ITSTPC (green) and TPConly (violet) the full markers represent data LHC22f and the empty markers Monte Carlo LHC23d1k. In each plot,

## 6 PHOTON MOMENTUM RESOLUTION USING NEUTRAL PIONS

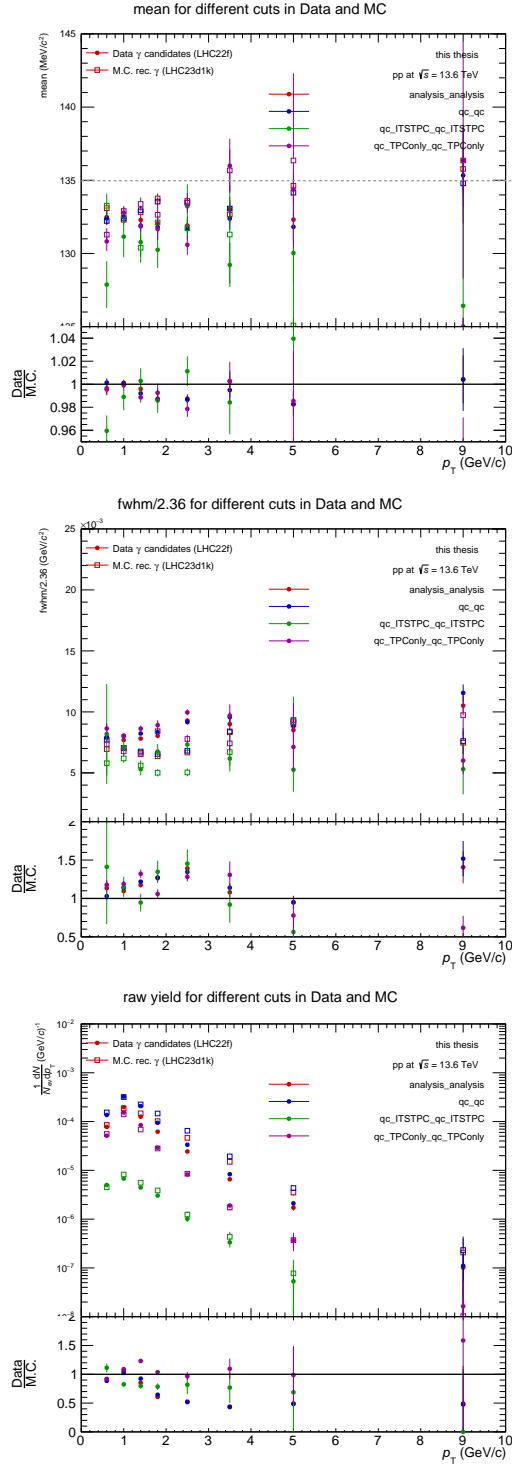


Figure 6.4: Mean (top) and FWHM (middle for the  $\pi^0$  invariant mass and the raw yield (bottom) for LHC22f and its Monte Carlo LHC23d1k and their comparison

the ratio of data divided by Monte Carlo is given on the bottom.

The estimated peak position is almost always under the PDG value of  $M_{\pi^0} = 134.97 \text{ MeV}/c^2$  including the error-bars. Here, one has to take into account the prominent Bremsstrahlung tail on the left of the neutral pion invariant mass peak, which leads to deviations of the maximum of the peak. Ideally, Monte Carlo and data should show the same behaviour in lowering the neutral pion peak position due to Bremsstrahlung. Looking at the ratio of data divided by Monte Carlo for the estimated mean, one can see the very little deviation from 1 of maximal 4%. Therefore, this seems to be the case.

For the mean as well as the FWHM, one can see that the results for the cuts qc and analysis are very close. This can be explained by only having little differences between the values defining the cuts in table 4.1. Also, one can see that for almost all  $p_T$ -bins, the cut TPConly usually has the largest value for the mean and the FWHM whereas the cut ITSTPC usually leads to the smallest value for a single  $p_T$ -bin.

The smaller values for ITSTPC can be explained by the fact that the photon conversions have to happen comparably early in order to classify as ITSTPC. However, in order to reach the TPC, the  $e^+e^-$  pair traverses much more material. This leads to a larger Bremsstrahlung tail and therefore a peak at lower mass. In contrast, the photon conversions classified as TPConly happen at larger radii. This leads to the  $e^+e^-$  pair experiencing way less material resulting in less Bremsstrahlung.

The yields calculated in the different cuts for data and Monte Carlo show an overall matching behaviour but with increasing transverse momentum Monte Carlo usually has a larger yield than data.

In conclusion, it was observed that the determined mean matched well for data LHC22f and its anchored Monte Carlo within the current uncertainties. However, the peak width for data and Monte Carlo does not match within the error bars and is different by up to 50%. The  $\pi^0$  is reconstructed using conversions: each  $\pi^0$  uses four charged tracks. Taking this into account plus the fact that the statistics decreases drastically with increasing  $p_T$ , it is only possible to probe the low  $p_T$  region and in this region, multiple scattering is dominant. In contrast, at high transverse momentum, there are many more effects that need to be taken into account which also leads to less reconstruction efficiency and therefore smaller yields.

In addition, many of the tracks stemming from neutral pions are TPConly tracks. Thus, they convert at larger radii. Therefore, the electron/positron experience a different amount of material and the momentum is determined only by the TPC. However, primary tracks travel through all the material and the momentum is determined by the ITS and the TPC. Therefore, for low  $p_T$  the TPConly tracks are less influenced by Bremsstrahlung than ITSTPC tracks as they traverse less material.

## 6.2.2 Comparison of the data sets LHC22f, LHC23zc and LHC22o min. Bias

In this section, instead of data and Monte Carlo, different data sets will be compared. Namely, the differences between the data sets LHC22f, LHC23zc and LHC22o min. Bias will be investigated and their results of the neutral pion analysis will be compared with each other. The structure of the plots in figure 6.5 is the same as in the section before. For clarity reasons, only the cut qc is studied as this cut has the largest statistics and the comparison for the other cuts would get repetitive.

In figure 6.5, the mean, the FWHM and the calculated raw yield are shown. The data set LHC22f is represented by red circular, LHC23zc by blue rectangular and LHC22o min. Bias by green triangular markers. The comparison via ratio on the bottom of each plot is given by data set divided by LHC22f as this one has the largest statistics. As before in the comparison between data LHC22f and Monte Carlo LHC23d1k, the mean shown in the upper plot is almost always lower than the PDG value for the pion invariant mass marked with the grey dotted line. In addition, the values determined for LHC23zc are mostly the largest values followed by LHC22o min. Bias, whereas the values determined for LHC22f are the lowest values in most cases. Nevertheless, the deviations between the different data sets are small as the determined values differ around 1% for LHC23zc from LHC22f and around 2% for LHC22o min. Bias.

A similar observation can be made for the determined FWHM: Here, the values determined for the different data sets are also very close resulting in differences of less than 2% for LHC23zc and LHC22o min. Bias from LHC22f. Contrary to having mostly upward deviations for the fitted mean, the FWHM deviates up- and downwards.

One could conclude that the small differences for the FWHM and the mean should also lead to small deviations for the calculated raw yield. However, this is not the case. Looking at the determined raw yields for the different data sets, one can see ratios ranging from around 0.01 to 0.1. Here one sees that for runs with larger interaction rate (see table 4.2) the raw yield is smaller than for low interaction rate. In addition, comparing LHC23zc and LHC22o min. Bias having similar interaction rates, LHC23zc with the best calibration available shows the larger raw yield per event. The fact that even with the best calibration available, the  $\pi^0$  raw yields in runs with intermediate interaction rate are still much lower than for low interaction rate runs, evidenced the need for a new V0 finder. Indeed, a V0 finder development including TPConly tracks and being done during tracking, was undertaken [39].

## 6 PHOTON MOMENTUM RESOLUTION USING NEUTRAL PIONS

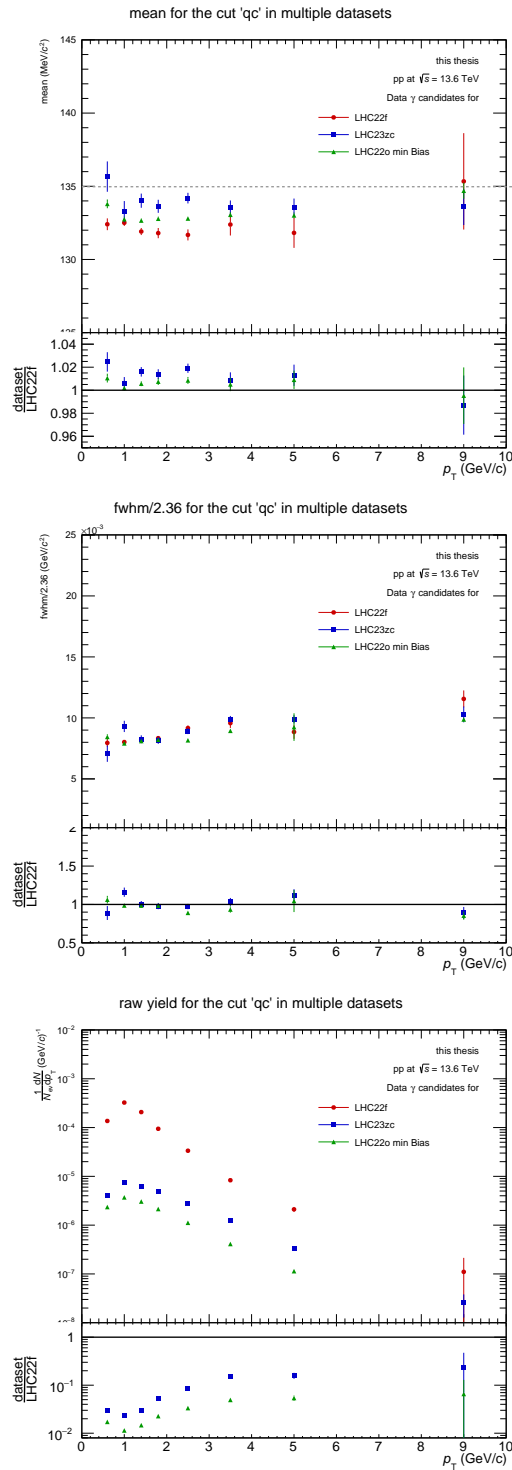


Figure 6.5: Mean (top) and FWHM (middle for the  $\pi^0$  invariant mass and the raw yield (bottom) for LHC22f, LHC23zc and LHC22o min. Bias and their comparison

# 7 Summary and Outlook

In this thesis, the performance of the Photon Conversion Method has been investigated. Starting with studies on the material budget of the ALICE detector in a radial interval of  $0 \text{ cm} \leq R_{xy} \leq 90 \text{ cm}$  the detector material implementation was helped to be improved for the upgraded detector in Run 3. In a next step, a first estimation of calibration weights using wires installed in the ITS2, respectively pion-isospin symmetry was presented. Finally, the pion invariant mass was used to investigate the photon momentum resolution.

## Material budget

During the work on this thesis, a detailed analysis of the material budget was performed. This led to observing pieces of material that are not yet implemented in the Monte Carlo simulation. They were identified and communicated to experts working on the detector material implementation into the simulation.

In a next step, the reconstruction efficiency was determined and one could see that this could still be improved. It is important to acknowledge that at this stage of Run 3, the calibration has not yet converged. Therefore, one should take a second look once the ongoing calibration is finished. The fact, that the work can be further improved in the future could also be seen at the purity of the photon sample. Especially for larger radii, increasing deviations could be observed. These could for example stem from contamination from other neutral particles or combinatorial background. As in the Monte Carlo reconstruction, only primary photons are used this could explain the difference when reconstructing Monte Carlo as data.

In a last step of the material budget investigation, calibration weights using pion-isospin and calibration wires, respectively, have been estimated. As a measure of how good the two calibration weights are matching, their ratio was determined. Here one could observe a deviation from the expectation value of one. This indicates that there are still effects that have not yet been taken into account. Like the reconstruction efficiency, this is a topic that should be further investigated.

## Photon momentum resolution

The photon momentum resolution and momentum scale was studied using the two photon decay of the neutral pion  $\pi^0$ . To do so, the pion in the two photon invariant mass spectrum was fitted. From that the peak position and peak width could be determined and the raw yield was calculated.

With that, one could first check how well the Monte Carlo matched the data. It was observed, that the determined mean matched well within the current uncertainties and the FWHM is different by up to 50%. The raw yield only matched at low  $p_T$  and with increasing  $p_T$  the deviation increased. Looking at the different cuts, one could see that the photon conversions labelled TPConly make up a large part of the conversions in qc and analysis. In addition, the Bremsstrahlung was observed to be more prominent in ITSTPC leading to usually lower  $\pi^0$  peak position values.

Starting with the data set LHC22f, it was also possible to compare different data sets with different properties. As seen before, the determined mean was mostly lower than the PDG values because of the Bremsstrahlung tail. The deviation between the data sets for FWHM and mean was small which leads to the conclusion that the influence of properties such as interaction rate on the neutral pion peak position and width is quite small. Contrary to this conclusion, the raw yield was influenced significantly by the different interaction rates as well as the optimised calibration in LHC23zc: Compared to LHC22f the raw yield for LHC22o minimum Bias and LHC23zc are lower. This is because the V0 finder used in this analysis works best at low interaction rates. In addition, one could observe, that the raw yield for LHC23zc is higher than for LHC22o minimum Bias which could be explained by the updated calibration.

## Outlook

At this point of Run 3, there is still much development happening. For this reason, some results presented in this thesis are only preliminary and are expected to be better in the future. Especially the implementation of the detector into the Monte Carlo simulation is going to become better. Here, the methods developed during this thesis could help to check the implementation during the updates. In addition, it would be useful to check the reconstruction efficiency as well as the photon sample purity again once the calibration has converged.

Looking at the ratio of the calibration weights which is currently still differing from one, this would also be a part that could be looked at again. In order to successfully calculate the calibration weights, it is also important to subtract secondaries, other neutral particles and combinatorial background from the reconstructed photons. However, data to proceed with this is not yet available and a full determination of the calibration weights as in Run 2 is beyond the scope of a bachelor's thesis. But the current value of the calibration weights and their ratio carries valuable information about how well the performance of the reconstruction on data and Monte Carlo matches. For the photon momentum resolution, it would also be interesting to study the neutral pion in other cuts as well as data sets. This should lead to increasing precision of the measurement that could be helpful to determine differences in the reconstruction and also for the new V0 finder.

In conclusion, this thesis was able to identify missing material in the Monte Carlo simulation, to give a first estimate on calibration weights and to investigate the photon momentum resolution in different data sets. As mentioned in the beginning, at this point of the analysis in Run 3, there are still many factors that should be included in the analysis. But nevertheless, this thesis enabled the first step to study the performance of photon measurements using PCM in Run 3.

# A Appendix

## A.1 Studies on material budget

### A.1.1 Analysis Tasks

Analysis Tasks Material Budget	
Monte Carlo LHC23d1k (HL155278)	Data LHC22f (HL125184) <sup>1</sup>
o2-analysis-em-associate-mc-info	–
o2-analysis-em-material-budget-mc	o2-analysis-em-material-budget
o2-analysis-em-pcm-qc-mc	o2-analysis-em-pcm-qc
o2-analysis-em-create-pcm	
o2-analysis-em-skimmer-gamma-conversion	
o2-analysis-pid-tpc-base	
o2-analysis-pid-tpc-full	
o2-analysis-em-create-emreduced-event	
o2-analysis-track-propagation	
o2-analysis-bc-converter	
o2-analysis-event-selection	
o2-analysis-centrality-table	
o2-analysis-multiplicity table	
o2-analysis-pid-tpc-base	
o2-analysis-pid-tpc-full	
o2-analysis-timestamp	
o2-analysis-tracks-extra-converter	

Table A.1: Overview of the tasks used for the data used for the material budget in chapter 5

### A.1.2 Integrated plots

On the following pages, a complete overview of the study on material budget is given. Datasets used are LHC22f for data and LHC23d1k for MC.

<sup>1</sup>The numbers refer to the hyperloop train numbers

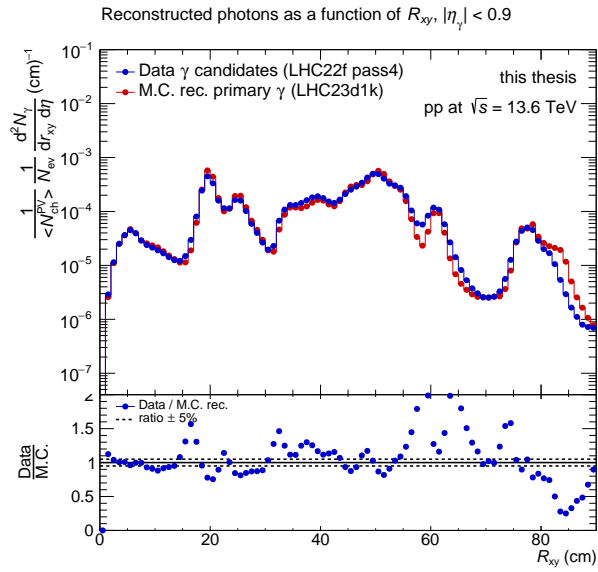


Figure A.1: Number of reconstructed photons (normalised) as a function of  $R_{xy}$  for data and reconstructed MC

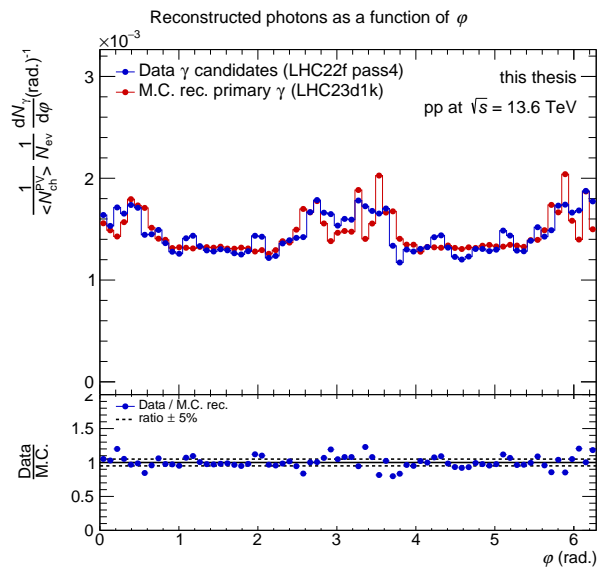


Figure A.2: Number of reconstructed photons (normalised) as a function of  $\varphi$  for data and reconstructed MC

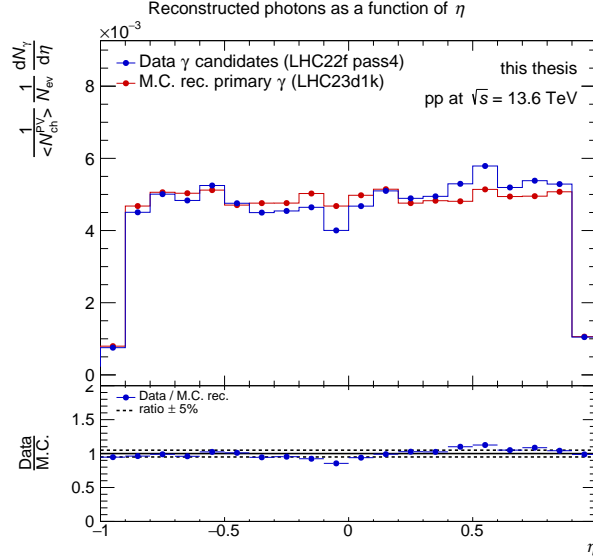


Figure A.3: Number of reconstructed photons (normalised) as a function of  $\eta$  for data and reconstructed MC

### A.1.3 Two-dimensional plots

In this section, two-dimensional plots are shown for the Conversion point in different planes as well as the material budget in  $\eta$  vs.  $\varphi$  for different radii. The radii correspond to the performed cuts in the next section.

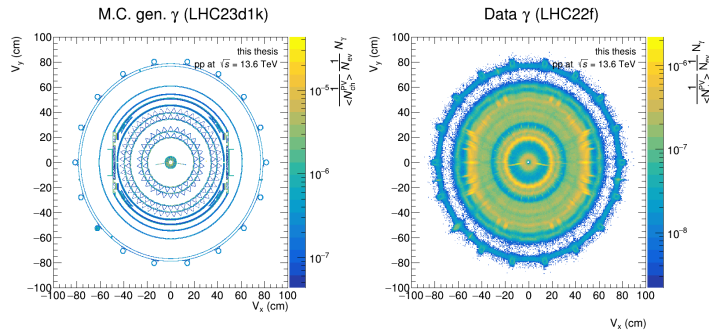


Figure A.4: Conversion points in  $V_x$  vs.  $V_y$  for data and MC generated

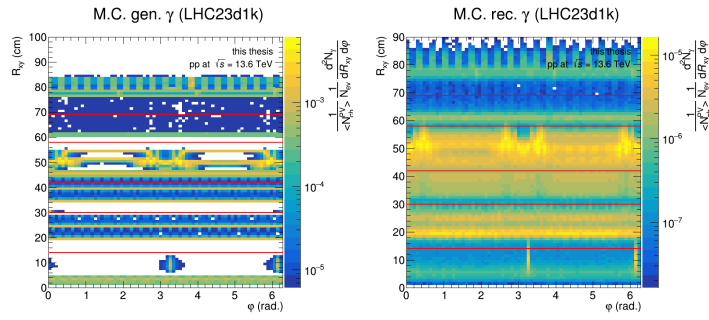


Figure A.5: Conversion points in  $R_{xy}$  vs.  $\varphi$  for MC generated and MC reconstructed

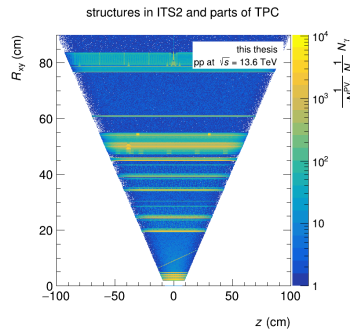


Figure A.6: Conversion points in  $R_{xy}$  vs.  $z$  for MC generated

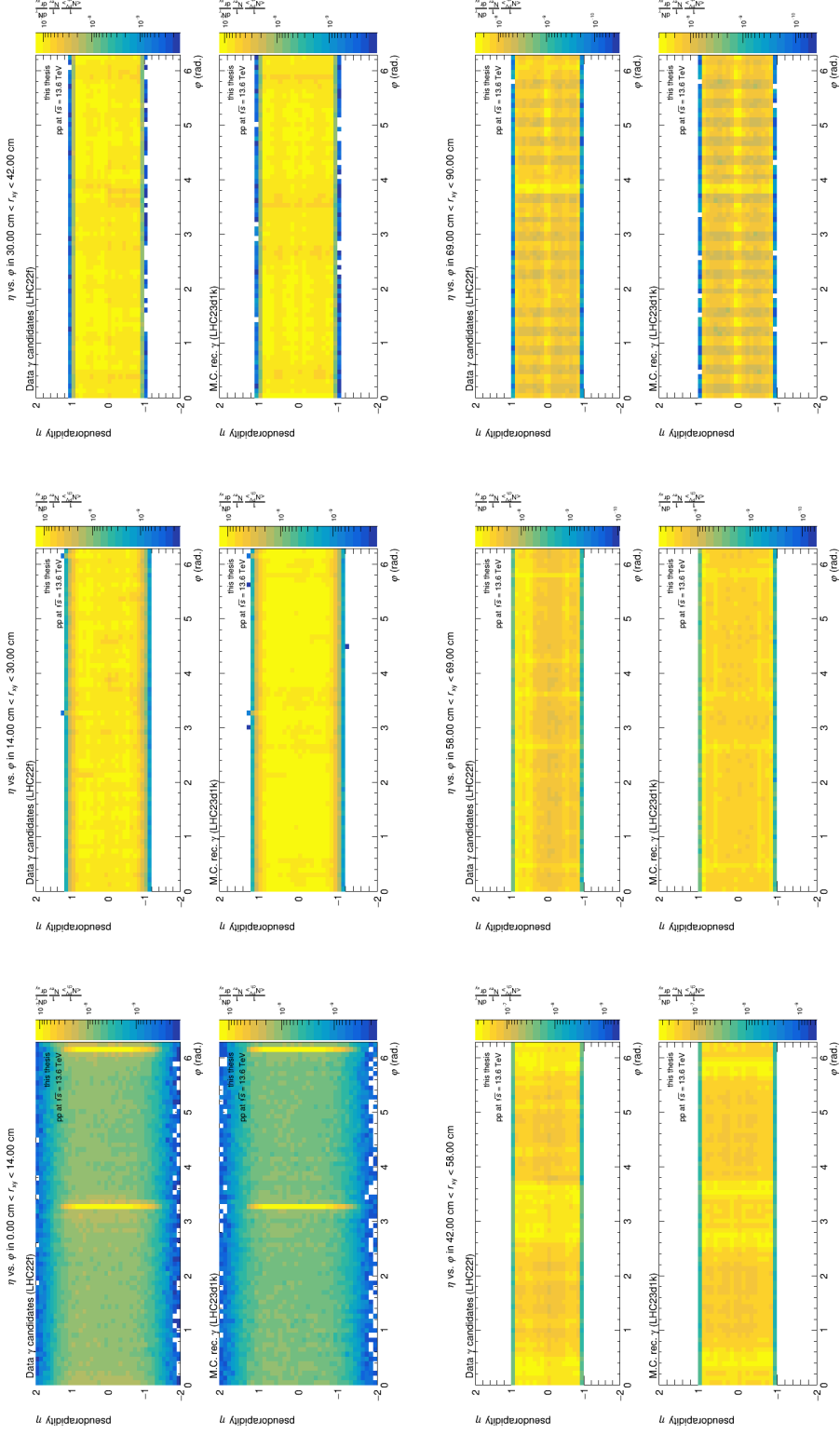


Table A.2:  $\eta$  vs  $\varphi$  distribution of photon conversion points in different radial intervals for data (top) and Monte Carlo (bottom) each.



## A.1.4 Detailed analysis for different radii

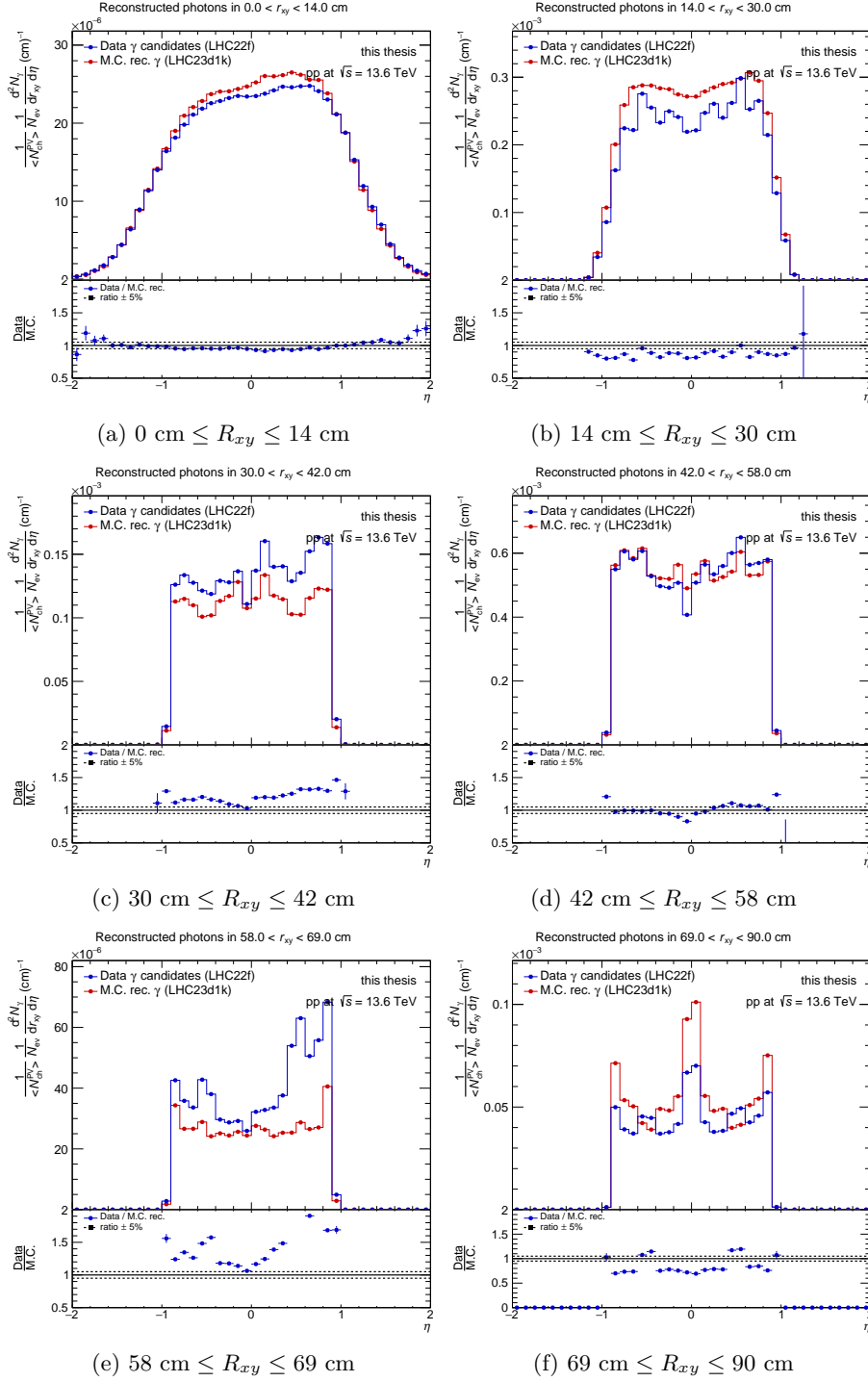
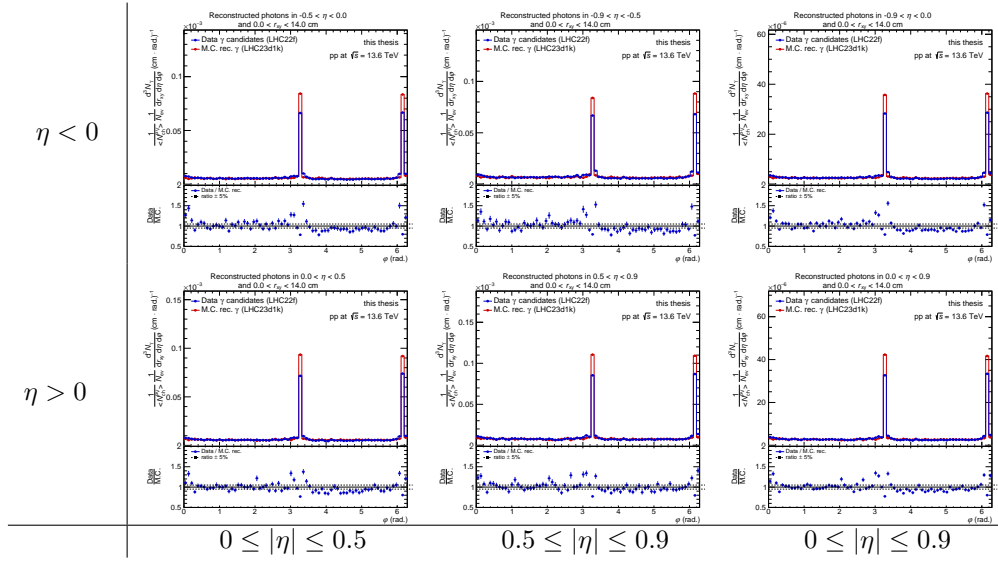
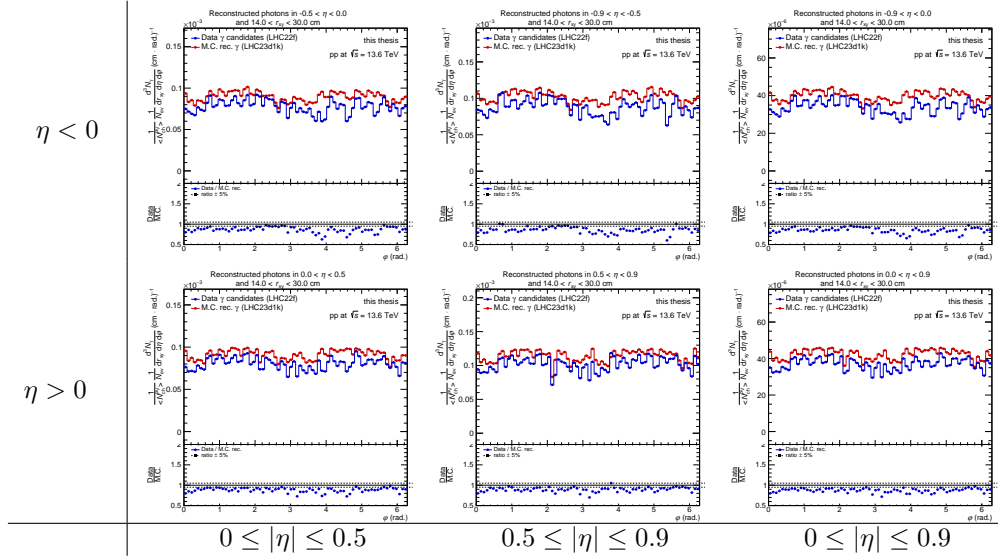


Figure A.7: Distributions of the normalised number of reconstructed photons as a function of  $\eta$  for data and Monte Carlo in different radial intervals according to table 5.2

Table A.3: Material budget in different  $\eta$  for  $0 \text{ cm} \leq R_{xy} \leq 14 \text{ cm}$ Table A.4: Material budget in different  $\eta$  for  $14 \text{ cm} \leq R_{xy} \leq 30 \text{ cm}$

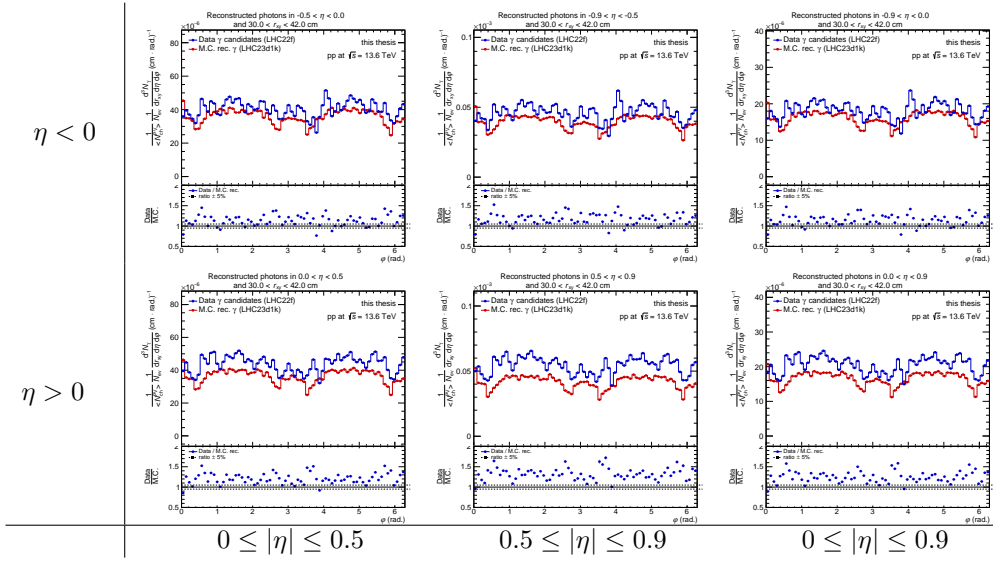


Table A.5: Material budget in different  $\eta$  for  $30 \text{ cm} \leq R_{xy} \leq 42 \text{ cm}$

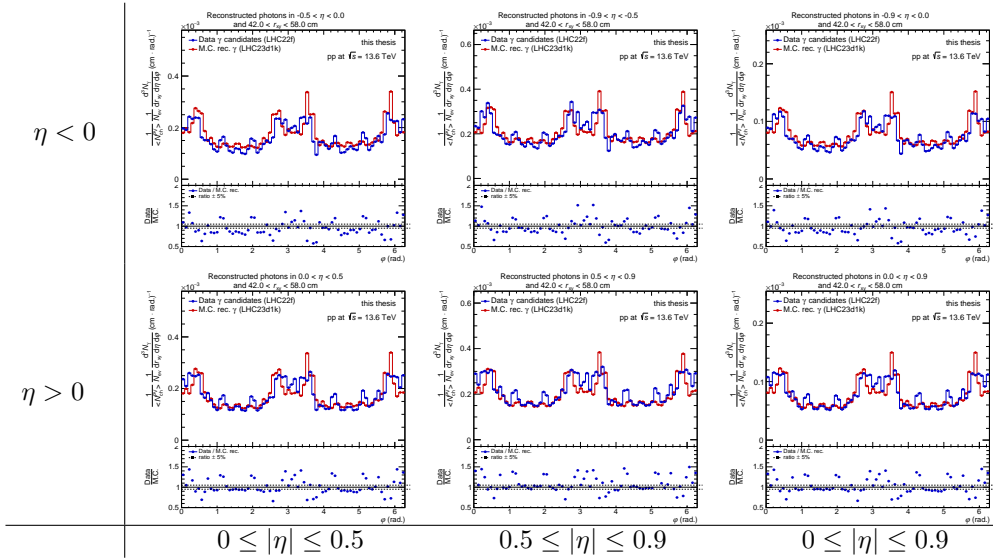


Table A.6: Material budget in different  $\eta$  for  $42 \text{ cm} \leq R_{xy} \leq 58 \text{ cm}$

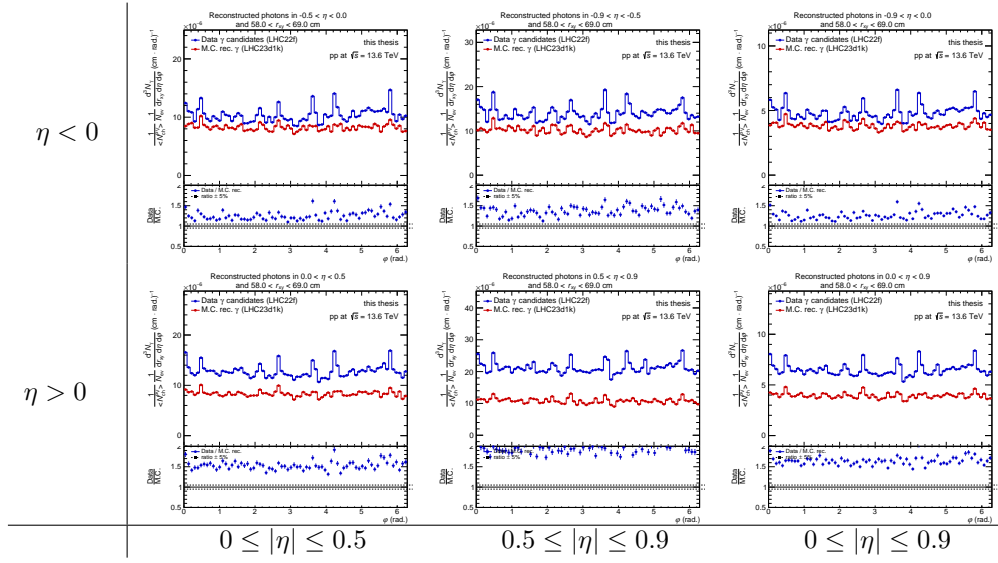


Table A.7: Material budget in different  $\eta$  for  $58 \text{ cm} \leq R_{xy} \leq 69 \text{ cm}$

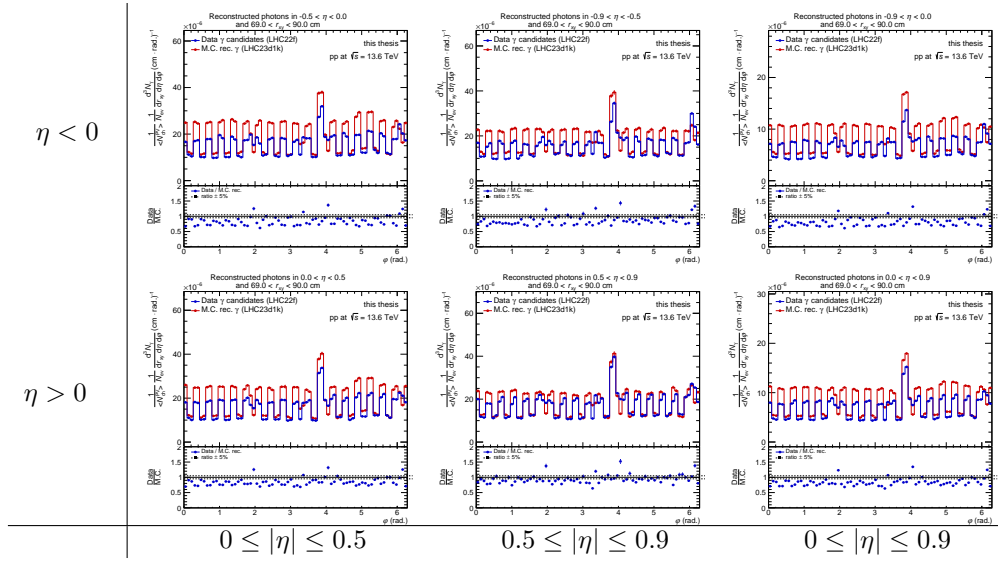


Table A.8: Material budget in different  $\eta$  for  $69 \text{ cm} \leq R_{xy} \leq 90 \text{ cm}$

detector part	$-0.9 \leq \eta \leq 0.0$	$0.0 \leq \eta \leq 0.9$	$-0.9 \leq \eta \leq -0.5$	$-0.5 \leq \eta \leq 0.0$	$0.0 \leq \eta \leq 0.5$	$0.5 \leq \eta \leq 0.9$
upper half	1.13	1.13	1.18	1.18	1.13	1.18
	2.01	2.01	2.01	1.96	1.96	1.96
lower half	4.28	4.28	4.28	4.32	4.28	4.28
	5.15	5.11	5.11	5.15	5.15	5.11

Table A.9: Angular position  $\varphi$ [rad] of the well visible peaks for all cuts in  $\eta$  in a radial interval of  $42 \text{ cm} \leq R_{xy} \leq 58 \text{ cm}$

detector part	$-0.9 \leq \eta \leq 0.0$	$0.0 \leq \eta \leq 0.9$	$-0.9 \leq \eta \leq -0.5$	$-0.5 \leq \eta \leq 0.0$	$0.0 \leq \eta \leq 0.5$	$0.5 \leq \eta \leq 0.9$
upper half	0.04	0.08	0.04	0.04	0.04	0.09
	0.43	0.52	0.44	0.44	0.48	0.52
	2.66	2.71	2.66	2.66	2.67	2.66
	3.58	3.67	3.58	3.58	3.62	3.67
lower half	4.28	4.27	4.27	4.28	4.23	4.27
	5.80	5.49	5.80	5.80	5.71	5.65

Table A.10: Angular position  $\varphi$ [rad] of the well visible peaks for all cuts in  $\eta$  in a radial interval of  $58 \text{ cm} \leq R_{xy} \leq 69 \text{ cm}$

### Overview of the observed deviations in data and Monte Carlo

- $0 \text{ cm} \leq R_{xy} \leq 14 \text{ cm}$ 
  - Wires are represented in MC, but MC 10% above data
  - $\eta$ -distribution similar for data and MC
  - Similar number of rec. gamma for each wire in MC
- $14 \text{ cm} \leq R_{xy} \leq 30 \text{ cm}$ 
  - Slightly more deviation between data and MC between  $\pi \leq \varpi \leq 2\pi$  for negative  $\eta$
  - similar distribution for data and MC
  - good reconstruction of ITS in MC
- $30 \text{ cm} \leq R_{xy} \leq 42 \text{ cm}$ 
  - Overall difference between data and MC
  - less reconstructed photons for MC
  - larger deviation between data and MC for positive  $\eta$
- $42 \text{ cm} \leq R_{xy} \leq 58 \text{ cm}$ 
  - Difference between data and MC for positive  $\eta$
  - Additional peaks In data not visible in MC
  - Structure in data starts to show but in MC not fully represented

- $58 \text{ cm} \leq R_{xy} \leq 69 \text{ cm}$ 
  - Additional peaks in data visible and only partly in MC
  - overall difference between positive and negative  $\eta$  (MC completely below data for positive  $\eta$ )
- $69 \text{ cm} \leq R_{xy} \leq 90 \text{ cm}$ 
  - Start of lack of efficiency
  - Overall more reconstructed photons for MC
  - Lack of statistics in data
  - Structure in MC more prominent than in data

## A.2 Neutral pion reconstruction

On the following pages, first the used analysis tasks are given. Then, an overview of the of the extraction of the neutral pion invariant mass peak and the fit using an asymmetric Gaussian as well as the derived parameters are given for each data set used in the analysis.

### A.2.1 Analysis Tasks

Analysis Tasks photon momentum resolution			
Monte Carlo LHC23d1k (124837)	Data LHC22f (124838)	Data LHC22o min. bias (135860)	Data LHC23zc (134765)
o2-analysis-centrality-table	o2-analysis-centrality-table	o2-analysis-centrality-table	—
o2-analysis-multiplicity-table	o2-analysis-multiplicity-table	o2-analysis-multiplicity-table	o2-analysis-multiplicity-table
—	o2-analysis-cal-clusters	o2-analysis-cal-clusters	—
o2-analysis-je-emcal-correction-task	o2-analysis-je-emcal-correction-task	o2-analysis-je-emcal-correction-task	—
<b>o2-analysis-em-pcm-qc-mc</b>	<b>o2-analysis-em-pcm-qc</b>	<b>o2-analysis-em-pcm-qc</b>	<b>o2-analysis-em-pcm-qc</b>
o2-analysis-em-create-emreduced-mc-event	o2-analysis-em-create-emreduced-event	o2-analysis-em-create-emreduced-event	o2-analysis-em-create-emreduced-event
<b>o2-analysis-em-pi0eta-to-gammagamma</b>	<b>o2-analysis-em-pi0eta-to-gammagamma</b>	<b>o2-analysis-em-pi0eta-to-gammagamma</b>	<b>o2-analysis-em-pi0eta-to-gammagamma</b>
o2-analysis-em-skimmer-gamma-conversion	o2-analysis-em-skimmer-gamma-conversion	o2-analysis-em-skimmer-gamma-conversion	o2-analysis-em-skimmer-gamma-conversion
—	o2-analysis-em-skimmer-gamma-cal	o2-analysis-em-skimmer-gamma-cal	—
—	o2-analysis-em-skimmer-phos	o2-analysis-em-skimmer-phos	—
o2-analysis-em-skimmer-dalitz-ee	o2-analysis-em-skimmer-dalitz-ee	—	—
o2-analysis-track-propagation	o2-analysis-track-propagation	o2-analysis-track-propagation	o2-analysis-track-propagation
—	o2-analysis-trackselection	o2-analysis-trackselection	—
<b>o2-analysis-em-create-pcm</b>	<b>o2-analysis-em-create-pcm</b>	<b>o2-analysis-em-create-pcm</b>	<b>o2-analysis-em-create-pcm</b>
o2-analysis-bc-converter	o2-analysis-bc-converter	o2-analysis-bc-converter	—
o2-analysis-ft0-corrected-table	o2-analysis-ft0-corrected-table	—	o2-analysis-ft0-corrected-table
o2-analysis-event-selection	o2-analysis-event-selection	o2-analysis-event-selection	o2-analysis-event-selection
o2-analysis-pid-tpc-base	o2-analysis-pid-tpc-base	o2-analysis-pid-tpc-base	o2-analysis-pid-tpc-base
o2-analysis-pid-tpc-full	o2-analysis-pid-tpc-full	o2-analysis-pid-tpc-full	o2-analysis-pid-tpc-full
o2-analysis-pid-tof-base	o2-analysis-pid-tof-base	—	—
o2-analysis-pid-tof-beta	o2-analysis-pid-tof-beta	—	—
o2-analysis-pid-tof-full	o2-analysis-pid-tof-full	—	—
o2-analysis-timestamp	o2-analysis-timestamp	o2-analysis-timestamp	o2-analysis-timestamp
—	—	o2-analysis-tracks-extra-converter	o2-analysis-tracks-extra-converter

Table A.11: Overview of the tasks used for the data and MC hyper-loop train runs for the photon momentum resolution studies presented in chapter 6. Note that the the calibration and the software development are still ongoing, which is why different (helper) tasks are used for different data sets.

## A.2.2 Results for LHC22f

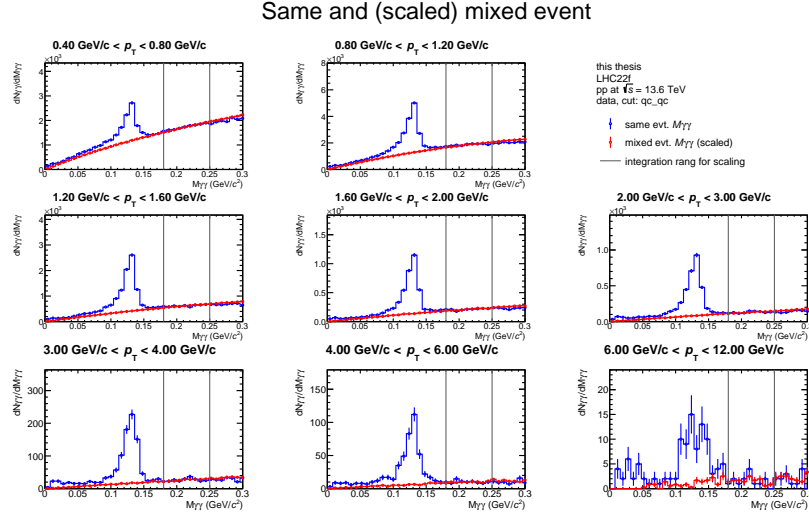


Figure A.8: Overview on the  $\pi^0$  invariant mass fits for the intervals in transverse momentum  $p_T$  for LHC22f and the cut quality control (qc)

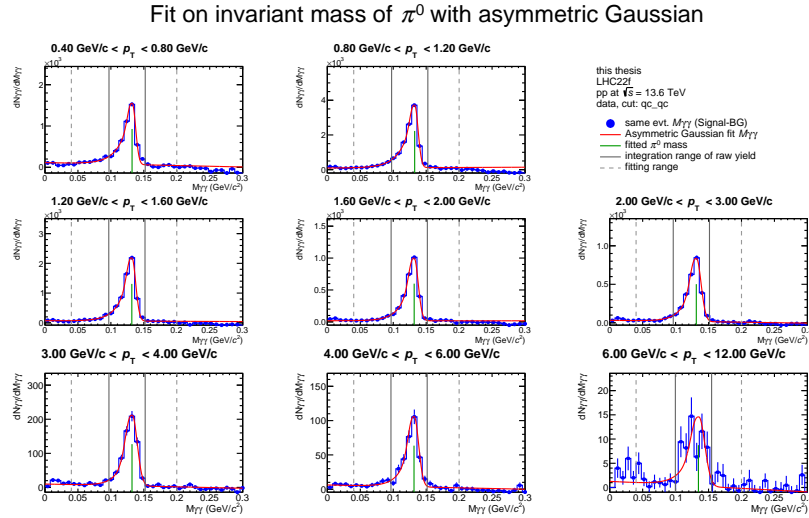


Figure A.9: Overview on the  $\pi^0$  invariant mass fits for the intervals in transverse momentum  $p_T$  for LHC22f and the cut quality control (qc)

Same and (scaled) mixed event

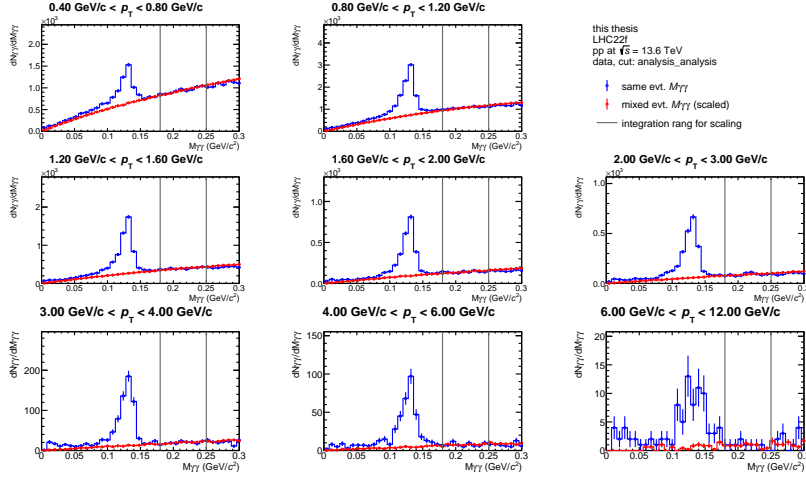


Figure A.10: Overview on the  $\pi^0$  invariant mass fits for the intervals in transverse momentum  $p_T$  for LHC22f and the cut analysis

Fit on invariant mass of  $\pi^0$  with asymmetric Gaussian

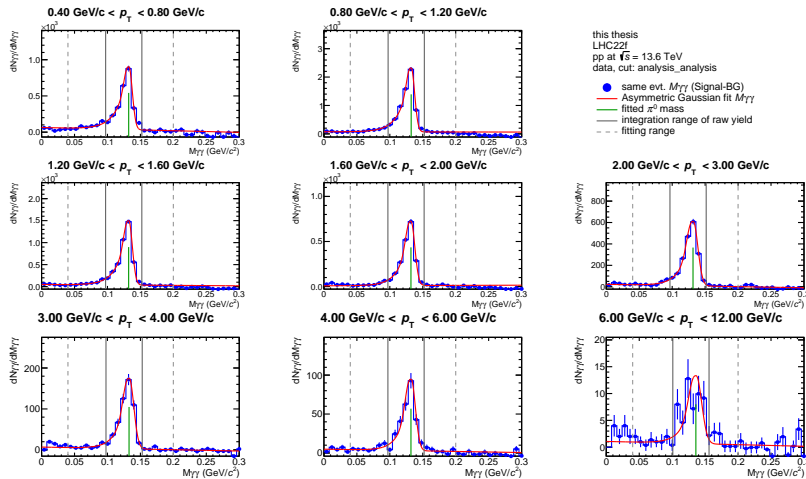


Figure A.11: Overview on the  $\pi^0$  invariant mass fits for the intervals in transverse momentum  $p_T$  for LHC22f and the cut analysis

Same and (scaled) mixed event

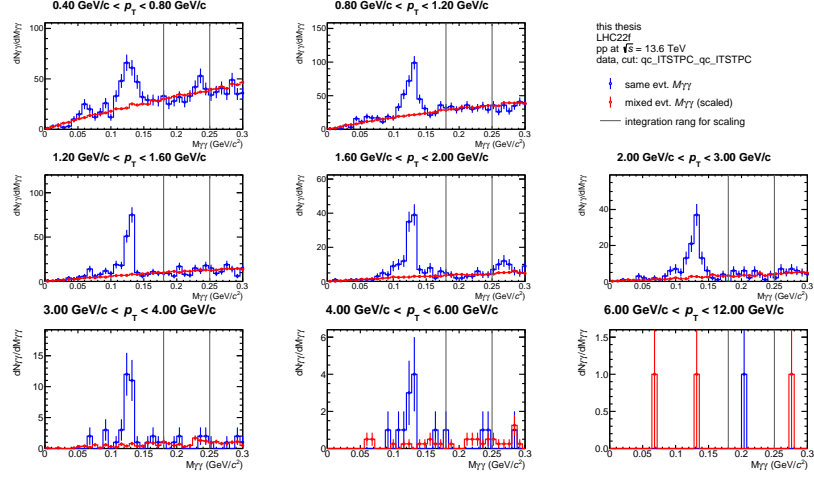


Figure A.12: Overview on the  $\pi^0$  invariant mass fits for the intervals in transverse momentum  $p_T$  for LHC22f and the cut ITSTPC

Fit on invariant mass of  $\pi^0$  with asymmetric Gaussian

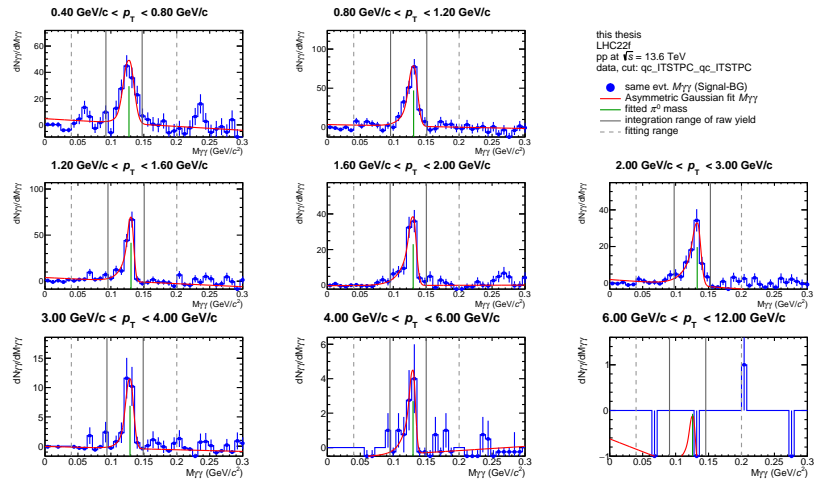


Figure A.13: Overview on the  $\pi^0$  invariant mass fits for the intervals in transverse momentum  $p_T$  for LHC22f and the cut ITSTPC

Same and (scaled) mixed event

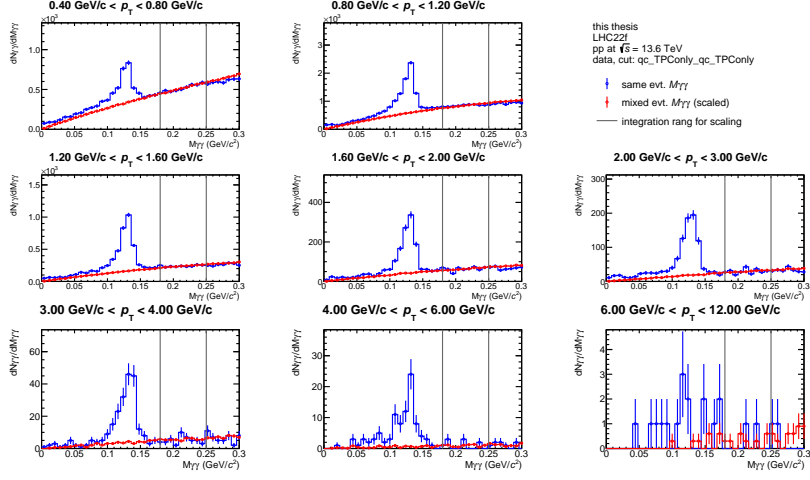


Figure A.14: Overview on the  $\pi^0$  invariant mass fits for the intervals in transverse momentum  $p_T$  for LHC22f and the cut TPCOnly

Fit on invariant mass of  $\pi^0$  with asymmetric Gaussian

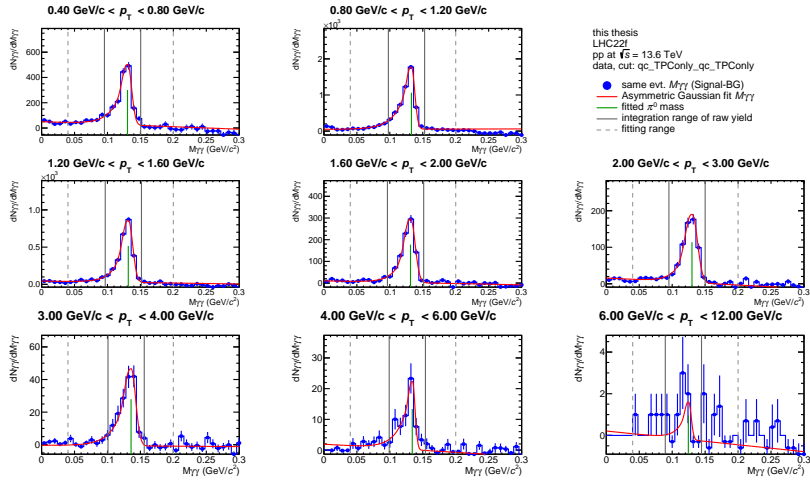


Figure A.15: Overview on the  $\pi^0$  invariant mass fits for the intervals in transverse momentum  $p_T$  for LHC22f and the cut TPCOnly

Fit parameters of asymmetric Gaussian on invariant mass of  $\pi^0$  for different cuts

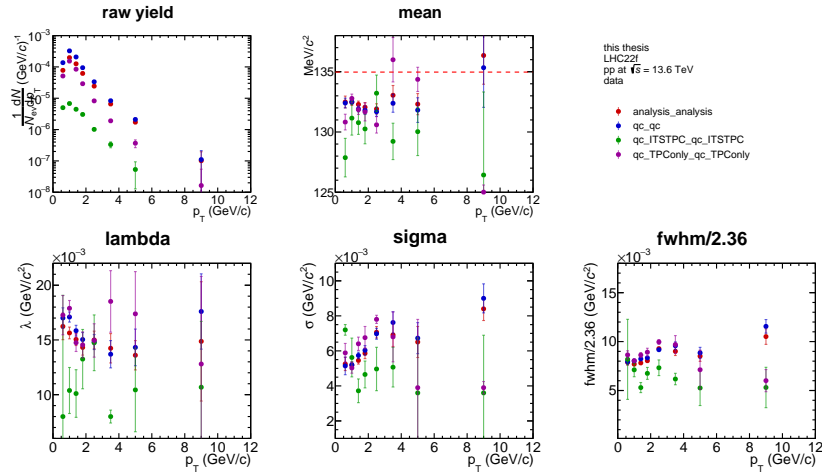


Figure A.16: Overview on the determined fit parameters of the  $\pi^0$  invariant mass fit as a function of the transverse momentum  $p_T$  for LHC22f for the different cuts qc (red), analysis (blue), ITSTPC (green) and TPCOnly (violet)

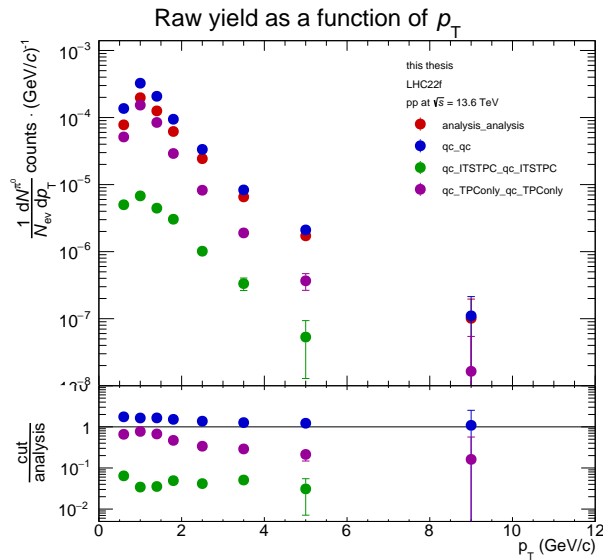


Figure A.17: Calculated raw yield as a function of the transverse momentum  $p_T$  for LHC22f for the different cuts qc (red), analysis (blue), ITSTPC (green) and TPCOnly (violet)

## A.2.3 Results for LHC23d1k (MC)

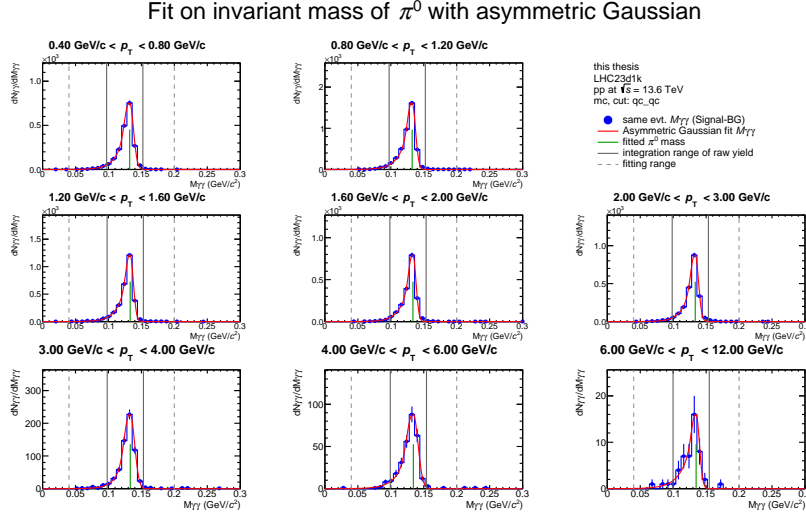


Figure A.18: Overview on the  $\pi^0$  invariant mass fits for the intervals in transverse momentum  $p_T$  for LHC23d1k and the cut quality control (qc)

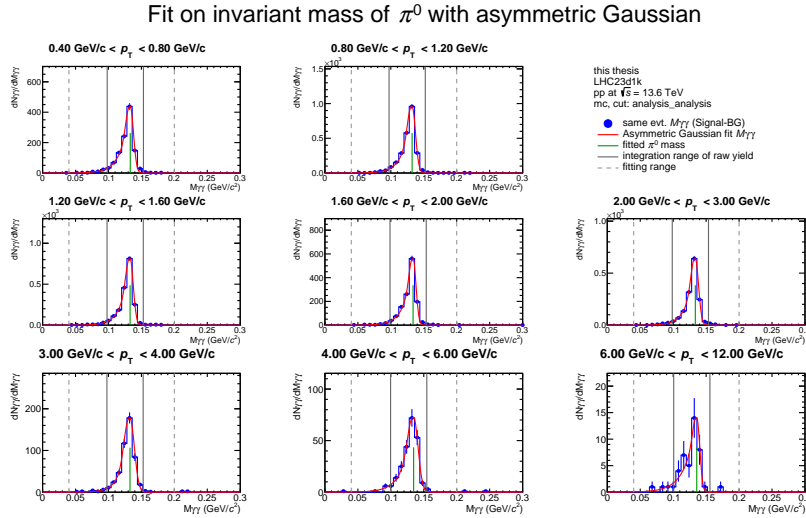


Figure A.19: Overview on the  $\pi^0$  invariant mass fits for the intervals in transverse momentum  $p_T$  for LHC23d1k and the cut analysis

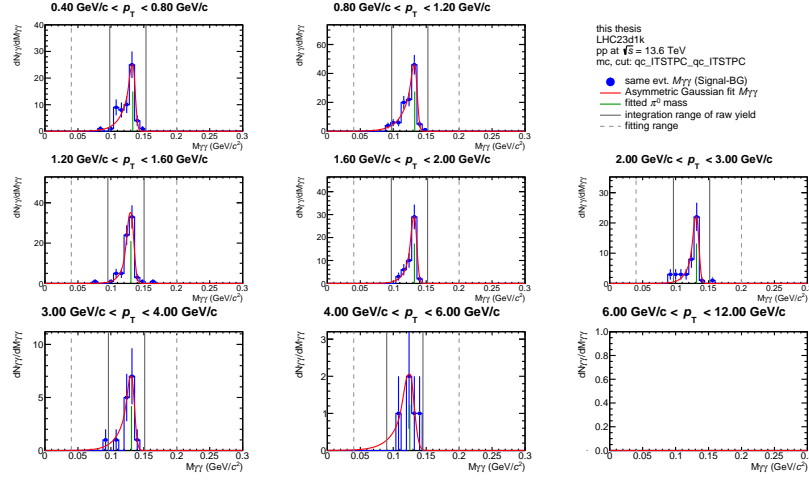
Fit on invariant mass of  $\pi^0$  with asymmetric Gaussian

Figure A.20: Overview on the  $\pi^0$  invariant mass fits for the intervals in transverse momentum  $p_T$  for LHC23d1k and the cut ITSTPC

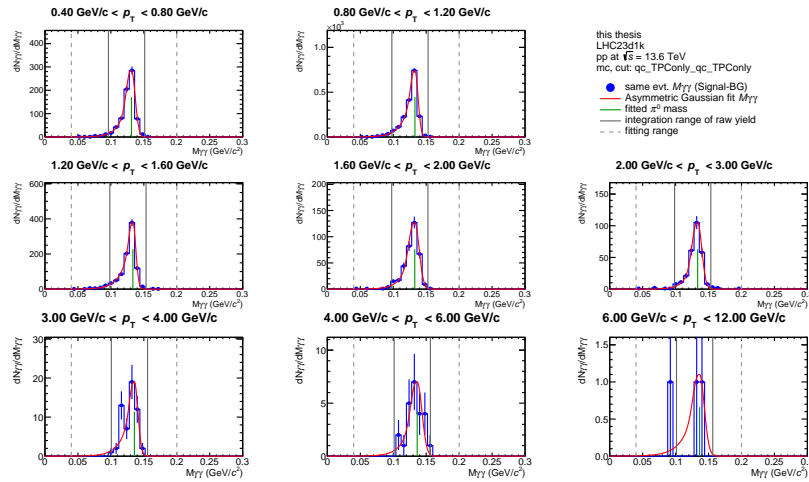
Fit on invariant mass of  $\pi^0$  with asymmetric Gaussian

Figure A.21: Overview on the  $\pi^0$  invariant mass fits for the intervals in transverse momentum  $p_T$  for LHC23d1k and the cut TPCOnly

Fit parameters of asymmetric Gaussian on invariant mass of  $\pi^0$  for different cuts

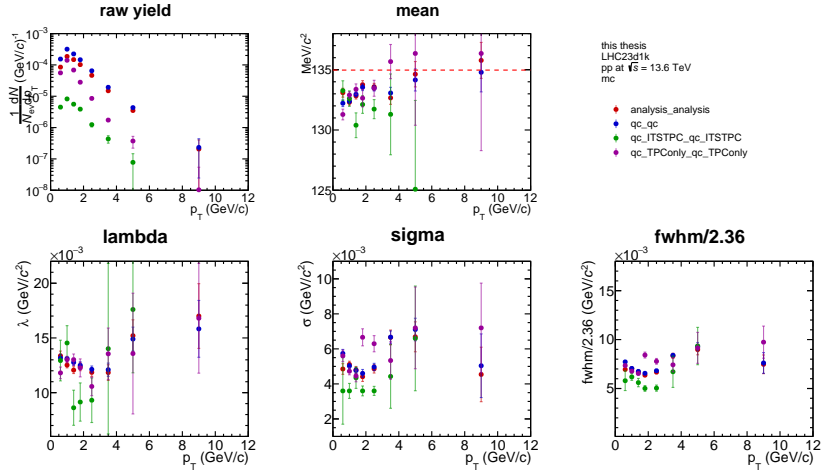


Figure A.22: Overview on the determined fit parameters of the  $\pi^0$  invariant mass fit as a function of the transverse momentum  $p_T$  for LHC23d1k for the different cuts qc (red), analysis (blue), ITSTPC (green) and TPCOnly (violet)

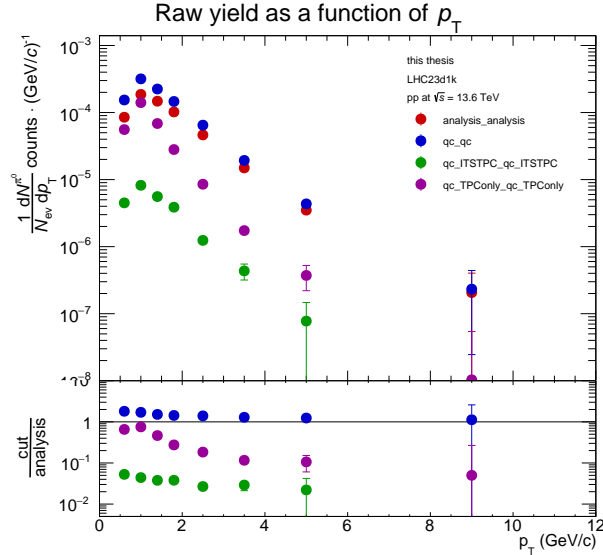


Figure A.23: Calculated raw yield as a function of the transverse momentum  $p_T$  for LHC23d1k for the different cuts qc (red), analysis (blue), ITSTPC (green) and TPCOnly (violet)

## A.2.4 Results for LHC23zc

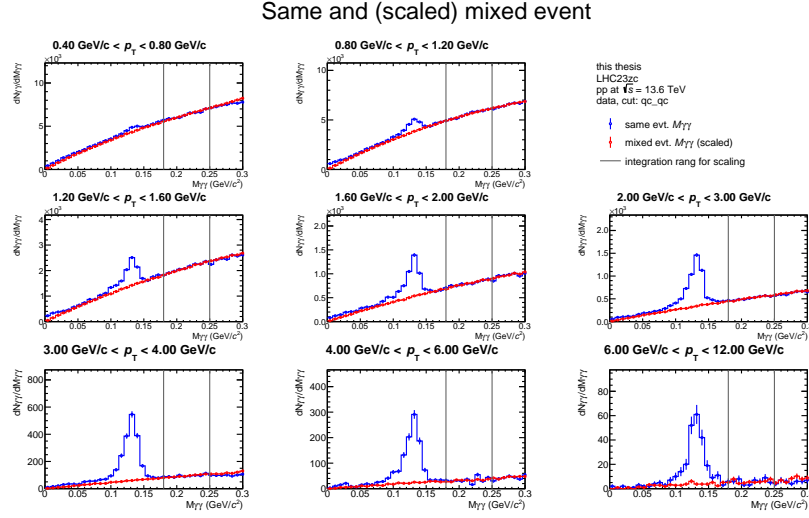


Figure A.24: Overview on the  $\pi^0$  invariant mass fits for the intervals in transverse momentum  $p_T$  for LHC23zc and the cut quality control (qc)

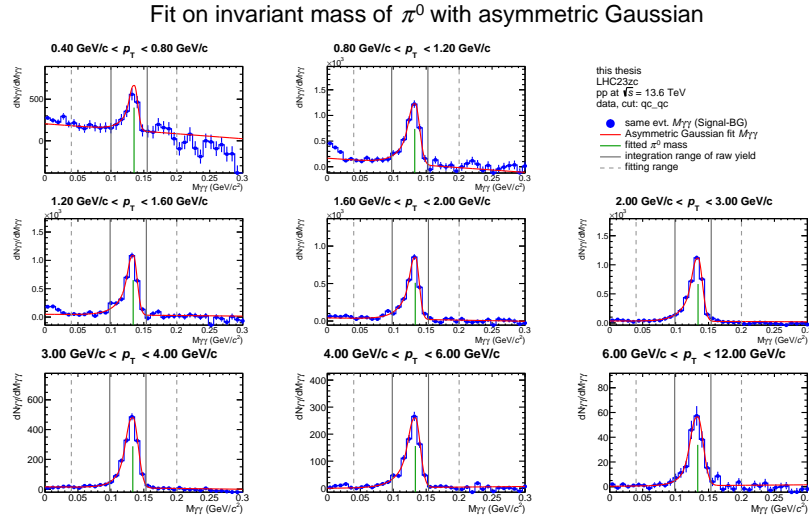


Figure A.25: Overview on the  $\pi^0$  invariant mass fits for the intervals in transverse momentum  $p_T$  for LHC23zc and the cut quality control (qc)

## Same and (scaled) mixed event

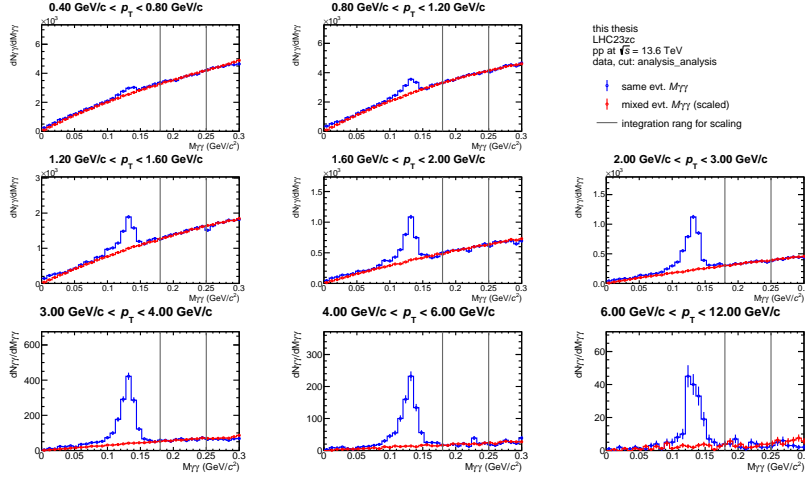


Figure A.26: Overview on the  $\pi^0$  invariant mass fits for the intervals in transverse momentum  $p_T$  for LHC22f and the cut analysis

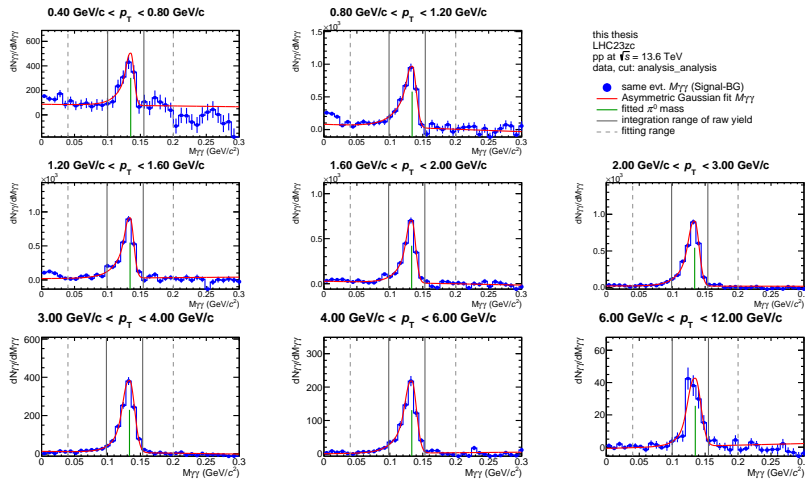
Fit on invariant mass of  $\pi^0$  with asymmetric Gaussian

Figure A.27: Overview on the  $\pi^0$  invariant mass fits for the intervals in transverse momentum  $p_T$  for LHC22f and the cut analysis

## Same and (scaled) mixed event

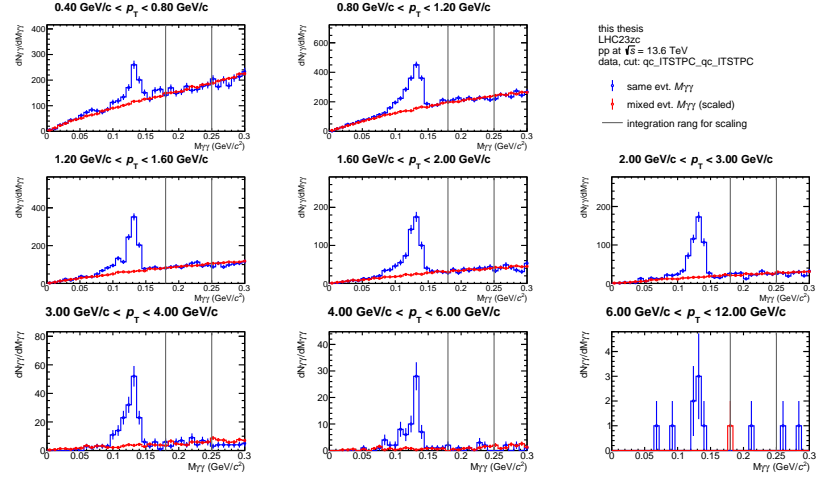


Figure A.28: Overview on the  $\pi^0$  invariant mass fits for the intervals in transverse momentum  $p_T$  for LHC22f and the cut ITSTPC

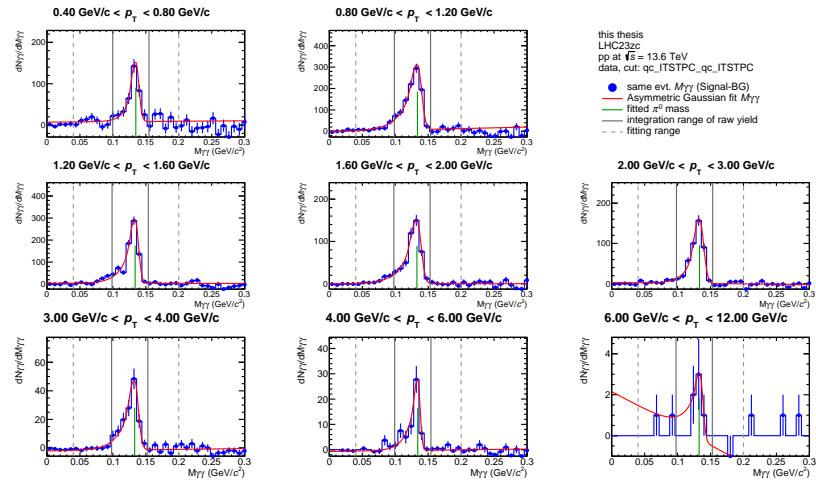
Fit on invariant mass of  $\pi^0$  with asymmetric Gaussian

Figure A.29: Overview on the  $\pi^0$  invariant mass fits for the intervals in transverse momentum  $p_T$  for LHC22f and the cut ITSTPC

Same and (scaled) mixed event

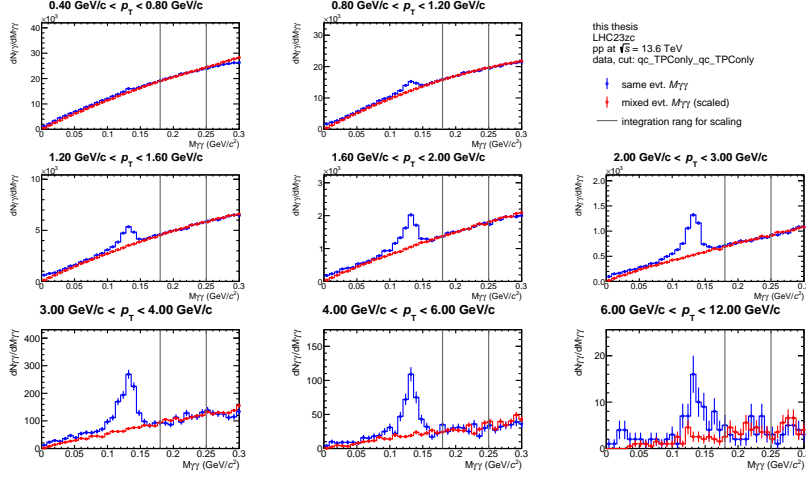


Figure A.30: Overview on the  $\pi^0$  invariant mass fits for the intervals in transverse momentum  $p_T$  for LHC22f and the cut TPConly

Fit on invariant mass of  $\pi^0$  with asymmetric Gaussian

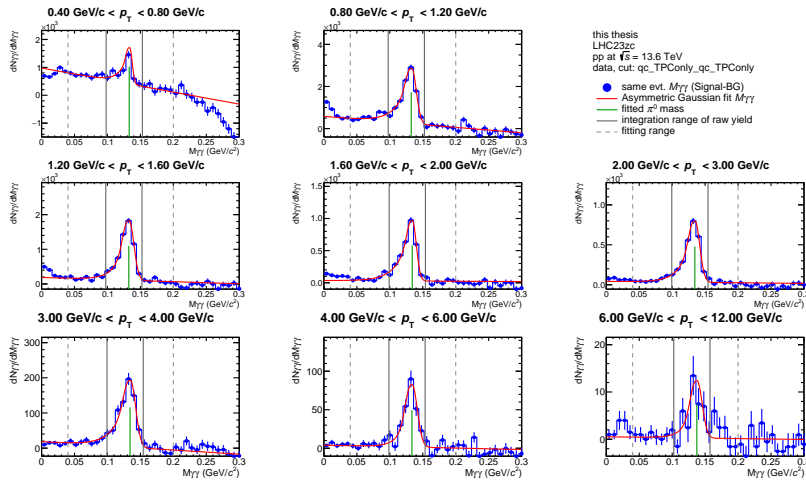
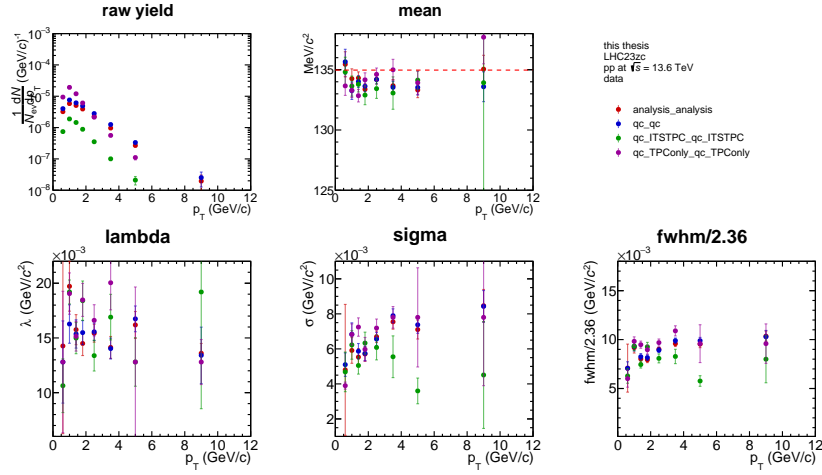
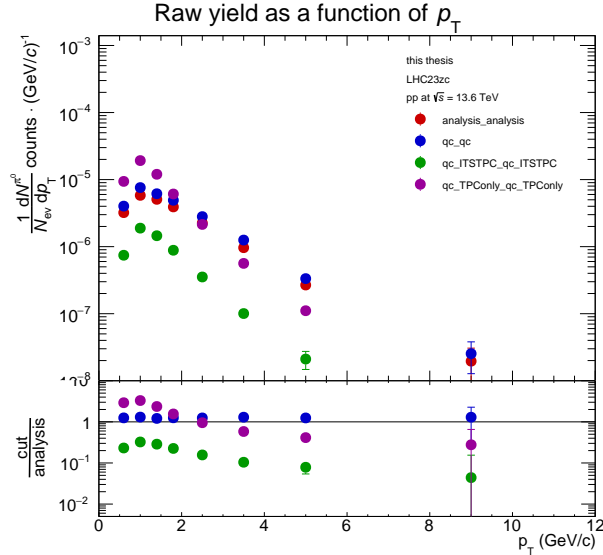


Figure A.31: Overview on the  $\pi^0$  invariant mass fits for the intervals in transverse momentum  $p_T$  for LHC22f and the cut TPConly

Fit parameters of asymmetric Gaussian on invariant mass of  $\pi^0$  for different cutsFigure A.32: Overview on the determined fit parameters of the  $\pi^0$  invariant mass fit as a function of the transverse momentum  $p_T$  for LHC23zc for the different cuts qc (red), analysis (blue), ITSTPC (green) and TPCOnly (violet)Figure A.33: Calculated raw yield as a function of the transverse momentum  $p_T$  for LHC23zc for the different cuts qc (red), analysis (blue), ITSTPC (green) and TPCOnly (violet)

### A.2.5 Results for LHC22o (min. Bias)

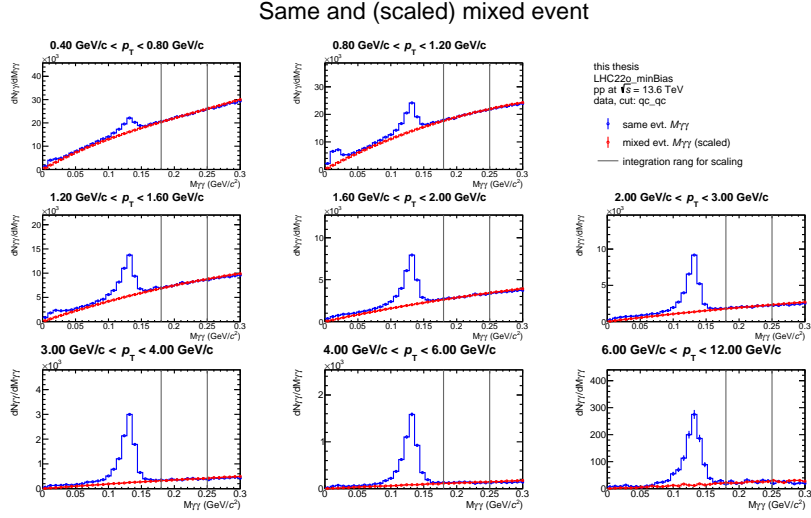


Figure A.34: Overview on the  $\pi^0$  invariant mass fits for the intervals in transverse momentum  $p_T$  for LHC22o min Bias and the cut quality control (qc)

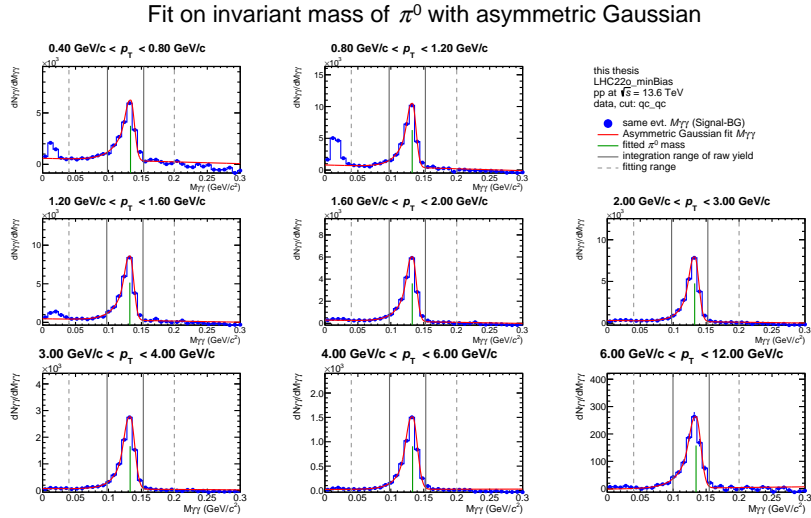


Figure A.35: Overview on the  $\pi^0$  invariant mass fits for the intervals in transverse momentum  $p_T$  for LHC22o min Bias and the cut quality control (qc)

Same and (scaled) mixed event

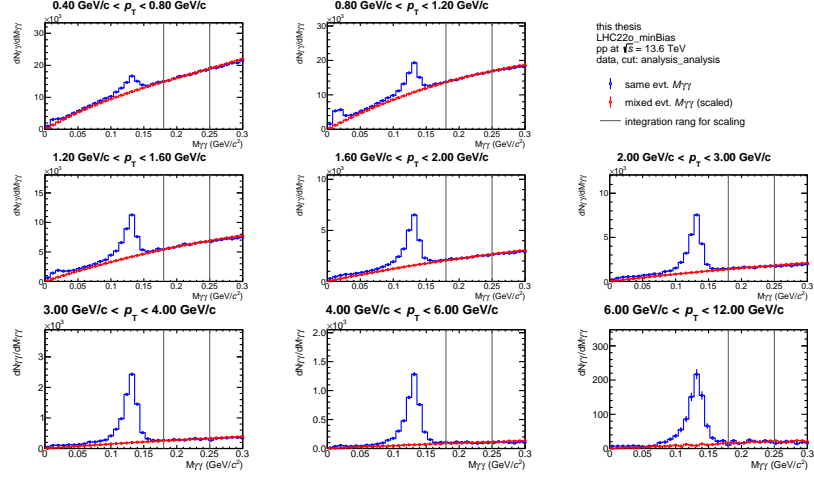


Figure A.36: Overview on the  $\pi^0$  invariant mass fits for the intervals in transverse momentum  $p_T$  for LHC22f and the cut analysis

Fit on invariant mass of  $\pi^0$  with asymmetric Gaussian

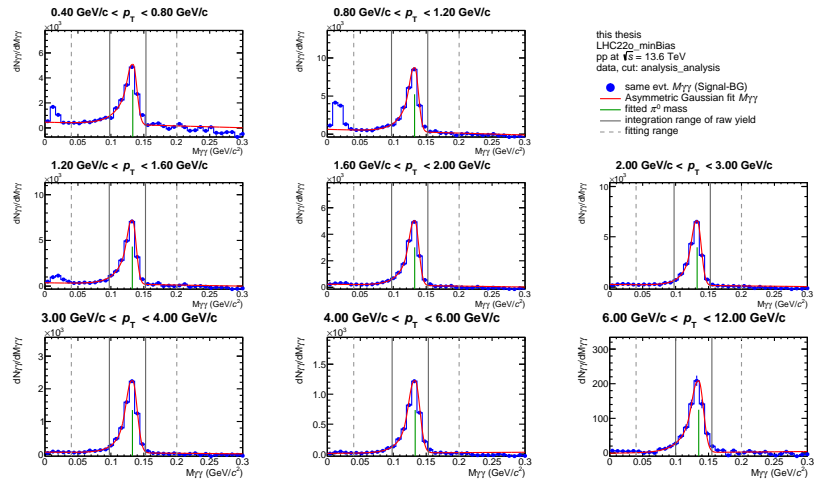


Figure A.37: Overview on the  $\pi^0$  invariant mass fits for the intervals in transverse momentum  $p_T$  for LHC22f and the cut analysis

Same and (scaled) mixed event

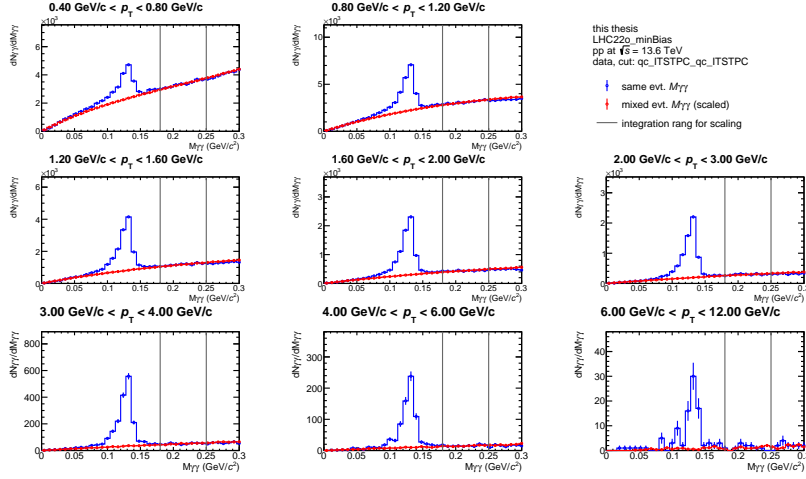


Figure A.38: Overview on the  $\pi^0$  invariant mass fits for the intervals in transverse momentum  $p_T$  for LHC22f and the cut ITSTPC

Fit on invariant mass of  $\pi^0$  with asymmetric Gaussian

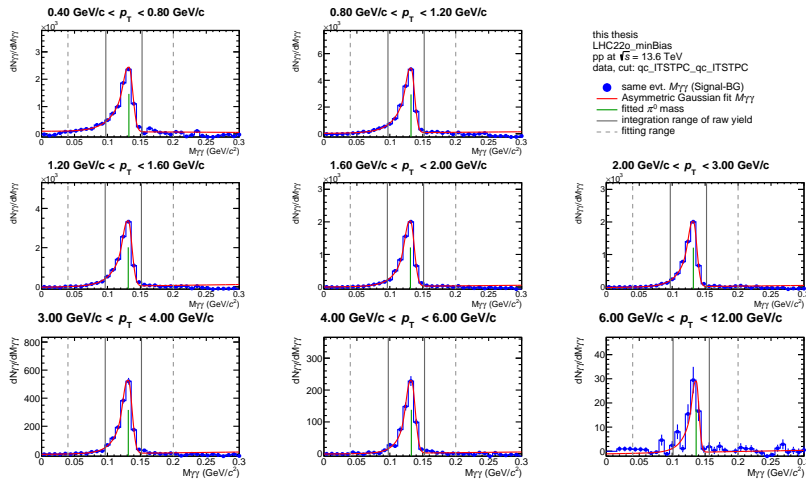


Figure A.39: Overview on the  $\pi^0$  invariant mass fits for the intervals in transverse momentum  $p_T$  for LHC22f and the cut ITSTPC

Same and (scaled) mixed event

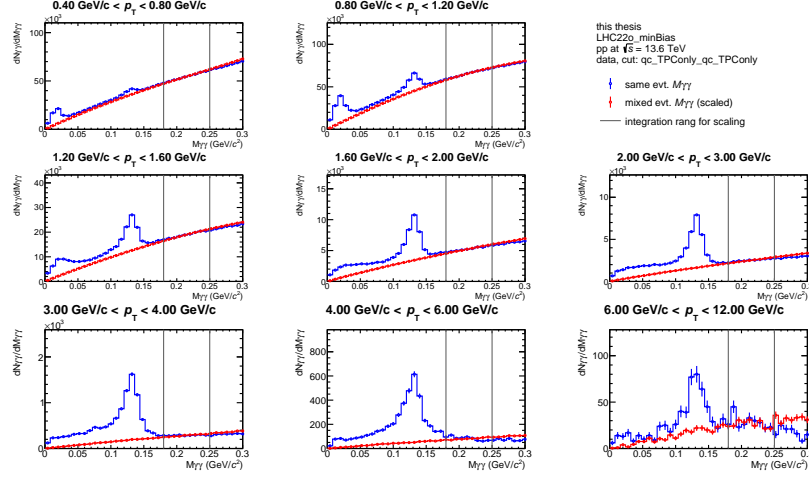


Figure A.40: Overview on the  $\pi^0$  invariant mass fits for the intervals in transverse momentum  $p_T$  for LHC22f and the cut TPCOnly

Fit on invariant mass of  $\pi^0$  with asymmetric Gaussian

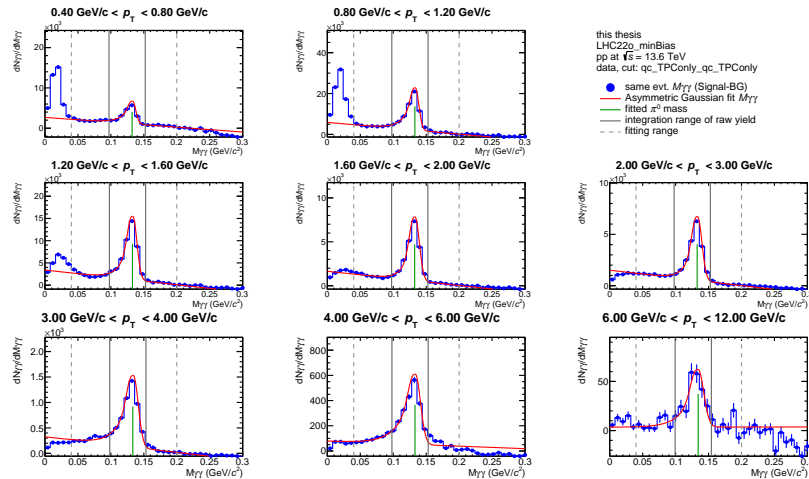


Figure A.41: Overview on the  $\pi^0$  invariant mass fits for the intervals in transverse momentum  $p_T$  for LHC22f and the cut TPCOnly

Fit parameters of asymmetric Gaussian on invariant mass of  $\pi^0$  for different cuts

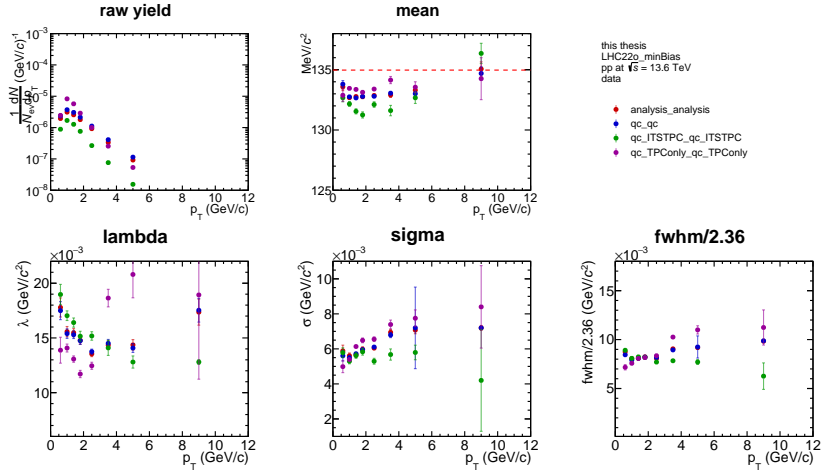


Figure A.42: Overview on the determined fit parameters of the  $\pi^0$  invariant mass fit as a function of the transverse momentum  $p_T$  for LHC22o min Bias for the different cuts qc (red), analysis (blue), ITSTPC (green) and TPCOnly (violet)

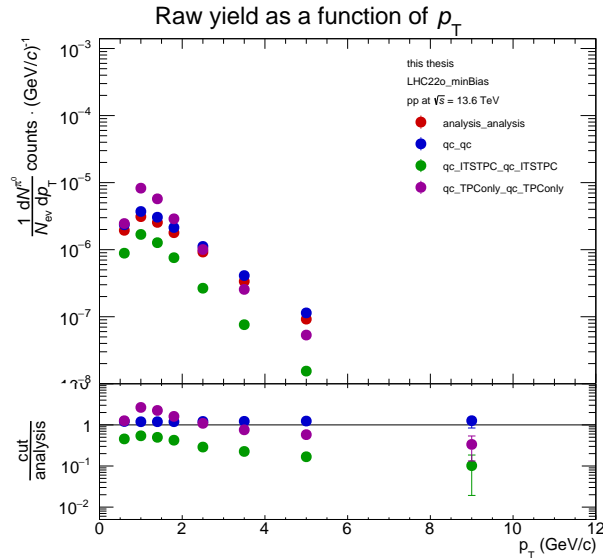


Figure A.43: Calculated raw yield as a function of the transverse momentum  $p_T$  for LHC22o min Bias for the different cuts qc (red), analysis (blue), ITSTPC (green) and TPCOnly (violet)

# B List of Acronyms

**ACORDE** ALICE Cosmic Rays Detector.

**ALICE** A Large Ion Collider Experiment.

**ATLAS** A Toroidal LHC Apparatus.

**CERN** European Organisation for Nuclear Research (CERN).

**CMS** Compact Muon Solenoid.

**DCal** Di-jet Calorimeter.

**EMCal** Electromagnetic Calorimeter.

**FWHM** Full Width at Half Maximum.

**Geant** Platform for Monte Carlo simulations.

**GEM** Gas Electron Multiplier.

**IB** Inner Barrel.

**ITS** Inner Tracking System.

**LEP** Large Electron-Positron Collider.

**LHC** Large Hadron Collider.

**LHCb** Large Hadron Collider beauty experiment.

**LS2** Long Shutdown 2.

**MFT** Muon Forward Tracker.

**MRPC** Multi-gap Resistive-Plate Chamber.

**MWPC** Multiwire Proportional chambers.

**OB** Outer Barrel.

**PCM** Photon Conversion Method.

**PHOS** Photon Spectrometer.

**PWGEM** Physics Working Group Electromagnetic Probes.

**QCD** Quantum Chromodynamics.

**QGP** quark-gluon-plasma.

**SM** Standard Model.

**TOF** Time-of-Flight detector.

**TPC** Time Projection Chamber.

**TR** Transition Radiation.

**TRD** Transition Radiation Detector.

# C Bibliography

- [1] ALICE Collaboration and others. Data-driven precision determination of the material budget in ALICE. *JINST*, 18(11):P11032, 2023. doi:10.1088/1748-0221/18/11/P11032.
- [2] Carsten Burgard and David Galbraith. A standard diagram of the current standard model of physics, December 2016. URL: <https://texample.net/tikz/examples/model-physics/>.
- [3] Mark Thomson. *Modern particle physics*. Cambridge University Press, Cambridge, 2013.
- [4] Particle Data Group Collaboration. Review of Particle Physics: 2022. *PTEP*, 2022:083C01, 2022. doi:10.1093/ptep/ptac097.
- [5] P. Braun-Munzinger and J. Wambach. The Phase Diagram of Strongly-Interacting Matter. *Rev. Mod. Phys.*, 81:1031–1050, 2009. doi:10.1103/RevModPhys.81.1031.
- [6] Peter Braun-Munzinger and Johanna Stachel. The quest for the quark–gluon plasma. *Nature*, 448(7151):302–309, July 2007. doi:10.1038/nature06080.
- [7] ALICE Collaboration. The ALICE experiment – A journey through QCD, November 2022. URL: <http://arxiv.org/abs/2211.04384>.
- [8] Wit Busza, Krishna Rajagopal, and Wilke Van Der Schee. Heavy Ion Collisions: The Big Picture and the Big Questions. *Annual Review of Nuclear and Particle Science*, 68(1):339–376, October 2018. doi:10.1146/annurev-nucl-101917-020852.
- [9] Patrick Steinbrecher. The QCD crossover at zero and non-zero baryon densities from Lattice QCD. *Nuclear Physics A*, 982:847–850, February 2019. doi:10.1016/j.nuclphysa.2018.08.025.
- [10] Piotr Traczyk. The LHC lead-ion collision run starts, September 2023. URL: <https://home.cern/news/news/experiments/lhc-lead-ion-collision-run-starts>.
- [11] Ewa Lopienska. The CERN accelerator complex, layout in 2022, 2022. URL: <https://cds.cern.ch/record/2800984>.
- [12] CERN webpage. Accelerator upgrades during LS2, September 2023. URL: <https://home.cern/press/2022/accelerator-upgrades-during-ls2>.

- [13] Rende Steerenberg. Accelerator Report: Getting lead ions ready for physics, September 2023. URL: <https://home.cern/news/news/accelerators/accelerator-report-getting-lead-ions-ready-physics>.
- [14] CERN webpage. The history of CERN | timeline.web.cern.ch. URL: <https://timeline.web.cern.ch/timeline-header/89#>.
- [15] ALICE Collaboration. Letter of Intent for A Large Ion Collider Experiment [ALICE], 1993. URL: <https://cds.cern.ch/record/290825>.
- [16] ALICE Collaboration. ALICE upgrades during the LHC Long Shutdown 2, February 2023. arXiv:2302.01238 [hep-ex, physics:nucl-ex, physics:physics]. doi: 10.48550/arXiv.2302.01238.
- [17] CERN webpage. A magnet worthy of ALICE, 2002. Issue: 46/2002 Pages: 1. URL: <https://cds.cern.ch/record/46083>.
- [18] ALICE Collaboration. Technical Design Report for the Upgrade of the ALICE Inner Tracking System. *J. Phys. G*, 41:087002, 2014. doi:10.1088/0954-3899/41/8/087002.
- [19] F. Reidt. Upgrade of the ALICE ITS detector. *Nuclear Instruments and Methods in Physics Research Section A: Accelerators, Spectrometers, Detectors and Associated Equipment*, 1032:166632, June 2022. URL: <https://www.sciencedirect.com/science/article/pii/S0168900222002042>, doi:10.1016/j.nima.2022.166632.
- [20] ALICE collaboration. ALICE Inner Tracking System (ITS): Technical Design Report, 1999. Place: Geneva Series: Technical design report. ALICE. URL: <https://cds.cern.ch/record/391175>.
- [21] Mario Sitta. Private communication.
- [22] ALICE Collaboration. The upgrade of the ALICE TPC with GEMs and continuous readout. *JINST*, 16(03):P03022, 2021. doi:10.1088/1748-0221/16/03/P03022.
- [23] ALICE Collaboration. The ALICE experiment at the CERN LHC. *JINST*, 3:S08002, 2008. doi:10.1088/1748-0221/3/08/S08002.
- [24] A. Andronic. ALICE TRD - Introduction. URL: <http://www-alice.gsi.de/trd/intro.html>.
- [25] ALICE Collaboration. The ALICE Transition Radiation Detector: Construction, operation, and performance. *Nuclear Instruments and Methods in Physics Research Section A: Accelerators, Spectrometers, Detectors and Associated Equipment*, 881:88–127, February 2018. doi:10.1016/j.nima.2017.09.028.

- [26] Xian-Guo Lu. Energy loss signals in the ALICETRD. *Nuclear Instruments and Methods in Physics Research Section A: Accelerators, Spectrometers, Detectors and Associated Equipment*, 706:16–19, April 2013. doi:10.1016/j.nima.2012.05.015.
- [27] CERN webpage. ALICE TOF. URL: <https://alice-collaboration.web.cern.ch/node/34978>.
- [28] Hermann Kolanoski, Norbert Wermes, Hermann Kolanoski, and Norbert Wermes. *Particle Detectors: Fundamentals and Applications*. Oxford University Press, Oxford, New York, June 2020.
- [29] Roger Forty. Time of flight technologies, 2021. URL: <https://indico.cern.ch/event/999817/contributions/4253048/attachments/2240084/3797788/TOF%20technologies.pdf>.
- [30] ALICE Collaboration. ALICE Time-Of-Flight system (TOF) : Technical Design Report. URL: <https://cds.cern.ch/record/430132?ln=de>.
- [31] Fabio Sauli. Interaction of photons and neutrons with matter. In *Gaseous Radiation Detectors: Fundamentals and Applications*, Cambridge Monographs on Particle Physics, Nuclear Physics and Cosmology, pages 43–75. Cambridge University Press, Cambridge, 2014. doi:10.1017/CB09781107337701.005.
- [32] Silvia Masciocchi. Detectors for particle tracking and identification, 2017.
- [33] ALICE Collaboration. ALICE: Physics Performance Report. *J. Phys. G*, 32:1295–2040, 2006. doi:10.1088/0954-3899/32/10/001.
- [34] J. Podolanski and R. Armenteros. III. Analysis of V-events. *The London, Edinburgh, and Dublin Philosophical Magazine and Journal of Science*, 45(360):13–30, January 1954. doi:10.1080/14786440108520416.
- [35] Nikita Philip Tatsch. Software development and validation for photon measurements in Run 3 using the photon conversion method in ALICE. Bachelor’s thesis, Heidelberg University, 2022. URL: [https://www.physi.uni-heidelberg.de/Publications/Bachelor\\_Thesis\\_Nikita\\_Philip\\_Tatsch.pdf](https://www.physi.uni-heidelberg.de/Publications/Bachelor_Thesis_Nikita_Philip_Tatsch.pdf).
- [36] J. Alme and others. The ALICE TPC, a large 3-dimensional tracking device with fast readout for ultra-high multiplicity events. *Nuclear Instruments and Methods in Physics Research Section A: Accelerators, Spectrometers, Detectors and Associated Equipment*, 622(1):316–367, October 2010. doi:10.1016/j.nima.2010.04.042.
- [37] Stephan Friedrich Stiefelmeier. Improving the accuracy of the photon conversion method in alice. Master’s thesis, Heidelberg University,

2017. URL: [https://www.physi.uni-heidelberg.de/Publications/thesis\\_as\\_uploaded\\_to\\_physi.pdf](https://www.physi.uni-heidelberg.de/Publications/thesis_as_uploaded_to_physi.pdf).
- [38] ALICE Collaboration. Production of charged pions, kaons and (anti-)protons in Pb-Pb and inelastic pp collisions at  $\sqrt{s_{\text{NN}}} = 5.02$  TeV. *Physical Review C*, 101(4):044907, April 2020. doi:10.1103/PhysRevC.101.044907.
- [39] Felix Schlepper. Svertexer with tpc-only tracks, 2023. URL: <https://indico.cern.ch/event/1351889/contributions/5696031/attachments/2762206/4810535/291123.pdf>.

# Acknowledgements

First and foremost, I would like to express my heartfelt appreciation to Silvia Masciocchi for giving me the opportunity to join her kind-hearted research team. Being a part of the ALICE group has been a tremendous pleasure, and the chance to contribute to such a big collaboration has been both fulfilling and inspiring.

Of course, special thanks go to Ana Marín for her exceptional guidance throughout the entire process. I am especially grateful for her committed support in addressing the various challenges and questions that occurred throughout my work.

Furthermore, I express my gratitude to Klaus Reygers for kindly agreeing to be my second examiner.

Finally, my heartfelt thanks goes to those who supported me throughout my entire degree, providing unwavering emotional support and fostering my self-belief. Your encouragement has been invaluable.

# Declaration of Authorship

Ich versichere, dass ich diese Arbeit selbstständig verfasst und keine anderen als die angegebenen Quellen und Hilfsmittel benutzt habe.

**Heidelberg, den 16. Februar 2024**

---

Alica Marie Enderich